



TAMPEREEN TEKNILLINEN YLIOPISTO
TAMPERE UNIVERSITY OF TECHNOLOGY

Ilari Jönkkäri

Rheological Characterization of Magnetorheological Fluids



Julkaisu 1566 • Publication 1566

Tampere 2018

Tampereen teknillinen yliopisto. Julkaisu 1566
Tampere University of Technology. Publication 1566

Ilari Jönkkäri

Rheological Characterization of Magnetorheological Fluids

Thesis for the degree of Doctor of Science in Technology to be presented with due permission for public examination and criticism in Festia Building, Auditorium Pieni Sali 1, at Tampere University of Technology, on the 5th of October 2018, at 12 noon.

Tampereen teknillinen yliopisto - Tampere University of Technology
Tampere 2018

Doctoral candidate: Ilari Jönkkäri
Laboratory of Materials Science
Faculty of Engineering Sciences
Tampere University of Technology
Finland

Supervisor: Jyrki Vuorinen, Professor
Laboratory of Materials Science
Faculty of Engineering Sciences
Tampere University of Technology
Finland

Instructor: Seppo Syrjälä, University Lecturer
Laboratory of Chemistry and Bioengineering
Faculty of Natural Sciences
Tampere University of Technology
Finland

Essi Sarlin, Assistant Professor
Laboratory of Materials Science
Faculty of Engineering Sciences
Tampere University of Technology
Finland

Pre-examiners: Juan de Vicente, Professor
Department of Applied Physics
University of Granada
Spain

Ladislau Vékás, Doctor
Center for Fundamental and Advanced Technical
Research
Romanian Academy-Timisoara Branch
Romania

Opponents: Ladislau Vékás, Doctor
Center for Fundamental and Advanced Technical
Research
Romanian Academy-Timisoara Branch
Romania

Sami Hietala, University Lecturer
Department of Chemistry
Faculty of Science
University of Helsinki
Finland

ISBN 978-952-15-4184-1 (printed)
ISBN 978-952-15-4221-3 (PDF)
ISSN 1459-2045

ABSTRACT

Magnetorheological (MR) fluids are smart materials that respond to an external magnetic field by changing their rheological properties. These field dependent properties are typically studied by rotational rheometry. Since the data of the rotational rheometer measurements may include errors caused by various sources, it is essential to study the rheological characterization of the MR fluids before the results are used in research. A major drawback of MR fluids is sedimentation that may weaken fluids MR response over time. The sedimentation is settling of magnetic particles induced by the large density mismatch between the particles and the carrier fluid. In this study, the rheological characterization of MR fluids by a rotational rheometer is first examined to reveal how the measurements should be done in order to gain reliable knowledge about their properties. Secondly a bidisperse size distribution of magnetic particles, consisting of micron- and nano-sized particles, was studied as a way to improve the sedimentation stability.

The study of rheological characterization of MR fluids by rotational rheometer involved determination field dependent yield stresses by using various measuring procedures and plate-plate measuring geometries with different surfaces. The results demonstrated that the measured static and dynamic yield stresses are strongly affected by the plate surface characteristics as the magnetic and roughened plates provided considerably higher values than the smooth non-magnetic plates. A likely source for the difference is wall slip that may happen during rotational rheometer measurements. Furthermore, it was shown that the wall slip of MR fluid does not cause measuring gap height dependency of the results, which is surprising, as its existence is commonly used as an indicator of the wall slip.

The bidisperse MR fluids were prepared by dispersing micron- and nano-sized particles in Silicone Oil (SO) or Ionic liquid (IL). The impact of the carrier fluid type and nanoparticle fraction, composition and size on the off-state viscosity, sedimentation stability and MR response were studied. The maghemite ($\gamma - \text{Fe}_2\text{O}_3$) nanoparticles used in the study were synthesized by Liquid Flame Spray (LFS) method that offers an interesting alternative for the chemical co-precipitation commonly used to prepare magnetic nanoparticles as it is a very versatile process. The dispersion of the micron-sized particles was better IL than in SO indicated by lower off-state viscosity and higher MR response. A partial substitution of micron-sized particles by nanoparticles provided improved sedimentation stability with both carrier fluids. The impact became stronger as the nanoparticle fraction was increased or the nanoparticle size was decreased. Both lead to higher particle surface to volume ratio and greater number of particles. These can improve the sedimentation stability by inducing higher drag between the particles and the carrier fluid or by forming a thicker nanoparticle halo around the micron-sized particles. The nanoparticles had only a minor impact on the fluids MR response, but often increased the field independent viscosity, which can be considered as a disadvantage in some applications.

PREFACE

The work was carried out in the Laboratory of Materials Science at Tampere University of Technology during the years 2008-2018. The work was partly conducted in the frame of Fundamentals of Magnetorheological Fluid Based Technology research financed by the Academy of Finland.

I wish to express my gratitude to my supervisor Professor Jyrki Vuorinen and instructor Dr. Seppo Syrälä for the guidance and support during this long path. I am grateful to my instructor Assistant Professor Essi Sarlin for the detailed comments on this thesis and to all my co-authors for their contribution. I want to thank Professor Pentti Järvelä for interesting conversations and for giving me the opportunity to work in the former Laboratory of Plastics and Elastomer Technology. I also wish to thank all the present and former staff members of the Laboratory of Materials Science for the team spirit that has made me feel privileged to work here. My special thanks go to M.Sc. Jari Kokkonen, Dr. Juuso Terva, Dr. Matti Isakov, M.Sc. Turo Salomaa and Dr. Niko Ojala for supporting me in this work and for your friendship over the years.

Finally, I am grateful to my family Mari, Iida, Aaro and Alekski for bringing love and joy in my life, as well as to my parents Nina and Tapio, and my sisters Eveliina and Karoliina for your unquestioning support.

Tampere, August 2018

Ilari Jönkkäri

LIST OF PUBLICATIONS

This thesis is based on the following original publications I to IV. Additionally, some unpublished data are presented and discussed.

- I Jönkkäri I, Syrjälä S: Evaluation of techniques for measuring the yield stress of a magnetorheological fluid, *Applied Rheology* 20 (2010) 45875-45882.
- II Jönkkäri I, Kostamo E, Kostamo J, Syrjälä S, Pietola M: Effect of the plate surface characteristics and gap height on yield stress of a magnetorheological fluid, *Journal of Smart Materials and Structures* 21(7) (2012) 075030.
- III Jönkkäri I, Isakov M, Syrjälä S, Sedimentation stability and rheological properties of ionic liquid-based bidisperse magnetorheological fluids, *Journal of Intelligent Materials Systems and Structures* 26(16) (2015) 2256-2265.
- IV Jönkkäri I, Sorvali M, Huhtinen H, Sarlin E, Salminen T, Haapanen J, Mäkelä J.M, Vuorinen J, Characterization of bidisperse magnetorheological fluids utilizing maghemite ($\gamma - \text{Fe}_2\text{O}_3$) nanoparticles synthesized by flame spray pyrolysis, *Journal of Smart Materials and Structures* 26(9) (2017) 095004.

AUTHOR'S CONTRIBUTION

- I The author is responsible for the experimental work. He analysed the results and wrote the manuscript together with Seppo Syrjälä.
- II The author is responsible for the experimental work and interpretation of the results. Esa Kostamo is responsible for the modelling of the magnetic flux density in the measuring gap. The author wrote the manuscript together with Esa Kostamo. All authors commented on and approved the manuscript.
- III The author is responsible for planning and performing the experiments, interpretation of the results and writing the manuscript. Matti Isakov is responsible for building the MATLAB® script that was used to analyse the sedimentation images. All authors commented on and approved the manuscript.
- IV The author is responsible for planning the research and performing the rheological experiments. Miika Sorvali is responsible for synthetization of the maghemite nanoparticles. Hannu Huhtinen is responsible for measuring the magnetic properties of the particles. Essi Sarlin is responsible the TEM images and Turkka Salminen for the Raman spectroscopy. The author wrote the manuscript with Miika Sorvali, Hannu Huhtinen and Essi Sarlin. All authors commented on and approved the manuscript.

LIST OF SYMBOLS AND ABBREVIATIONS

Greek symbols

β	Contrast factor
γ_0	Strain amplitude
$\dot{\gamma}$	Shear rate
$\dot{\gamma}_R$	Rim shear rate
δ	Phase angle
η_p	Plastic viscosity
η_f	Viscosity of the carrier fluid
η_r	Relative viscosity
η_s	Viscosity of the suspension
λ	Coupling constant
μ_0	Vacuum permeability
μ_{rp}	Relative permeability of the particles
μ_{rf}	Relative permeability of the carrier fluid
ρ_f	Density of the carrier fluid
ρ_p	Density of the particles
τ	Shear stress
τ_0	Shear stress amplitude
τ_R	Rim shear stress
τ_{aR}	Apparent rim shear stress
τ_y	Yield stress
τ_{yd}	Dynamic yield stress
τ_{ys}	Static yield stress
$\tau_{y,meas}$	Measured yield stress
ϕ	Particle volume fraction
ϕ_0	Angular amplitude
ϕ_{eff}	Effective particle volume fraction
ϕ_l	Volume fraction of large particles
ϕ_m	Maximum packing density
ϕ_s	Volume fraction of small particles
χ	Magnetic susceptibility
Ω	Angular velocity
ω	Angular frequency

Latin symbols

A	Consistency factor for the power law model
B	Magnetic flux density
\bar{B}	Rheology-relevant average magnetic flux density
\bar{B}_{ref}	\bar{B} with non-magnetic plates and the smallest gap height
\bar{B}_h	\bar{B} with magnetic plates and/or higher gap height
C	Setup dependent coefficient
c_l	Coefficient for large particles (model by Qi and Tanner)
c_s	Coefficient for small particles (model by Qi and Tanner)
d	Particle diameter
F_g	Gravitational force
G	Complex modulus
G'	Storage modulus
G''	Loss modulus
g	Gravitational acceleration
H	Magnetic field strength
h	Gap height
h_c	Height of the inner cylinder
h_0	Initial height of suspension in the test tube
h_{10000}	Height of suspension in the test tube after 10 000h
K	Consistency factor for the Herschel-Bulkley model
K_E	Einstein coefficient
k	Empirically determined exponent for the Richardson and Zaki equation
k_B	Boltzman constant
L	Thickness of the nanoparticle halo
M	Torque
M_0	Torque amplitude
M_n	Mason number
M_s	Saturation magnetization
n	Power law index
n'	Local power law index
R	Plate radius
Ra	Surface roughness
R_i	Radius of the inner cylinder
R_o	Radius of the outer cylinder
r_i	Radial position in the measuring gap
T	Temperature
T_0	Absolute temperature
v_s	Sedimentation rate
v_t	Terminal velocity

Abbreviations

$\alpha - \text{Fe}$	Ferrite
$\gamma - \text{Fe}_2\text{O}_3$	Maghemite
Fe_3O_4	Magnetite
$(\text{Fe}(\text{C}_5\text{H}_5)_2)$	Ferrocene
<i>FSP</i>	Flame spray pyrolysis
<i>IL</i>	Ionic liquid
<i>LFS</i>	Liquid flame spray
<i>MR</i>	Magnetorheological
<i>PD</i>	Packing density
<i>SEM</i>	Scanning electron microscope
<i>SO</i>	Silicone oil
<i>TEM</i>	Transmission electron microscope
<i>XRD</i>	X-ray diffraction

Contents

ABSTRACT	i
PREFACE	iii
LIST OF PUBLICATIONS	v
AUTHOR'S CONTRIBUTION	vii
LIST OF SYMBOLS AND ABBREVIATIONS	ix
1 Introduction	1
2 Magnetorheological (MR) fluids	3
2.1 Magnetorheology	3
2.2 MR fluid composition	4
2.2.1 Particles	4
2.2.2 Nanoparticles	4
2.2.3 Carrier fluids	5
2.2.4 Additives	6
2.3 On-state properties	6
2.3.1 Yielding	6
2.3.2 Flow	9
2.4 Off-state properties	10
2.4.1 Field independent viscosity	10
2.4.2 Sedimentation	11
3 Rheometry	13
3.1 Rotational rheometry	13
3.1.1 On-state measurements	13
3.1.2 Yield stress	15
3.1.3 Off-state measurements	16
3.1.4 Wall slip	16
4 Experimental	19
4.1 Materials	19
4.1.1 Carrier fluids	19
4.1.2 Particles	20
4.1.3 Additives	20
4.2 Sample preparation	20
4.3 Characterization techniques	21
4.3.1 Rotational rheometer	21
4.3.2 SQUID magnetometer	22
4.3.3 Sedimentation measuring system	22
4.3.4 Electron microscopy	22

4.3.5	X-ray diffraction	23
4.3.6	Raman spectroscopy	23
5	Results and discussion	25
5.1	Effect of the measuring method on the measured yield stress	25
5.2	Effect of the plate properties and measuring gap height on the measured yield stress	28
5.2.1	Modelling and measurement of the magnetic flux density profile with different measuring setups	29
5.2.2	Effect of the plate surface characteristics on the measured yield stresses	33
5.2.3	Effect of the gap height on the measured yield stresses	34
5.3	Properties of the bidisperse magnetorheological fluids	35
5.3.1	Properties of the particles	35
5.3.2	Field independent viscosity of the bidisperse MR fluids	38
5.3.3	Sedimentation of the bidisperse MR fluids	39
5.3.4	MR response of the bidisperse MR fluids	42
5.3.4.1	Dynamic yield stress	42
5.3.4.2	Oscillatory measurements	44
6	Conclusions	47
6.1	Suggestions for the future work	48
	Bibliography	49
	Appendix: Original publications	56

1 Introduction

Smart materials are materials that change their properties in a controlled manner as response to an external stimulus [1]. Magnetorheological (MR) fluids are smart materials, which rheological properties can be altered rapidly and reversibly by application of an external magnetic field [2,3]. Since the magnitude of the response depends on the intensity of the field, the properties of MR fluids can be adjusted almost in real time.

The MR technology enables design of devices where mechanical or electrical components are replaced by a magnetically responsive material. The MR fluids were discovered by Jacob Rabinow in 1940s and were first used in a magnetorheological clutch [4]. Since then the number of engineering applications of the technology have increased and include shock absorbers, dampers, engine mounts, brakes, magneto-resistors, magnetic field sensors and polishing technology among others [5–8].

The MR fluids are suspensions of magnetic particles dispersed in a non-magnetic carrier fluid like mineral or silicone oil. The particles are typically spherical, micron-sized and made of ferromagnetic soft magnetic materials, most commonly iron. The particles become magnetized under an external magnetic field and form columnar structures aligned with the field. The structures hinder fluid's flow causing an increase in viscosity and appearance of a yield stress, which is the minimum stress needed to break the particle structures and initiate flow. The strength of the particle structure depend on the attractive magnetostatic forces between the magnetized particles, which are affected by the composition of the fluid and intensity of the magnetic field.

Since the particles in MR fluids are metallic, hard and dense, the fluids may have to contain additives that inhibit corrosion and wear and slow down sedimentation. Traditionally the MR fluid's stability against sedimentation has been improved by thixotropic agents and surfactants. As a drawback both can increase the field independent viscosity [9, 10] and in addition the thixotropic agents can make the redispersion of the particles more difficult [11] and weaken the MR response [12]. In more recent studies the usage of magnetic particles with bidisperse size distribution, consisting of both micron- and nano-sized particles, has offered a way to hinder sedimentation and even improve the MR response at the same time [13–18].

The field dependent yield stress is often used as a measure for the strength of the MR response. The yielding of the MR fluid happens in several stages determined by the elastic limit, static and dynamic yield stresses [19]. They are generally determined from data measured with a rotational rheometer applying a plate-plate measuring geometry. The measured data may include errors caused for example by inhomogeneous magnetic flux density profile in the measuring gap [20] and wall slip [21, 22]. Especially the wall slip may cause drastic underestimation of the yield stress. Therefore, it is essential to eliminate or quantify the potential error sources before the data is used for the development of the MR technology.

The first objective of this work was to study how the field dependent yield stresses of MR fluids should be measured with a rotational rheometer in order to suppress the errors caused

by the measuring procedure and system. Furthermore, the outcomes of the study were utilized in pursue to reach the second aim that was to study how the composition of bidisperse fluid is affecting its properties like sedimentation stability and dynamic yield stress. The following research questions were stated:

1. How does the measuring set-up of the rotational rheometer applying plate-plate geometry influence on the measured yield stresses?
2. Can ionic liquid (IL) as a carrier fluid provide improved properties for bidisperse MR fluids?
3. Does the size of the magnetic nanoparticles affect the properties of bidisperse MR fluid?

The first research question was studied in publications I and II. The influence of the measuring procedure on the measured yield stresses and the deviation of the results were investigated in the publication I. The effect of the plate surface properties on the smoothness of the magnetic flux density profile and on the wall slip were studied in publication II. Measuring geometries with different plate surfaces characteristics were build for this purpose as the system was originally provided only with a single smooth measuring geometry. The second research question was studied in publication III. Bidisperse MR fluids dispersed in SO and IL were prepared the dispersion and sedimentation stabilities as well as MR response were investigated. The publication IV focused on the third research question. The LFS method was utilized in the research to prepare ($\gamma - \text{Fe}_2\text{O}_3$) nanoparticles with different average sizes.

The scientific contributions of the thesis are the following:

- Magnetic plates of the plate-plate measuring geometry were found to provide more uniform magnetic flux density profile in the measuring gap than non-magnetic plates, which can reduce transient changes during long measurements caused by particle migration. The measured yield stresses were found to be higher when the MR fluid was measured with magnetic plates or roughened non-magnetic plates. This was likely a consequence of reduced wall slip.
- The measured yield stress was independent of the gap height even though the wall slip was present. The results indicate that the study of the gap height dependency alone does not provide enough information about the existence of the wall slip with MR fluids.
- IL together with magnetic nanoparticles was found to provide improved dispersion stability of the MR fluid. This was likely achieved by a combination of steric repulsion generated by the IL and halving of the magnetic nanoparticles.
- LFS method was used to synthesize $\gamma - \text{Fe}_2\text{O}_3$ nanoparticles with properties comparable to the particles prepared by chemical co-precipitation. The LFS method is an interesting alternative for the chemical co-precipitation as it is very versatile and can be used to create various one- or multicomponent metal and metal oxide particles.
- Decrease of the nanoparticle size was found to improve the sedimentation stability of bidisperse MR fluid. It was likely a consequence of higher surface area per volume ratio and greater number of the nanoparticles. However, it also led to higher field independent viscosity.

2 Magnetorheological (MR) fluids

2.1 Magnetorheology

Magnetorheology is a branch of science that studies flow and deformation behaviour of materials that show magnetic field induced changes. These materials include MR fluids, gels, foams and elastomers, from which the MR fluids are clearly the most studied ones and have many applications. The field induced changes, also called as the MR effect, may appear as an increase in modulus or viscosity, change in the damping ratio or appearance of a yield stress. The MR effect is fast and reversible: the material returns to its original state within milliseconds as the magnetic field is switched off. The MR materials are commonly composed of magnetic particles dispersed in a non-magnetizable fluid or solid medium. The MR materials with a solid medium are meant to operate in the pre-yield region whereas MR fluids generally operate in the post-yield region.

In the absence of an external magnetic field the MR fluids behave in more or less Newtonian manner. The magnetic field induces polarization of the magnetic particles in the fluid, which then interact and form columnar structures in direction of the magnetic field lines. The chain structures resist flow and thereby increase the fluid's viscosity. The magnetostatic forces between the particles have a direct effect on the energy needed to start and maintain the flow, therefore the viscosity and yield stress are proportional to the external magnetic field strength. The flow behaviour of MR fluids is generally well described with a Bingham equation

$$\tau = \tau_y(H) + \eta_p \dot{\gamma}, \tau \geq \tau_y \quad (2.1)$$

where τ is the shear stress, $\tau_y(H)$ magnetic field depended yield stress, η_p the plastic viscosity and $\dot{\gamma}$ the shear rate. In the pre-yield region the MR fluid behaves in a solid viscoelastic manner and its behaviour can be described in the following way:

$$\tau = G(H)\gamma, \tau < \tau_y \quad (2.2)$$

Here, G is the complex modulus that depends on the magnetic field strength [2].

MR elastomers are solid counterparts of MR fluids. The usage of a solid medium helps to overcome the sedimentation problem of MR fluids. The mixing of the particles into the elastomer is done prior to the crosslinking, where the elastomer gets its solid form. The crosslinking is normally done under magnetic field, as the magnetizable particles are still able to move and form chain structures in direction of the field lines. After the crosslinking is complete the elastomer has solidified and the magnetizable particles are locked in place. This type of MR elastomer is called anisotropic since its properties are directionally dependent. In the absence of a magnetic field the properties of the MR elastomer depend mainly on the properties of the elastomer matrix. When the magnetic field is switched on it induces magnetostatic attraction between the particles that adds to the energy needed to deform the material. This may be seen as an increase in the storage modulus and change in the damping properties.

2.2 MR fluid composition

The typical MR fluids contain 25-45 vol-% of magnetic particles, carrier fluids and additives. MR fluid's viscosity in absence of the magnetic field (off-state) depends mainly on fraction of the solid particles, viscosity of the carrier fluid and the possible additives, while under external magnetic field (on-state) the viscosity depends mainly on solid particle fraction, magnetic field strength and saturation magnetization of the particles.

2.2.1 Particles

The particles in MR fluids are generally of ferromagnetic material and have diameters around 1-5 μm . The most used material is the iron, which has the highest saturation magnetization of pure elements (2.1 T). The high saturation magnetization is important since there is a direct relation between it and the maximum yield stress of the MR fluid. Some iron alloys have higher saturation magnetization than pure iron and could offer a better performance for the MR fluid, but many of the alloying elements, like cobalt, have high price and would make the fluid too expensive for many applications.

The synthetization process of the iron particles is typically thermal decomposition of iron pentacarbonyl, which leads to formation of spherical Carbonyl Iron (CI) particles with fine size and high iron content [3]. The micron-sized magnetic particles have multiple magnetic domains. In an unmagnetized state the spins within a domain are aligned and each domain has a magnetic moment. However, the orientation of the moments in the constituent domains varies and they cancel each other out, thus the particle has no net magnetization. If the particle is placed under an external magnetic field the domains having the closest alignment with the field start to grow at the expense of the others. When the magnitude of the external magnetic field reaches the saturation magnetisation there is only one domain within the particle, which has its magnetic moment parallel to the external magnetic field [23]. The growth of the magnetic domains requires movement of the domain walls. The resistance to movement of the walls tells if the material is magnetically soft or hard. With magnetically hard materials the movement is difficult and the coercivity and remanent magnetization are high. This type materials are generally used in permanent magnets. With soft magnetic materials the movement of the walls is relatively easy and the coercivity and remanent magnetization are low. The magnetic particles in MR fluids are generally soft and become easily demagnetized. A strong remanent magnetization can cause agglomeration of particles without external magnetic field and thereby make the redispersion of the particles more difficult.

2.2.2 Nanoparticles

The magnetic nanoparticles in MR fluids are ferri- or ferromagnetic. The most used material by far is magnetite (Fe_3O_4) due to its availability, well known synthetization and magnetic properties [13, 14, 16, 18]. The Fe_3O_4 particles are generally synthetized by chemical co-precipitation method where the particle size and magnetic properties can be altered for example by reaction temperature, pH and surface modifications. Maghemite ($\gamma - \text{Fe}_2\text{O}_3$) is also used and its magnetic properties are near to Fe_3O_4 . Both of these magnetic iron oxides have an inverse spinel structure, but $\gamma - \text{Fe}_2\text{O}_3$ has only Fe^{3+} iron cations whereas Fe_3O_4 has both Fe^{3+} and Fe^{2+} cations. The cations, their locations in the lattice structure and the interactions between the cations affect the net magnetic moment of the material. The Fe_3O_4 particles are typically spherical, but the shapes of $\gamma - \text{Fe}_2\text{O}_3$ particles may vary from spheres

to ellipsoids over a wide size range from 2 to 1000 nm depending on the synthesis route. In general, γ -Fe₂O₃ particles are produced by a two step process via controlled oxidation of Fe₃O₄. They can also be produced directly from liquid precursors via thermal aerosol techniques, such as spray pyrolysis or Flame Spray Pyrolysis (FSP) [24, 25]. In FSP the liquid precursor is sprayed into a flame where the precursor first evaporates, then the evaporated molecules react chemically or decompose thermally, nucleate and re-condense in the form of nanoparticles. The thermal aerosol techniques offer a continuous process to synthesize nanoparticles, but the particles are typically aggregated.

Magnetic nanoparticles generally have lower saturation magnetization compared to micron-sized particles of the same material. The phenomenon is caused by a thin magnetically disordered layer at the surface of the particles, which reduces the total saturation magnetization. The effect is insignificant with micron-sized particles, but becomes remarkable when the size decreases to nanoscale as the portion of the volume of the disordered surface layer to the total volume of the particle increases [26, 27]. Because of their small size the nanoparticles only have a single magnetic domain and poses a permanent non-zero magnetic moment. The critical particle diameter for magnetic single domains depends on the material and is generally within 10-800 nm [26]. A single domain magnetic particle just below the critical limit generally has a high coercivity, as the magnetic anisotropy makes it difficult to change the direction of magnetization from the preferred easy axis. If the size of the particle decreases further the coercivity diminishes quickly to zero because of increased thermal excitation that causes rapid fluctuation of the direction of magnetization [26, 28, 29]. The particle reaches a superparamagnetic state, where its coercivity is zero and remanent magnetization is lacking. Since magnetic nanoparticles have a permanent non-zero magnetic moment they may agglomerate unless treated with proper surfactants [30, 31].

2.2.3 Carrier fluids

The carrier fluids in the MR fluids are generally non-magnetic Newtonian liquids like water or oil. More recently the use of Ionic Liquids (IL) has also been studied. The selection of the carrier fluid affects the rheology, tribological properties, sedimentation and thermal stability of the MR fluid. A low viscosity carrier fluid like water offers a high relative change when the MR fluid is subjected to an external magnetic field. The obvious drawbacks of water are corrosion when in contact with ferrous particles and a high vapour pressure that can lead to evaporation of the carrier fluid in open systems. Mostly the carrier fluids in MR applications are hydrocarbon or silicone oils. Hydrocarbon oils have good lubricating properties, durability and a large selection of known additives. Silicone oils have a slightly wider operating temperature range, better compatibility with materials like rubbers and are available at different precise viscosities [2].

ILs are salts that are in liquid state at room temperature and offer a new and interesting choice for a carrier fluid. ILs can be designed to a specific application, since the properties are mainly determined by selection of base cation and anion and can be finely tuned even further by variation of the alkyl groups that are incorporated into the cation [32]. In addition to versatility, the ILs have other beneficial properties: they are non-volatile, have low vapour pressure and good thermal stability. Usage of ILs as carrier fluids in MR fluids and ferrofluids has been reported in several papers, where it has offered an improved sedimentation stability [33, 34] and a better redispersivity [35] compared to conventional carrier fluids. It has been suggested that the anions in the IL could form a steric barrier on the surface of

the magnetic particles preventing agglomeration [34, 35].

2.2.4 Additives

There are two major challenges with MR fluids as mentioned before; sedimentation and wear. The additives are mainly used to prevent or reduce their effect. This research is only focusing on the sedimentation. The sedimentation is conventionally hindered by surfactants and thixotropic agents. The surfactants are short molecule chains capable to adhere on the particle surface from one end while the other end is stretching out and preventing a contact with neighbouring particle [36]. Typical surfactants are fatty acids like lecithine and oleinic acid [37]. They also improve the dispersion stability of the particles, which is required especially with the magnetic nanoparticles, since they pose a permanent non-zero magnetic moment and will agglomerate if not stabilized. Thixotropic agents are typically substances that are capable to form three dimensional structures in a carrier fluid when the shear rates are small and slow down the descent of magnetic particles. When the shear rate increases the structures break down and the viscosity decreases. They can be organic or inorganic. The organic thixotropic agents are polymers, like high molecular weight hydrocarbons or polyureas. The inorganic thixotropic agents are typically nanosized solid particles like fumed silica or colloidal clay [11, 37, 38]. However, when the MR fluid is exposed to an external magnetic field the non-magnetic nanoparticles tend to disturb the formation of particle structures, thus resulting to a weaker MR effect [12]. The usage of magnetic nanoparticles together with micron-sized particles has also proven to improve the sedimentation stability while even strengthening the particle structures under magnetic field [13–18, 39, 40]. Furthermore, the additives can be used to prevent oxidation or control viscosity [3].

2.3 On-state properties

2.3.1 Yielding

The existence of a true yield stress in fluids has been questioned by number of authors, but it is generally recognized that number of fluids have a limiting stress below which appreciable flow does not occur [41, 42]. The yield stress of MR fluids appear when the fluid is subjected to an external magnetic field that induces polarization of the particles. The particles chain up and form columnar structures along the magnetic field flux lines that restrict flow as illustrated at the figure 2.1 a [2]. The yielding of the MR fluids has several stages; there are elastic limit, static and dynamic yield stresses. The elastic yield stress is the maximum shear stress that the structure can sustain while recovering completely after the stress is removed. The deformation happens by slight tilting of the chains without a rupture (figure 2.1 b). The magnetostatic interactions cause a torque in the tilted position that try to reoriented the chains in direction with the magnetic field [43]. The static yield stress is the stress needed to initiate the flow and the dynamic yield stress is the stress that is needed to continuously break the particle structure and maintain the flow while the particle structures are reforming (figure 2.1 c) [19]. The strength of the structure depends on the magnetostatic interaction forces between the particles. At low magnetic field strengths the magnetostatic forces and therefore also the yield stress are proportional to the field strength squared. At higher fields the magnetization in the polar regions of the particles begin to saturate due to a local concentration of the magnetic field in the contact area of the particles and the relationship

becomes weaker [44]. The yield stress τ_y reaches the maximum when the particles become fully saturated as follows:

$$\tau_y \approx \phi\mu_0 H^2, \text{ low fields} \quad (2.3)$$

$$\tau_y \approx \phi\mu_0 M_s^{1/2} H^{3/2}, \text{ moderate fields} \quad (2.4)$$

$$\tau_y \approx \phi\mu_0 M_s^2, \text{ high fields} \quad (2.5)$$

Here, ϕ is the particle volume fraction, μ_0 the vacuum permeability, M_s the saturation magnetization of the particles and H the external magnetic field strength.

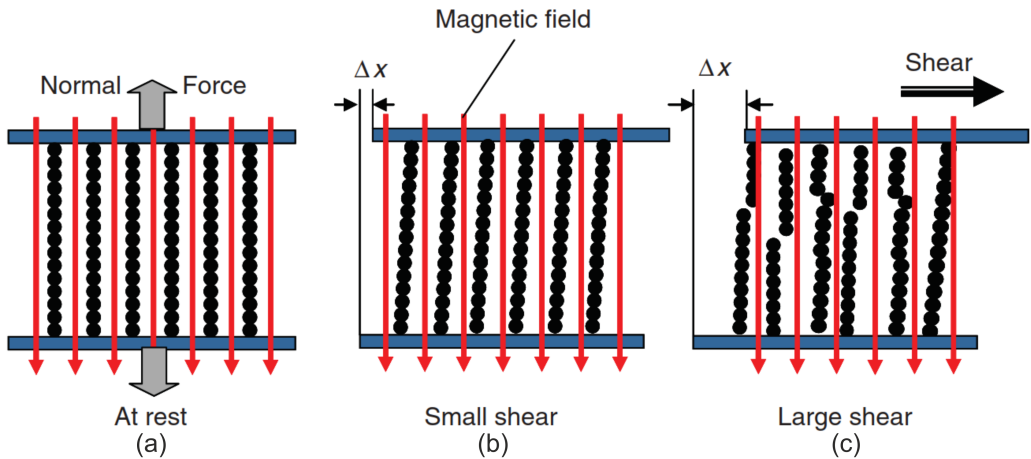


Figure 2.1: Particle chains in parallel with the magnetic field flux lines (a), tilted chains without rupture at small deformations (b) and ruptured chains at large deformations (c) [43].

Based on equations 2.3 - 2.5, one could predict linear relationship between the yield stress and the particle concentration. However, this is only valid at low particle concentrations where the effect of the interactions between the field induced particle structures is negligible. When the particle concentration is higher, a faster than linear growth of the yield stress is observed [3].

The size of the magnetic particles has an impact on the yield stress aswell, especially if the size is in nano scale. This is evident from the properties of ferrofluids, which are highly stable colloidal suspensions consisting of magnetic nanoparticles that are well dispersed in a carrier fluid and stabilized with surfactants. They have only a weak MR effect and do not generate a yield stress. The formation of the chain structures under magnetic field happens due to the interactions of magnetic dipoles. The magnitude of the magnetostatic forces between the particles diminishes if the magnetic field strength, saturation magnetization or the size of the particles decreases [45]. The saturation magnetization of the nanoparticles is smaller compared to larger particles of the same material as previously discussed in the section 2.2.2.1. The formation of the particle structures by the magnetostatic forces is opposed by the thermodynamic forces, which are generated by the thermal movements of molecules in

the surrounding carrier fluid called Brownian motions. The potential of the particles to form chain structures under magnetic field can be estimated by so called coupling constant λ , which is the ratio of the magnetic interaction energy to the thermal energy

$$\lambda = \frac{\pi(\mu_0\chi H)^2 d^3}{18k_B T} \quad (2.6)$$

where χ is the magnetic susceptibility, d the particle diameter, k_B the Boltzman constant and T the temperature. With a conventional MR fluid under typical magnetic field strengths the magnetostatic forces are much higher in comparison to the Brownian forces and λ is much higher than unity. As the particle size decreases to small enough (about 10 nm) the situation becomes reversed and only a weak MR effect appears [13, 19, 45, 46].

The bidisperse MR fluids have an extremely bimodal distribution of particle sizes. The diameter of the large particles is the same as with conventional MR fluids around 1-10 μm and the small particles are in the nanoscale with typical diameters of 5-20 nm [36]. There are two different ways how the bidisperse MR fluids are usually prepared: the micron-sized particles are dispersed into a carrier fluid together with nanoparticles and a surfactant [17, 18, 47] or the micron-sized particles are dispersed into a ferrofluid [13–16, 39, 48]. It is difficult to disperse the nanoparticles in the carrier fluid completely by the first way as they may already be aggregated. The bidisperse MR fluid will likely contain nanoparticle aggregates or agglomerates rather than separate nanoparticles. In the second case the nanoparticles are already stabilized with surfactants and well dispersed in the carrier fluid before the larger particles are added. The resulting bidisperse MR fluid can be approximated as a magnetizable carrier fluid where the micron-sized particles are dispersed in.

The bidisperse MR fluids can develop even higher yield stresses than monodisperse MR fluids with the same total particle loading. There has been several theories for the phenomenon. One explanation is that the nanoparticles are able to fill the cavities between the larger particles and strengthen the particle structures [13]. If the nanoparticles are small enough ($d < 10$ nm), well dispersed in a carrier fluid and stabilized with surfactants they form a ferrofluid that surrounds the larger particles. The high permeability of the ferrofluid enhances the attractive magnetostatic forces between the larger particles, which could increase the yield stress [16, 46]. Probably the most popular theory for the increased yield stress is that the nanoparticles can improve the dispersion stability of the MR fluid by forming a magnetically attached halo or cloud of nanoparticles around the micron-sized particles. This would increase their separation and prevent irreversible aggregation due to remnant magnetization and van der Waals forces in the absence of an external magnetic field [14, 15]. The improved dispersion of micron-sized particles would favour the formation of a well-arranged particle structure with less defects [16]. The increasing number of contacts and smaller average distance between neighbouring particles increases the average magnetostatic force density in fluid thus improves the MR effect. A halo formation can occur if the nanoparticles are large ($d > 15$ nm) or aggregated into clusters as their interactions with the larger particles are sufficiently strong. It should be noted that even though the average particle size in ferrofluids is typically below 10 nm they often also contain some larger particles and particle aggregates capable to form the halos [48, 49].

Initially the yield stress of a bidisperse MR fluid seems to increase with the relative portion of the nanoparticles, but the increase is not monotonic. After certain nanoparticle concentration the yield stress begins to diminish. Wereley et al. studied the effect of the

nanoparticle concentration on the performance of the bidisperse MR fluid and found that the highest yield stresses were reached when 7.5% of the particles were nano sized and the yield stress was still higher than in monodisperse fluid when the portion of the nanoparticles was 20% [17]. Chaudhuri et al. reached a substantial increment in yield stress when the portion of the nanoparticles was about 10%, but at about 15% the yield stress decreases to a level below that of the monodisperse fluid [18]. The nanoparticles used in these researches were potential to form nanoparticle halos as they had an average diameter of 28 nm and were likely also aggregated since they were synthesized by a microwave-based process. The optimum nanoparticle concentration to reach the highest yield stress is likely obtained when the nanoparticles are covering the larger particles to a sufficient degree [14]. The thickness of the halo grows with the nanoparticle concentration and after certain threshold the attraction between the micron-sized particles starts to decrease because of the increased distance between them and the repulsive forces generated by the nanoparticle halo [48–50].

2.3.2 Flow

When the MR fluid is forced to flow the particles will experience a hydrodynamic drag or friction by the carrier fluid. The shear response of a MR fluid under external magnetic field is described by the Mason number that is the ratio between the hydrodynamic forces and magnetostatic forces [46, 51]. In a simple shear flow it is defined as

$$M_n = \frac{8\eta_f \dot{\gamma}}{\mu_0 \mu_{rf} \beta^2 H^2} \quad (2.7)$$

where η_f is the viscosity of the carrier fluid, μ_{rf} the relative permeability of the carrier fluid and β the contrast factor that is defined as

$$\beta = \frac{\mu_{rp} - \mu_{rf}}{\mu_{rp} + 2\mu_{rf}} \quad (2.8)$$

where μ_{rp} the relative permeability of the particles. It should be noted that in addition to the hydrodynamic forces there can also be hydrodynamic interactions as the particles in the carrier fluid disturb the flow field around them, which can then exert forces on other particles within the range of the flow field [52].

2.4 Off-state properties

2.4.1 Field independent viscosity

The field independent plastic viscosity η_p of the MR fluid has a great importance, since it creates shear rate dependent forces in MR devices that are present even if the external magnetic field is not applied and generally limits the maximum particle fraction in the MR fluid [3]. At these off-state conditions the magnetic particles are randomly distributed in the carrier fluid and the forces they encounter are mostly hydrodynamic. The magnitude of the viscosity of a MR fluid depends mainly on the viscosity of the carrier fluid and particle volume fraction ϕ , but the particle morphology (size and shape) and the additives impact on it as well. The viscosity of a suspension is commonly given as the relative viscosity η_r that is defined as

$$\eta_r = \frac{\eta_s}{\eta_f} \quad (2.9)$$

where η_s is the viscosity of the suspension. For a suspension η_r is higher than unity because of the extra energy dissipated by the hydrodynamic forces and interactions as the particle moves in the carrier fluid.

The hydrodynamic interactions are also the source of shear thinning of MR fluids at off-state conditions, which means that the viscosity of the fluid decreases with increasing shear rate. A proposed mechanism for the shear thinning is a localized viscous heating of the carrier fluid as it is squeezed through the small gaps between the particles, which decreases its viscosity and lubricates the passing of the particles [53]. These lubrication hydrodynamic interactions are especially important at high packing densities where the distance between the particles is small. The effect of the ϕ on η_r has been studied by number of authors. A model by Krieger and Dougherty [54] has been used most successfully to model experimental data when $\phi > 0.25$, which is generally the case with MR fluids. The model is expressed in a following way:

$$\eta_r = \left(1 - \frac{\phi}{\phi_m}\right)^{-K_E \phi_m} \quad (2.10)$$

Here, ϕ_m is the maximum packing density and K_E the Einstein coefficient that equals to 2.5 for spheres. As the particle fraction reaches the theoretical ϕ_m the fluid is no longer able to flow as the particles jam [52]. The theoretical value for monodisperse spheres is 0.74, but for disordered systems that exist naturally, the simulated random close-packing density of 0.64 is more appropriate [55].

The concentration of the magnetic particles has an influence on the field independent viscosity as well on the maximum yield strength of the MR fluid under magnetic field (section 2.3). Both increase with increasing particle fraction and the mechanism is basically the same: as the particle fraction increases the density of the particle-particle interactions grows [53]. The maximum yield stress of the MR fluid increases quite linearly with ϕ , but the off-state viscosity grows faster than the yield stress and eventually sets the practical maximum ϕ for the fluid. The size and shape of the particles influences on the off-state viscosity aswell. A finer particle size generally leads to higher off-state viscosity as the surface area and therefore the amount of friction between the particle and carrier fluid grows and the density of the particle-particle interactions becomes higher a [56]. The non-spherical particles have more interactions compared to spherical particles with the same ϕ , since they occupy a larger

volume as they rotate in the flow and therefore have a smaller ϕ_m [53]. The shape of the micron-sized particles is generally spherical, but the spherical nanosized particles may be aggregated into non-spherical structures during synthezation. If the particle size distribution in the suspension is not uniform, as is the case with bidisperse MR fluids, η_r differs from a monodisperse suspension. In a situations where the majority of the solid particles are large with a low concentration of small particles the viscosity should be reduced compared to a completely monodisperse suspension with the same ϕ . The cause is the higher ϕ_m (0.639-0.869) [57] as the smaller particles are able to occupy the empty spaces between the larger particles [58]. The η_r of a bidisperse fluid can be estimated for example with a model by Qi and Tanner [57]

$$\eta_r = \left[\left(1 - \frac{\phi_l}{1 - c_l \phi_l} \right) \left(1 - \frac{\phi_s}{1 - c_s \phi_s} \right) \right]^{-5/2} \quad (2.11)$$

where ϕ_l and ϕ_s are volume fractions of large and small particles respectively. The parameters c_l and c_s depend on particle size ratio, random close packing densities and few other factors as described in more detail in [57]. The model ignores Brownian motion and therefore works well only for particle sizes above 1 μm . Since the particles in bidisperse MR fluid are magnetic, their interactions are more complex compared to non-magnetic particles due to possible agglomeration by remanent magnetization. The agglomerates may break and reform in the flow due to the hydrodynamic and magnetostatic forces.

2.4.2 Sedimentation

The magnetic micron-sized particles may settle in the MR fluid at off-state conditions due to the large density mismatch between the metallic particles and the carrier fluid. The gravimetric force acting on a single spherical particle is defined as

$$F_g = (\rho_p - \rho_f) \frac{3}{4} \pi r^3 g \quad (2.12)$$

where ρ_p is the density of the particles, ρ_f is the density of the carrier fluid, g the gravitational acceleration and r the radius of the particle. The gravimetric forces are opposed by the Brownian forces that result from random thermal movement of carrier fluid molecules that are colliding with particles:

$$F_B = k_B T_0 / r^3 \quad (2.13)$$

where k_B is the Boltzman constant and T_0 the absolute temperature. The particles will settle if the gravitational forces are larger than the Brownian forces. The size of the particle has a major impact on the sedimentation; it ceases altogether when the particle size decreases to small enough, as is the case with colloidal suspensions. The downward movement of a particle requires upward back-flow of the carrier fluid during settling. Therefore, the sedimentation rate (the velocity of the settling particle) is influenced also by the viscosity of the carrier fluid, ϕ and additives. The flow of the carrier fluid is hindered if the viscosity of the carrier fluid or number of the neighbouring particles (ϕ) increases.

The additives that can improve sedimentation stability were discussed earlier in section 2.2.3. Thixotropic agents generate three dimensional networks in the carrier fluid that suspend the particles when the shear rates are small. Other stabilizing methods rely on increasing the average distance between the particles, which improves dispersion stability by reducing

the Van der Waals and magnetostatic attraction between them and prevents formation of agglomerates. The magnetostatic forces are relatively long range forces, but decrease significantly when the separation is more than the particle size [59]. The improvement of dispersion stability will also prevent formation of a hard sediment at the bottom of a container if the particles eventually settle and ease the redispersion. The different ways to improve the dispersion stability are illustrated in figure 2.2.

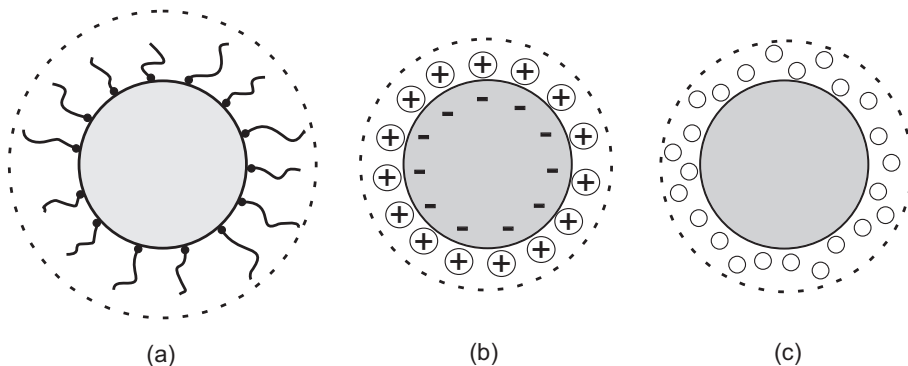


Figure 2.2: Stabilization mechanisms (a) steric repulsion (b) electrostatic repulsion and (c) nanoparticle halo.

The usage of surfactants generates steric repulsion between the particles by the molecular chains crafted on the surfaces. The steric repulsion is formed due to osmotic pressure, as there is high local concentration of molecular chains, and entropic effect, since there is less freedom for the chains to move. Another way to improve dispersion stability is by electrostatic repulsion. Electrostatic repulsion occurs, when the negative surface charge of the particles in a carrier fluid is countered by a thin layer of positive ions from the carrier fluid. This double layer repulses other particles with similar double layer. The effect becomes significant when the particle size decreases to nano scale. However, it has been stated that electrostatic repulsion alone is not enough to overcome attraction by remanent magnetization and is therefore not suitable method to stabilize magnetic particles [60]. The proposed mechanism for improved stability of bidisperse MR fluids has been the formation of magnetically attached halo or cloud of nanoparticles around the micron-sized particles that increase their separation [14,15]. This mechanism was well reported in a research by Magnet et al. where they studied formation of Fe_3O_4 nanoparticle halos around micron-sized nickel particles [49].

3 Rheometry

3.1 Rotational rheometry

A rotational rheometer is a device that is used to study flow and deformation behaviour of materials. The material is generally measured under shear load that is formed by placing the specimen between the two surfaces of the measuring geometry, one surface remains stationary and the other rotates dragging the specimen along. The device is generally supplied with plate-plate, cone-plate or concentric cylinder geometries. The schematics of the plate-plate and concentric cylinder geometries, which are generally used to measure MR fluids, are illustrated in figure 3.1. The selection of the appropriate geometry is done based on the nature of the measured material and type of the measurement.

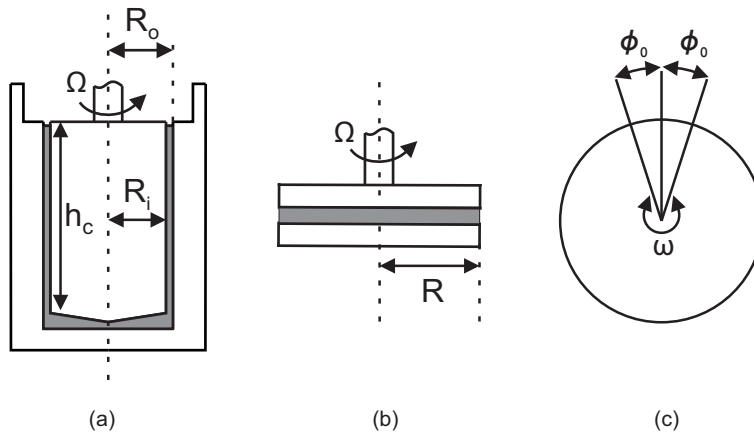


Figure 3.1: Concentric cylinder geometry (a), plate-plate geometry (b), oscillatory testing (c).

A rotational rheometer can typically function in a strain rate or stress controlled mode. In the strain rate controlled mode the angular velocity of the geometry Ω is set while the torque M needed to rotate the geometry is recorded and in the stress controlled mode it is vice versa. During a measurement the geometry can rotate steadily in one direction or oscillate back and forth as illustrated in figure 3.1.

3.1.1 On-state measurements

The measurements of MR fluids under magnetic field are typically done using a plate-plate geometry even though the flow field is not uniform; the shear rate and stress vary depending on the radial position in the gap as they are zero at the middle of the plates and reach the maximum at the rim. The reason why the geometry is used is that the magnetic field has to be also considered; the formation of a rather uniform magnetic field with a magnetic field generator is easiest with a plate-plate geometry. Usually the rheological properties with

a plate-plate geometry are determined at the rim of the plates. The rim shear rate $\dot{\gamma}_R$ is defined as

$$\dot{\gamma}_R = \frac{R\Omega}{h} \quad (3.1)$$

where R is the plate radius and h the gap height. The equation for the rim shear stress τ_R is strictly valid only for Newtonian fluids. For the non-Newtonian fluids, like MR fluids, the formula gives a so-called apparent rim shear stress τ_{aR}

$$\tau_{aR} = \frac{2M}{\pi R^3} \quad (3.2)$$

However, the true rim shear stress τ_R can be obtained from τ_{aR} by applying a correction [61]:

$$\tau_R = \tau_{aR} \left(\frac{3 + n'}{4} \right) \quad (3.3)$$

where n' is determined as

$$n' = \frac{d(\log M)}{d(\log \dot{\gamma}_R)} \quad (3.4)$$

The oscillatory measurements are customary used to study the viscoelastic properties of materials. During a measurement the specimen is subjected to shear strain that is oscillating in a sinusoidal manner at angular frequency ω . The Small Amplitude Oscillatory Shear (SAOS) measurements are done in the linear viscoelastic region, where the strains are small enough not to cause structural changes in the material. Here the resulting stress will also be sinusoidal and has the same frequency as the strain. Depending on the ratio of the viscous and the elastic responses there may be a phase angle δ between the applied strain amplitude γ_0 and the recorded stress amplitude τ_0 as illustrated in the figure 3.2.

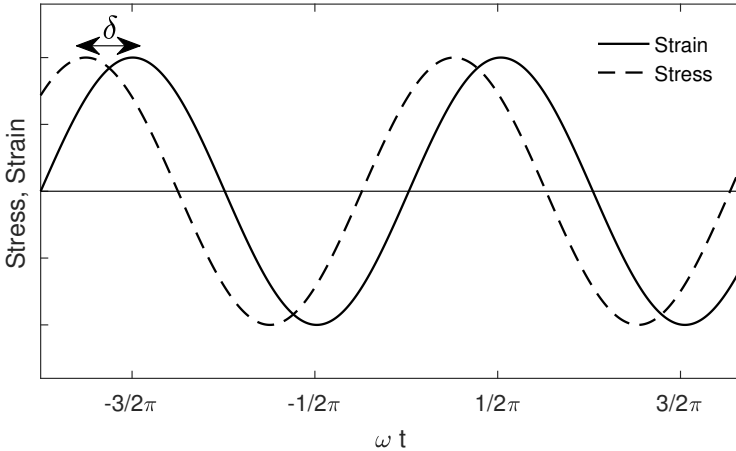


Figure 3.2: The wave forms of shear stress and strain. δ represents the phase angle.

The elastic component of the stress response is in phase with γ_0 and is characterised by the storage modulus G'

$$G'(\omega) = \frac{\tau_0}{\gamma_0} \cos \delta \quad (3.5)$$

Analogously the viscous component of the stress response is out of phase ($\delta = \pi/2$) with γ_0 and is characterised by the loss modulus G''

$$G''(\omega) = \frac{\tau_0}{\gamma_0} \sin\delta \quad (3.6)$$

Since the SAOS measurements are done in a linear viscoelastic region, the radial dependency of the shear stress and strain with plate-plate geometry is no longer an issue and no corrections are needed to calculate γ_0 and τ_0

$$\dot{\gamma}_0 = \frac{\phi_0 R}{h} \quad (3.7)$$

$$\tau_0 = \frac{2M_0}{\pi R^3} \quad (3.8)$$

Here, ϕ_0 is the the angular amplitude and M_0 the torque amplitude.

3.1.2 Yield stress

A number of techniques have been devised for measuring the yield stress of fluids directly or indirectly; reviews of these techniques have been presented by various authors (e.g. [62–64]). Since the flow field with the plate-plate geometry is not uniform, the pertinent corrections need to be applied on the data before the yield stress is evaluated. For fluids exhibiting a yield stress, the uncorrected data may lead to overestimation of the shear stress by 25% [65]. The measured yield stresses may still vary significantly depending on the used measuring techniques and/or instruments [66, 67].

The yield stress of MR fluids is generally evaluated by an indirect procedure where the measured flow curve, that is the steady shear stress versus shear rate data, is extrapolated to the zero shear rate and the yield stress is determined as the shear stress intercept as shown in figure 3.3a. The extrapolation is typically done by fitting a viscoplastic model, most commonly the Bingham equation 2.1, on the measured data [47, 67–69]. Yielding of MR fluids happens in three different stages as discussed in section 2.3.1. The yield stress determined by an indirect procedure is the dynamic yield stress that is the stress needed to continuously break the particle structures. The direct measurement of the yield stress is done by evaluating the stress needed to initiate the flow. The procedure produces the static yield stress that generally has a lower value than the dynamic yield stress [70]. The static yield stress is also called as frictional yield stress, since many times the yielding happens by slipping of the particles on the measuring geometries rather than by actual rupture of the particle structures [19, 71].

The yield stress of MR fluids has been determined directly by fixed shear rate (also called static torque) [67, 72], stress ramp (also called stress sweep and breakaway) [56, 67, 70, 72] and strain sweep [67, 72, 73] tests. In the stress ramp test, which is the most common procedure with MR fluids, the shear stress is increased at a constant rate from zero to a level above the yield stress and the imposed deformation is recorded. When the shear stress exceeds the yield stress, the strain or the strain rate slope shows a rapid increase, which indicates the onset of the flow as shown in figure 3.3b. The static yield stress is determined by fitting a linear curve on the last few data points of the test and extrapolating it to zero strain or strain rate.

The yield stress can also be evaluated from the oscillatory measurements that are conducted as a function of increasing strain/stress amplitude [43, 74]. The critical stress recorded at

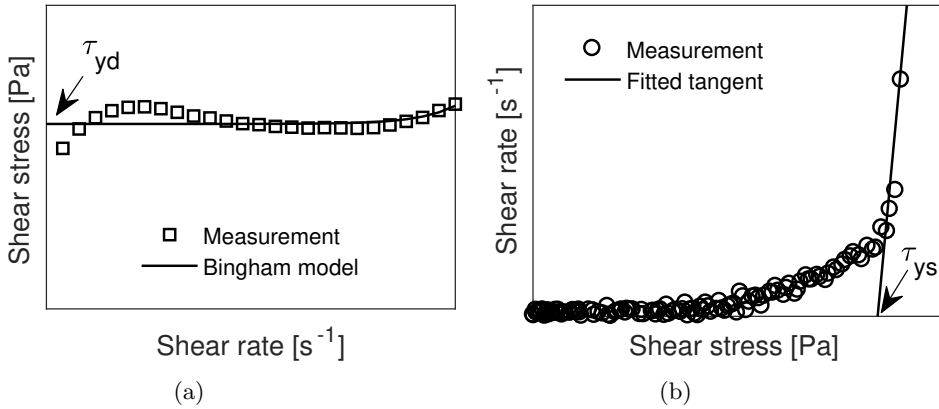


Figure 3.3: The dynamic yield stress τ_{yd} determined by fitting of the Bingham model (a) and static yield stress τ_{ys} by the stress ramp procedure (b).

the crossover point of the storage and loss moduli has been used as one estimate of the yield stress, but there are other possibilities as well. If the results of the amplitude sweep are plotted against the stress amplitude, both the storage and loss moduli exhibit a rapid decrease at a value corresponding closely to the yield stress [43]. The procedure should be used with care, since the critical stress does not always coincide well with the yield stress estimated by other methods and it may depend strongly on the frequency [75]. However, Laun et al. demonstrated that with MR fluids the frequency dependence is typically small [43].

3.1.3 Off-state measurements

When the magnetic field is not applied, the viscosity of the MR fluid is too low to remain in the gap between the plates. Therefore the off-state viscosity of a MR fluid is commonly measured using a concentric cylinder geometry, where the specimen is contained in a narrow gap between two cylinders. The inner cylinder with radius R_i is typically rotating while the outer cylinder with radius R_o remains stationary. The shear stress and rate are rather uniform in the gap and therefore, the rheological properties of the non-Newtonian fluids can also be determined directly without corrections in a following way [76]:

$$\dot{\gamma} \approx \frac{R_o \Omega}{R_o - R_i} \quad (3.9)$$

$$\tau \approx \frac{M}{2\pi R_i^2 h_c} \quad (3.10)$$

Here, h_c is the height of the inner cylinder.

3.1.4 Wall slip

Rheological measurements are based on the assumption that the measured fluid does not slip on the measuring geometry. If slippage occurs during measurements, the measured values are smaller than the true values and wrong conclusions could be drawn from the results. Sometimes the slippage may appear as jumps or sudden changes in the slope of the flow curve. The wall slip is a common problem when measuring rheological properties of any

suspensions. Its effect becomes more pronounced when the fraction of the solid particles or particle size increases [77]. The wall slip can appear in two forms: true and apparent. The true wall slip happens when the adhesion between the sample and the surface of the measuring geometry fails. The apparent wall slip occurs with suspensions when the suspended particles are displaced away from the measuring surfaces forming a depleted layer of lower viscosity fluid on them. The velocity gradient within this "slip layer" is high; it acts as a lubricant between the wall and the bulk suspension. The apparent wall slip should not exist with MR fluids under strong magnetic fields when the particle structures are gap spanning, since they develop normal forces that should prevent formation of the slip layer [78].

The wall slip is commonly studied with plate-plate geometry by changing the gap height. When the wall slip exists, the measured values should become higher when the gap height is increased as more bulk suspension is being deformed, which has a greater effect on the measurement [79]. It should be noted that with MR fluids the gap height may also influence on the fluids structure and therefore, the interpretation of the results should be done with more care. Lopez-Lopez et al. reported that the strength of the MR fluid becomes stronger with increasing gap height in the pre-yield region, but the effect disappears when the fluid begins to yield as no gap dependence was observed at static and dynamic yield stresses [78]. de Vicente et al. used significantly lower magnetic field strengths in their study and reached similar conclusions about the dynamic yield stress, but the static yield stress decreased with increasing gap height [80]. This was postulated to be caused by the wall slip.

The wall slip can also be studied by using measuring plates with different kind of surface properties, like smooth and rough or otherwise textured surfaces. The measured values should be the same, if slippage exist in neither cases. The roughened surfaces can typically eliminate the slippage of MR fluids effectively [78, 80–82]. The application of an external magnetic field may prevent formation of the slip layer if the particle structures are gap spanning. However, if the surface roughness is smaller than the particle size the particles may still slip on the surface, since the attractive magnetostatic forces between the particles are typically higher than friction forces between the particles and the measuring surface. When the surface roughness is higher the particles are pushed in the defects where they become trapped and the slippage is prevented [21, 22]. The slipping of the MR fluids can also be prevented by using magnetic surface materials instead of non-magnetic as the attractive magnetostatic forces will exist also between the magnetic plate and magnetic particles [21, 22].

The dispersion of the magnetic particles may also affect the wall slip. Caballero-Hernandez et al. reported that wall slip had greater impact on static and dynamic yield stresses of agglomerated than well dispersed MR fluids at low magnetic field strengths [82]. Both measured yield stresses increased at moderate field strengths when rough measuring plates were used instead of smooth ones, but the impact was stronger for the static yield stress.

4 Experimental

This chapter introduces the materials and the methods used in the present study.

4.1 Materials

Table 4.1 shows the composition of the MR fluid specimens used in this study. The Lord MRF-132DG specimen, which was used in publication I, is a commercial product and therefore, the precise composition is unknown. The carrier fluid is a hydrocarbon oil and the solid fraction is about 32 vol-%. It is likely that the fluid also contains additives.

Table 4.1: MR fluid specimens

Specimen	Particle vol-%(M/N) ¹	Microparticle Grade	Nanoparticle Type	Carrier fluid vol-% - Type ²	Lecithin vol-%
Lord	32 (100/0)	-	-	68 - HO	N.A.
1	32 (100/0)	BASF OM	-	68 - SO	-
2.1	15 (100/0)	BASF HQ	-	85 - SO	-
2.2	15 (95/5)	BASF HQ	Nanofer	83 - SO	2
2.3	15 (90/10)	BASF HQ	Nanofer	83 - SO	2
2.4	15 (100/0)	BASF HQ	-	85 - IL	-
2.5	15 (95/5)	BASF HQ	Nanofer	85 - IL	-
2.6	15 (90/10)	BASF HQ	Nanofer	85 - IL	-
3.1	15 (100/0)	BASF HQ	-	83 - SO	2
3.2	15 (95/5)	BASF HQ	$\gamma - \text{Fe}_2\text{O}_3$ 1	83 - SO	2
3.3	15 (95/5)	BASF HQ	$\gamma - \text{Fe}_2\text{O}_3$ 2	83 - SO	2

¹ M/N=relative volume fractions of the micron- and nano-sized particles

² HO=Hydrocarbon oil, SO=Silicone oil, IL=Ionic liquid

4.1.1 Carrier fluids

Rhodorsil 47 v 50 Silicone Oil (SO) was used as the carrier fluid in most of the MR fluid specimen. It has a viscosity of 48.6 ± 2.4 mPa ·s and the density 0.96 g/cm³. Silicone oil was chosen as a carrier fluid because of its availability at various precise viscosities. The use of surfactants to improve dispersion of iron particles in silicone oil has been already studied and therefore, a guideline to prepare well dispersed suspensions was available [83].

The ionic liquid 1-ethyl-3-methylimidazolium diethylphosphate by Merck was used in three MR fluid specimens. It has a viscosity of 317.6 ± 16 mPa ·s and density of 1.14 g/cm³. The grade was chosen based on earlier work by Gómez-Ramírez et al., they found that it provided high stability against aggregation [35].

4.1.2 Particles

Micron-sized magnetic carbonyl iron particles were BASF OM and HQ grades. Based on the manufacturer information the particle diameter (d_{50}) of the OM grade varies from 3.9 to 5.2 μm and with HQ grade it is 2 μm .

Nanofer Star particles were supplied by NANO IRON s.r.o.. The particles are composed of zero-valent iron and are surface stabilized against oxidation with FeO – Fe₃O₄ double shell. Based on the supplier specifications the mean particle diameter is 50 nm (20-100 nm).

The γ – Fe₂O₃ nanoparticles were synthesized by LFS method. The precursor for the particles was ferrocene (Fe(C₅H₅)₂, Alfa Aesar 99%) dissolved in xylene (VWR, technical grade), with metallic concentration of 29 mg(Fe)/ml. Two precursor feed rates 3.0 and 8.3 ml/min were used that resulted in 7.9 and 16.6 nm average particle diameters, respectively.

4.1.3 Additives

Lecithin (VWR, soy based) was chosen as a surfactant for the nanoparticles to improve the dispersion stability. The concentration of the lecithin in the MR fluid specimen was determined based on the literature, calculations and preliminary tests. The amount of lecithin needed for 100% coverage of nanoparticles was calculated based on the known absorption density of oleic acid ($2 * 10^{18}$ mol/m² [83]) and the specific surface area of the particles calculated by their density and average diameter. This gave only a rough estimate of the needed concentration that was studied further by the preliminary tests.

4.2 Sample preparation

In publication II the specimen 1 was prepared by first mixing the micron-sized particles into the silicone oil by hand. The suspension was then placed into ultrasonic bath for half an hour to improve the dispersion of particles.

In publication III the specimens 2.1-2.6 were mixed with a high shear rate mixer at 2000 r/min for 20 min while held in a ultrasonic bath to promote mixing. With specimens 2.5 and 2.6 that contained lecithin the carrier fluid and lecithin were premixed with a high shear rate mixer for 20 min before addition of the particles.

In publication IV the nanoparticles were first mixed with silicone oil and lecithin by a sonicator (Qsonica, Q700). The total sonication time was 30 min that resulted to about 165 kJ total energy input (the specimen volume was 20 ml). Since the energy input per volume is high the specimen heats up and for that reason, the sonication was done in cycles to avoid overheating. The specimen was first sonicated for 10 s and then let rest for 30 s. The cycle was repeated until 30 min total sonication time was reached. In addition the mixing pot was cooled with 3 °C liquid circulation from the outside. The micron-sized particles were added into the suspension after the sonication and the sample was mixed with a high shear rate mixer at 2000 rpm for 30 min.

4.3 Characterization techniques

4.3.1 Rotational rheometer

The rheological properties of the MR fluid samples at on- and off-state conditions were measured with Anton Paar MCR301 rotational rheometer. For the on-state measurements the rheometer was equipped with a MRD180/1T magneto-cell that applies a plate-plate measuring geometry. The structure of the magneto-cell is illustrated in the figure 4.1.

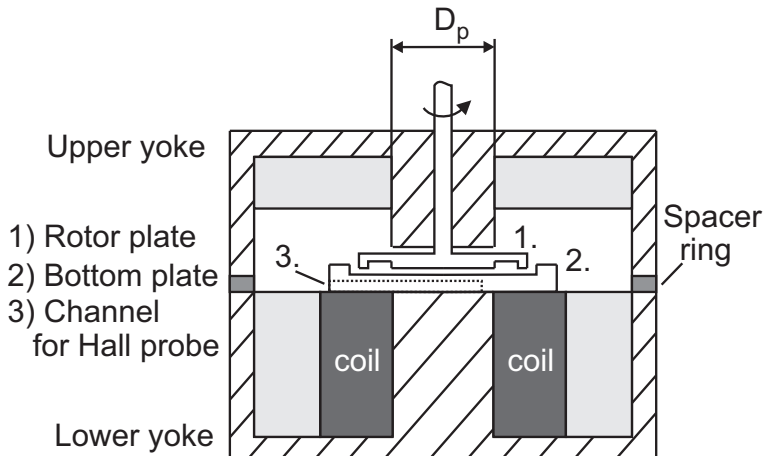


Figure 4.1: Schematics of the magneto-cell.

The cell creates a vertical and rather homogeneous magnetic field into the measuring gap. The magnetic field strength can be adjusted by controlling the current that passes through the field generating coil. The resulting magnetic flux density may be measured with a Hall-probe from a channel that is machined to the bottom plate underneath the measuring gap. The radial position at which the magnetic flux density was typically measured was 6 mm from the plate rim. The magneto-cell tends to heat up at high currents, which may affect the results. Therefore, the temperature during measurements was held at 30 °C by liquid circulation. The measurements were done using various plate materials and surface finishes; the original Anton Paar geometry was used only in the research that was reported in the publication I and all the rest were measured with custom made geometries. The custom made bottom plate was slightly thicker than the original (1.8 mm vs. 2.2 mm). Therefore the upper yoke was raised by 0.5 mm with a thicker than original ferromagnetic spacer ring. The change in the configuration resulted to about 30% lower maximum magnetic flux density in the measuring gap than with the original design.

The on-state tests were done with different magnetic flux densities to determine the yield stresses and to evaluate how the magnetic field strength affects the microstructure of the MR fluids. The test types were constant shear rate (publications I-IV), stress ramp (publications I-III) and oscillatory tests (publications I and IV). In the constant shear rate tests the sample was first sheared at 0.001 1/s until steady state conditions were reached and the first data point was measured. The shear rate was then increased in logarithmic steps and the next data points were measured from each step in a similar manner until the shear rate range from 0.001 to 100 1/s was covered. In the stress ramp tests the shear stress was increased logarithmically from a very low value to a level well above yield point. The

oscillatory tests were done in the amplitude sweep mode with 1 (publications I and IV) and 5 rad/s (publication I) angular frequencies. The strain amplitude ranges were 0.1-10% (publication I) and 0.1-100% (publication IV).

As the viscosity of the MR fluids without magnetic field is rather low, a concentric cylinder geometry was used to measure the viscosity of the specimen at these off-state conditions. The concentric cylinder offers a better sensitivity for the measurement as it has higher contact area between the sample than the plate-plate geometry. The inner rotating cylinder had a rough surface finishing to eliminate possible wall slip that may occur with suspensions. The viscosities were measured with constant shear rate tests that had two phases: first the shear rate was increased from 0.01 to 1000 1/s and then decreased back to 0.01 1/s in logarithmic steps.

4.3.2 SQUID magnetometer

The magnetic properties of BASF HQ, Nanofer Star and $\gamma - \text{Fe}_2\text{O}_3$ particles in publications III and IV were measured with Quantum Design MPMS XL magnetic property measurement system. The virgin magnetization of the particles was measured as function of the magnetic flux density B from 0 to 1 T. The magnetic hysteresis curves were recorded from -2.5 to 2.5 T. All measurements were done at 10 and 300 K temperatures.

4.3.3 Sedimentation measuring system

The sedimentation of the MR fluids was studied with an in-house build measuring system. When the MR fluid specimens were stored in test tubes and held in static fixture, there was formation of an interface between the clear carrier fluid and particle suspension that was descending as the sedimentation proceeded. This interface was tracked optically by taking digital images from the test tubes with 60 minute interval up to 800 h. The final images were taken after 10 000 h when the settling had ended to determine the packing density of the particles. The images were analysed with Matlab® software after they had been converted to gray scale. The Matlab script detects the interface between the clear carrier fluid and the suspension numerically; as the gray scale values are scanned in the vertical direction of the test tube there is a steep gradient in the values at the interface as illustrated in figure 4.2. The red box illustrates the area that was scanned and the green line shows the interface position detected by the script. The interface positions were then plotted as a function of time based on the image date and time informations.

4.3.4 Electron microscopy

The size and morphology of the nanoparticles was studied by electron microscopy. The size and shape of the particles were evaluated from the Transmission Electron Microscope (TEM) images by randomly selecting 200 particles from the images and measuring the diameters. The agglomeration and aggregation was studied from both TEM and Scanning Electron Microscope (SEM) images. Since the area of the TEM images is extremely small the SEM images gave a better view of the overall situation. The samples were prepared by mixing small fractions of nanoparticles with ethyl alcohol, pouring mixture on TEM grid and letting the alcohol evaporate. The sample preparation had its challenges as the particles tend to agglomerate when the alcohol evaporated regardless of their original dispersion in the fluid. The TEM images were acquired using JEOL JEM 2010 operating at accelerating voltage of 200 kV. The SEM images were taken with Zeiss ULTRApplus operating at accelerating voltage of 3.0 kV.

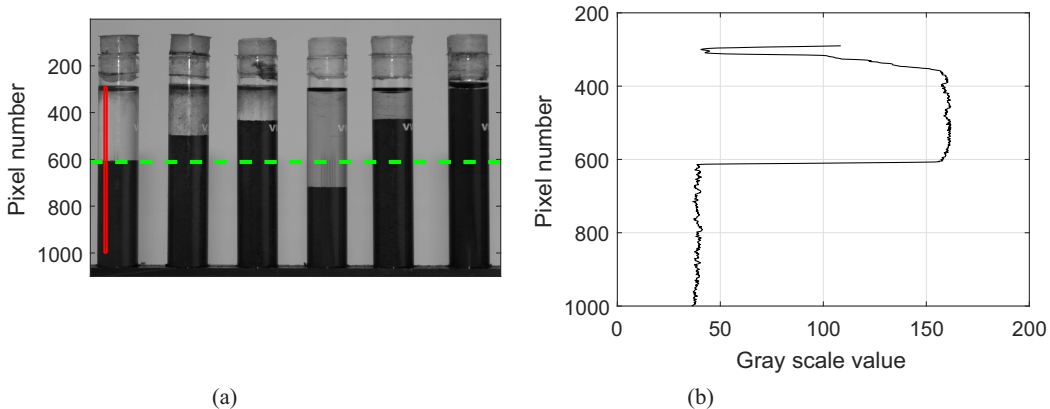


Figure 4.2: The Matlab scripts detects the clear carrier fluid particle suspension interface based on the steep gradient of the images gray scale values.

4.3.5 X-ray diffraction

The composition of the nanoparticles was studied with the X-ray powder diffraction (XRD). The measurements were done with Panalytical Empyrean Multipurpose Diffractometer using Cu $K\alpha$ radiation ($\lambda = 1.5405 \text{ \AA}$) and 45 kV and 40 mA cathode voltage and current, respectively.

4.3.6 Raman spectroscopy

Raman spectroscopy was used to study the composition of the iron oxide nanoparticles further, since $\gamma - \text{Fe}_2\text{O}_3$ and $\text{FeO} - \text{Fe}_3\text{O}_4$ can not be reliably distinguished by XRD. Raman spectra were measured with Andor Shamrock 303 spectrometer and Andor Newton 940P cooled CCD detector. The wavelength of the excitation laser was 532 nm. Since the heating of the iron oxide can cause phase conversion the laser power level was kept low during the measurements.

5 Results and discussion

This chapter summarises the most important findings of the publications I to IV. Some previously unpublished findings are also presented. Publications I and II concentrate on developing the measuring practice and equipment to correctly measure the properties of MR fluids. The focus on publications III and IV is to modify the MR fluid composition to achieve better sedimentation stability.

5.1 Effect of the measuring method on the measured yield stress

The yield stresses were determined using direct and undirect procedures and oscillatory measurements at 33, 118, 255, 386, 513 and 634 mT magnetic flux densities. More precisely the used procedures were stress ramp and steady shear rate tests and determination of the maximum elastic stress. The maximum elastic stress is the in-phase stress component of the stress response and is defined as the product of the storage modulus and the strain ($G'\gamma_0$). The flow curves from the steady shear rate tests were extrapolated to the zero shear rate by two parameter Bingham and three parameter Herchel-Bulkley equations. The Herchel-Bulkley equation is defined as

$$\tau = \tau_y + K\dot{\gamma}^n \quad (5.1)$$

where K is the consistency factor and n is the power law index. The fit of the Bingham and Herchel-Bulkley equations on the measured data are illustrated in figure 5.1. Generally speaking the two equations perform fairly similarly, but the Bingham equation gives a slightly higher estimate for the dynamic yield stress. The difference is more apparent at low magnetic flux densities (33 and 118 mT) where the the Herschel-Bulkley equation fits better on the measured data.

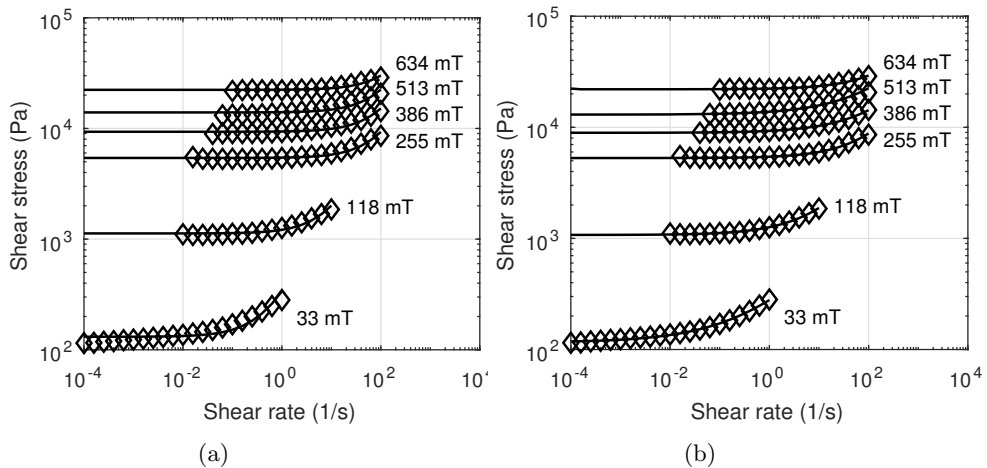


Figure 5.1: Bingham (a) and Herschel-Bulkley (b) equations fitted on the data measured for the Lord MRF-132DG specimen.

The shear stress increase rate of the stress ramp test affected the static yield stress. The effect was studied with 513 mT magnetic flux density by increasing the shear stress in a stepwise manner logarithmically with 200, 100 and 50 steps per decade while keeping the measuring time at 3 seconds per a step. The yield stress was higher with lower ramp rate as shown in figure 5.2. Yang et al. have also observed that a higher increase rate in strain (or stress) results to a lower measured yield stresses [72]. Initially the results suggested that longer exposure to the magnetic field might lead to a stronger particle network giving rise to a higher yield stress. However, keeping in mind that the MR effect is extremely fast and the static yield stress is the stress needed to initiate the flow, a more probable explanation is that at lower ramp rates the particle structure has time to adapt to the exposed strain by reforming the broken chains, which shifts the initiation to a slightly higher stresses. The moderate ramp rate of 100 points per decade was chosen for rest of the measurements.

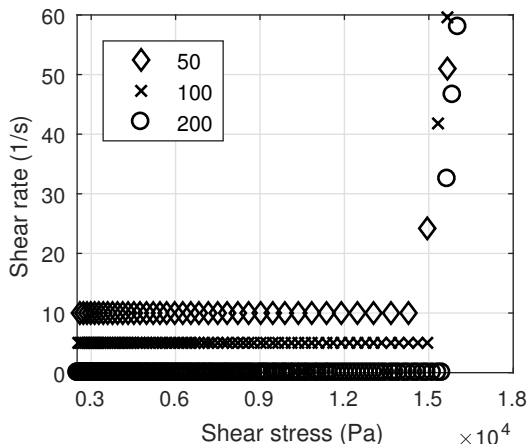


Figure 5.2: The effect of the ramp rate on the static yield stress of Lord MRF-132DG. The 50 and 100 points per decade curves are shifted vertically for better clarity.

In the oscillatory measurements the G' and G'' were determined as a function of the strain amplitude. The moduli showed a short linear region at low amplitudes where they remained virtually independent of the amplitude as shown in figure 5.3a. The G' is significantly higher than G'' that indicates predominantly solid like behaviour. Eventually the linear region ends that is seen as steady decrease in G' and peaking of G'' after which it also begins to decrease. The peaking is called strain overshooting, which has been witnessed with electrorheological (ER) and MR fluids before [84–86]. It is caused by reformation of the particle networks; G'' increases as extra energy is dissipated when old particle structures break and new ones are formed. G'' starts to decrease when the formation of the new structures is hindered at higher strain amplitudes (and shear rates) and the structure breaks into smaller agglomerates [86].

The yield stress can be estimated from the various points of the curves; for example the stress amplitude values at the inflection point of G' or at the cross over point of G' and G'' have been used before. Here the yield stress was denoted as the maximum of the elastic stress, which is an unambiguous method and has shown a good correspondence to the values from the direct and indirect procedures for gels and suspensions [87, 88]. The method how the yield stress is obtained from the oscillatory data will likely affect its value and how it compares with static and dynamic yield stresses.

It is known that the angular frequency may affect the results of the oscillatory measurements [84]. Therefore, the frequency dependence was studied at 255 mT by performing the measurements with 1 and 5 rad/s angular frequencies. As seen from the figure 5.3b the maximum of the elastic stress increases with the frequency. Because of this the usability of the oscillatory measurements to determine the yield stress has been questioned by some authors [75]. However, as previously has been shown the measurement parameters can also affect the yield stresses determined from the direct measurements as well. The 1 rad/s frequency was chosen for the following measurements.

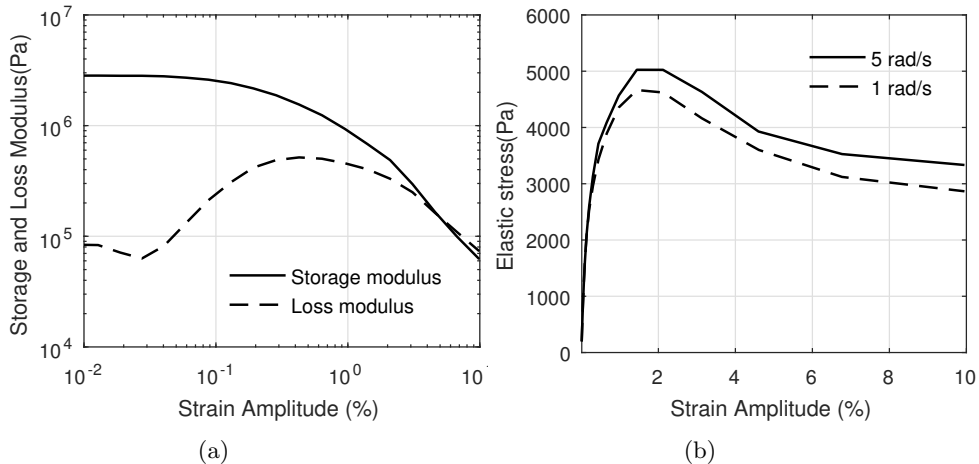


Figure 5.3: Loss and storage modulus for Lord MRF-132DG as function of the strain amplitude (a) and frequency dependence of the elastic stress (b) at 255 mT magnetic flux density.

The yield stresses determined by different procedures are plotted in figure 5.4. The values are averages of two measurements and the standard errors are illustrated by the error bars. The yield stresses increase as a function of the magnetic flux density and follow the power law as expected. The power law index is about 1.7 for direct and 1.6 for indirect procedures at moderate flux densities (386-634 mT), which are quite well in line with 1.5 predicted by the equation 2.4. The power law index for the oscillatory measurements is 1.9; the yield stress is at about the same level with other procedures at low flux densities, but increases faster with the flux density. The yield stresses from the stress ramp measurements are generally the lowest. As previously discussed the yield stresses determined by direct and indirect procedures are the static and dynamic yield stresses. Therefore, it is not expected that the values would be the same. Typically the dynamic yield is higher than the static [67, 70, 71].

The extrapolation of the flow curves by the Bingham or Herchel-Bulkley models proved to be rather straightforward and reliable procedure with typical scatter of results less than 10%. The stress ramp procedure offered the lowest scatter, which was generally less than 5%, but the value was effected by the ramp rate. Similar drawback was observed with oscillatory measurements where the value was frequency dependent. It should be noted that especially the measured value of the static yield stress may be affected by the wall slip. Here the existence of the wall slip was studied by a common procedure where the gap height was changed and the measured values were compared. It appeared that the wall slip was non-existing as the curves coincided. However, as show later in section 5.2, this procedure

fails to reliably indicate the existence of wall slip with MR fluids. Therefore, the possibility of wall slip cannot be completely excluded.

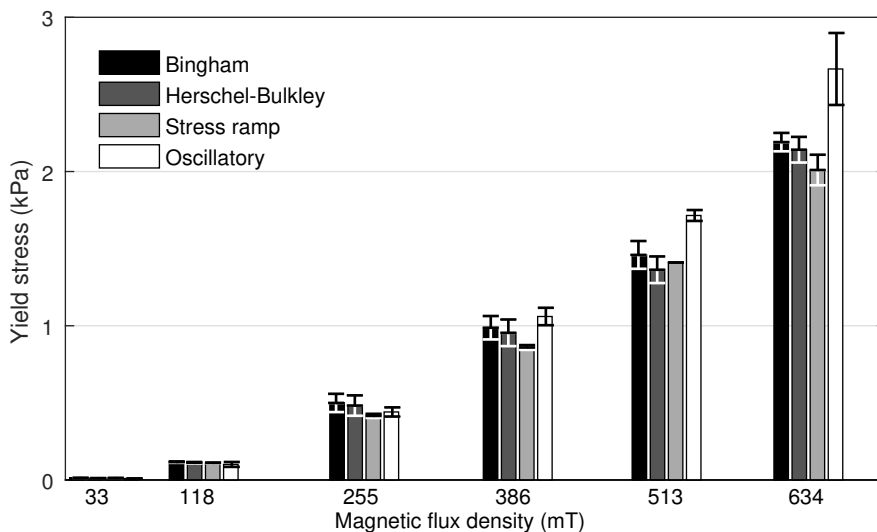


Figure 5.4: Yield stresses of the Lord MRF-132DG specimen determined by different procedures.

5.2 Effect of the plate properties and measuring gap height on the measured yield stress

The effect of the plate surface material and roughness on the static and dynamic yield stresses was studied with a set of custom made plate-plate geometries. The plate materials were paramagnetic aluminium and ferromagnetic iron and the roughness was either smooth ($R_a \sim 0.3 \mu\text{m}$) or rough ($R_a \sim 10 \mu\text{m}$). The custom geometry was designed in a way that the steel adapter part remained the same while the plate part was changeable and made of aluminium as shown in figure 5.5. With magnetic geometries a 0.2 mm thick ferromagnetic plate was embedded into the aluminium plate as shown in figure 5.6.



Figure 5.5: The plate part with and without the adapter.



Figure 5.6: Custom plates from the left: smooth non-magnetic, rough non-magnetic, smooth magnetic, rough magnetic.

Since the particle size of the MR fluid was $3.9\text{-}5.2\ \mu\text{m}$, the rough surface should be able to eliminate the wall slip. A customary procedure to detect the wall slip with plate-plate geometry has been the comparison of the flow curves at different gap heights [79]. The procedure was adopted also in here to study if the wall slip of MR fluids could be detected by such way. Therefore, all rheological measurements were done with 0.25, 0.50 and 1.00 mm gap heights.

5.2.1 Modelling and measurement of the magnetic flux density profile with different measuring setups

The usage of magnetic measuring plates or different gap heights also changes the magnitude of the magnetic flux density and shape of the flux density profile in the measuring gap. These variations may cause larger changes in the yield stresses since the yield stress and the magnetic flux density have a power law relationship. In order to study just the effect of the plate surface characteristics or the gap height on the measured results, the changes in the magnetic flux density profile have to be compensated. Therefore, the flux density profile in the gap at different measuring set-ups was studied first. This was done by creating a magnetic model of the MRD180/1T magneto-cell with a finite element method magnetics (FEMM) software. The model was created mostly based on the details provided by the Anton Paar GmbH, but some material specific details had to be defined semi-experimentally based on the magnetic flux density measurements. The magnetic flux densities were measured with a FW Bell Model 5180 T meter and STD18-0404 Hall probe from a channel underneath the measuring gap as shown in figure 4.1. The radial flux density profile was measured by moving the probe with a custom made actuator from the middle of the plate towards the rim in 0.5 mm steps. The measured and simulated profiles in the measuring channel at 0.5-2.0 A coil currents are illustrated in figure 5.7. The shapes of the profiles are

quite flat, but show distinct peaking near the rim, which has been reported also by Laun et al. [20]. The agreement between the measured and simulated profiles is excellent, which validates the used model.

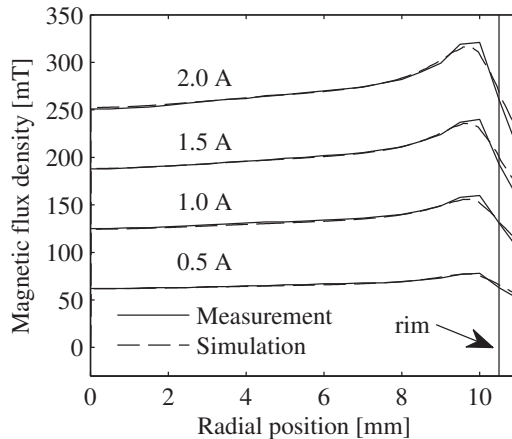


Figure 5.7: Measured and simulated radial magnetic flux density profiles in the measuring channel for the non-magnetic plates with a 0.25 mm empty gap at different coil currents.

The figures 5.8a and 5.8b illustrate the measured and simulated magnetic flux density profiles with 0.5 mm MR fluid filled measuring gap for non-magnetic and magnetic plates. The simulated values correlate well with the measured values with only 3% systematic underestimation. The difference is likely caused by slight error in the magnetization properties of the MR fluid used in the model. There are some differences in the profiles when comparing magnetic and non-magnetic plates. The magnetic flux density is higher with magnetic plates, which is expected as the amount of material with higher permeability compared to air between the upper and lower yokes is increased. Also the the shape of the profiles is different as the peaking of the flux density profile near the rim almost disappears with magnetic plates. This is an advantage as the magnetic particles tend to migrate towards higher flux density intensities over time that may cause transient changes during measurements [20, 22, 89].

Since the magnetic flux densities near the rim of the plate have the highest contribution to the torque needed to rotate the plate, the effect of the profile shapes on the measured rheological values has to be considered when comparing different plate materials. This can be done by calculating a rheology-relevant average magnetic flux density \bar{B} [22]

$$\bar{B} = \frac{\sum_0^R B(r_i) r_i^2 \Delta r}{\sum_0^R r_i^2 \Delta r} \quad (5.2)$$

where r_i is the radial position in the measuring gap. The equation takes into account that the magnetic flux density B at greater radial locations has dominant effect on the measured rheological values.

The figures 5.9a and 5.9b show \bar{B} as function of the coil current calculated based on the simulated magnetic flux density profiles in the middle of the MR fluid filled 0.25, 0.50 and 1.00 mm high measuring gaps for the non-magnetic and magnetic plates, respectively. The

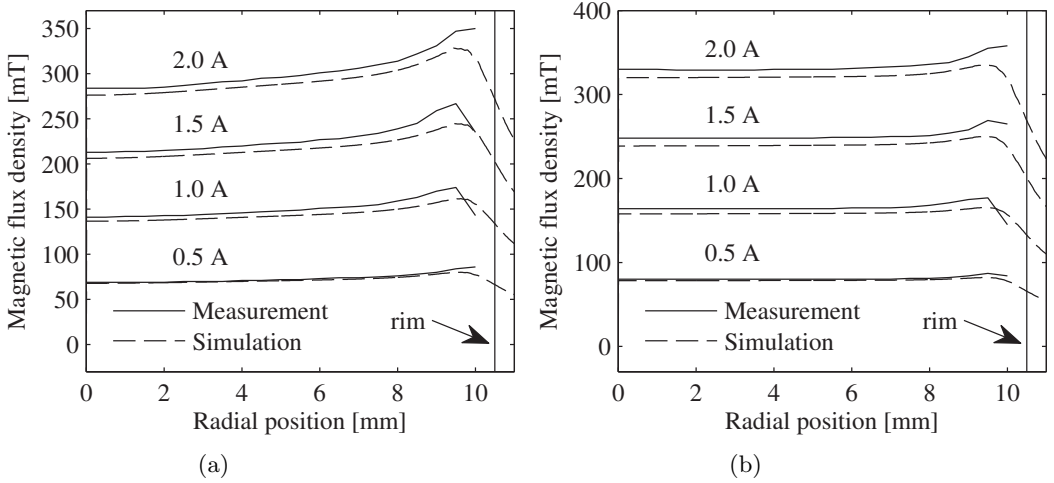


Figure 5.8: Measured and simulated radial magnetic flux density profiles with 0.5 mm MR fluid filled measuring gap for the non-magnetic (a) and magnetic (b) plates at different coil currents.

figures show that \bar{B} increases linearly with the coil current. A 0.25 mm elevation in the gap height causes about 4.5% increase in the average flux density with both non-magnetic and magnetic plates. The usage of magnetic plates yields to about 7% higher flux density values compared to the non-magnetic plates. This rise of the average flux density has to be also compensated when comparing the results of the rheological measurements with different measuring setups.

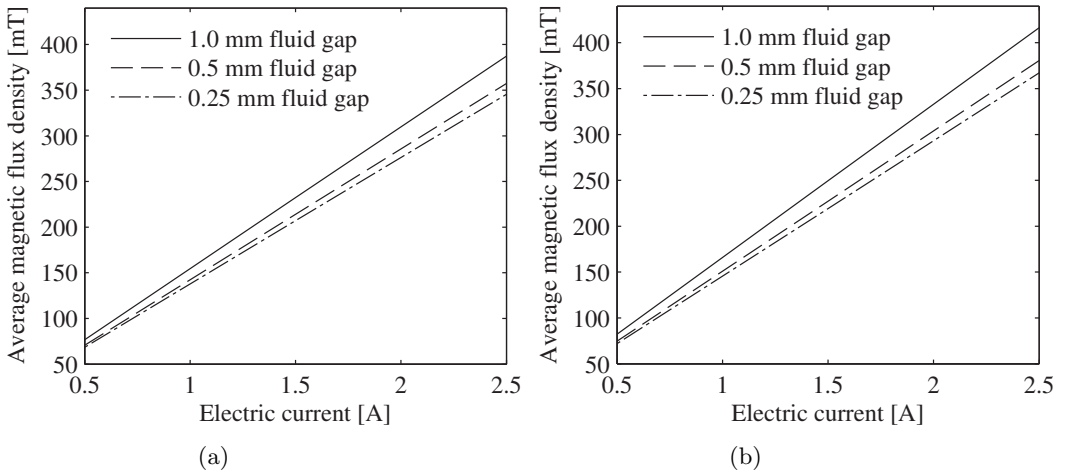


Figure 5.9: \bar{B} as function of the coil current in the middle of the MR fluid filled 0.25, 0.50 and 1.00 mm high measuring gaps for the non-magnetic (a) and magnetic (b) plates.

The yield stress of MR fluids is known to have a power law relationship with the flux density. A power law model was fitted on the measured yield stresses $\tau_{y,meas}$ as function of \bar{B} in

order to determine the power law index and the consistency factor. The power law index varied from 1.66 to 1.72 for static and from 1.78 to 1.81 for dynamic yield stresses and was highest with magnetic plates. Faster increase of the dynamic yield stress compared to the static has also been reported elsewhere [70]. The fit of the model on the measured values is generally good, but there is a slight overshoot of the static yield stress at highest coil current with non-magnetic plates as illustrated in figure 5.10a. Since similar behaviour was not observed with magnetic plates, it is likely caused by the sample-plate interface rather than by partial magnetic saturation of the particles.

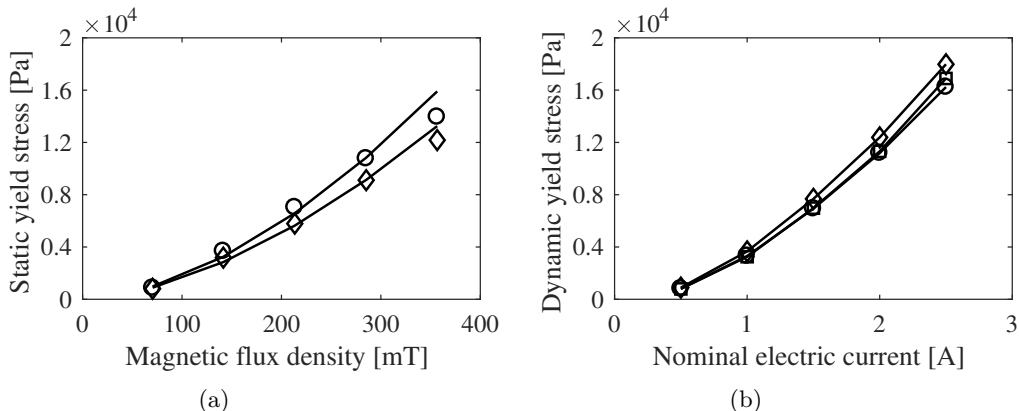


Figure 5.10: (a) The measured static yield stresses for the MR fluid containing BASF MO particles illustrated by the symbols (diamonds = smooth non-magnetic plates, circles = rough non-magnetic plates) and the modelled values by the solid lines. (b) The dynamic yield stress measured with magnetic plates (diamonds) and with calculated (circles) and manual (cubes) compensations.

As previously observed \bar{B} increases linearly with the gap height or when the plate material is changed from non-magnetic to magnetic. If \bar{B}_{ref} represents a reference value with non-magnetic plates and the smallest gap height, the \bar{B}_h , which is the \bar{B} at the same coil current, but using higher gap height or magnetic plates, can be calculated by

$$\bar{B}_h = C\bar{B}_{ref} \quad (5.3)$$

where C is a setup dependent coefficient larger than one. A theoretical change in yield stress $\Delta\tau$ caused by rise of \bar{B} can therefore be calculated by

$$\Delta\tau_y = A[(C\bar{B}_{ref})^n - \bar{B}_{ref}^n] \quad (5.4)$$

where A is the consistency factor from the power law model. An increase similar degree was expected also in the measured values

$$\Delta\tau_{y,meas} = \tau_{y,meas} \frac{(C\bar{B}_{ref})^n - \bar{B}_{ref}^n}{\bar{B}_{ref}^n} \quad (5.5)$$

The authenticity of the equation 5.5 was studied by carrying out two sets of dynamic yield stress measurements with smooth magnetic plates. In the first set the measurements were done with the same coil currents as with non-magnetic plates and the effect of the higher

\bar{B} was compensated by subtracting the value calculated by equation 5.5 from the measured yield stress. In the second set the coil current was adjusted manually in a way that the measured \bar{B} corresponded to that with non-magnetic plates. The coil currents in that case were 0.47, 0.95, 1.41, 1.88 and 2.35 A. The figure 5.10b illustrates the results. The correlation of the compensated results is excellent up to 2 A current. With highest coil current the calculated compensation is bit too strong. The comparison validates that the value from the equation 5.5 can be used to reasonably compensate the change in \bar{B} when comparing the results of the yield stress measurements with different measuring setups.

5.2.2 Effect of the plate surface characteristics on the measured yield stresses

The effect of the plate material and roughness on measured yield stresses was studied with 0.5, 1.0, 1.5, 2.0 and 2.5 A coil currents. The static yield stress was determined by a stress ramp procedure and dynamic yield stress by extrapolating the flow curve to zero shear rate with a Bingham model. Both procedures are presented in more detail in the section 3.1.1.1. The yield stresses as function of \bar{B} measured with smooth and rough plates are tabulated in tables 5.1 and 5.2.

Table 5.1: Static and dynamic yield stresses for the MR fluid containing BASF MO particles measured with smooth and rough non-magnetic plates

\bar{B} (mT)	Static yield stress			Dynamic yield stress		
	Smooth (Pa)	Rough (Pa)	Relative difference (%)	Smooth (Pa)	Rough (Pa)	Relative difference (%)
70	807	860	6	633	794	22
142	3184	3678	14	2629	3436	27
213	5789	7027	19	5193	6719	26
285	9110	10761	17	8296	10559	24
357	12175	13947	14	11513	14932	26

Table 5.2: Static and dynamic yield stresses for the MR fluid containing BASF MO particles measured with smooth and rough magnetic plates. Note that the higher \bar{B} caused by the magnetic plates has been compensated by the equation 5.5

\bar{B} (mT)	Static yield stress			Dynamic yield stress		
	Smooth (Pa)	Rough (Pa)	Relative difference (%)	Smooth (Pa)	Rough (Pa)	Relative difference (%)
70	953	1011	6	804	786	2
142	3297	3552	7	3164	3307	4
213	7132	7341	3	6745	6634	2
285	10567	10975	2	10185	10639	4
357	15237	15583	4	16071	15607	3

The static yield stresses for the Lord specimen in section 5.1 were generally lower than the dynamic yield stresses. Here they are about the same. The difference might be partly caused by higher friction between CI particles and aluminum than CI particles and titanium. However, a more likely explanation is based on the dispersion of the CI particles; it

has been shown that well dispersed particles develop slightly higher dynamic yield stresses and slightly lower static yield stresses than agglomerated particles [83]. The commercial Lord specimen probably has additives that improve dispersion of the particles while the specimen in here has none and therefore, the particles may agglomerate due to remanent magnetization and van der Waals attractions.

As seen from the results at table 5.1, the roughening of the non-magnetic plates leads to a notable increment in both static and dynamic yield stresses. This is likely caused by elimination of the wall slip. The increase is higher in dynamic yield stress, where the relative difference between smooth and rough plates is from 22 to 27%, while it is from 6 to 19% in static yield stress. A probable explanation for the difference is associated with the particle chain structures in the measuring gap. The measurement of static yield stress happens at no-flow conditions, where the particle structures are gap spanning causing strong normal forces that push the particles against the measuring plate surfaces [90,91]. Since the friction between the smooth plate surface and the particles is probably already quite high due to these normal forces the roughening provides only a modest increase in measured values. The dynamic yield stress is measured when the MR fluid is flowing and the particle structures are broken up into smaller clusters. The structures are no longer gap spanning, which is seen as decrease in the normal forces [90,91]. Since the normal forces are smaller, also the frictional forces between the smooth plate surface and the particles are smaller and the wall slip may happen at lower stress level. The situation changes drastically when the surface is roughened, since the particles can be mechanically locked in the surface defects and the deformation happens more likely by breakage of particle chain structures near the surface rather than by slipping of the particles on the surface. Consequently, the roughening provides a more notable increment in the dynamic than static yield stress. The yield stresses measured with smooth magnetic plates are about 12% higher than with rough non-magnetic plates to start with, but after the 7% higher \bar{B} has been compensated the values are almost the same, as seen from the table 5.2. The roughening of the smooth magnetic plates does not cause a significant increase (normally less than 5%) in the measured values. The strong magnetostatic forces between the magnetic particles and magnetic plates already prevent the slippage and therefore, the roughening does not provide any further increase.

5.2.3 Effect of the gap height on the measured yield stresses

The effect of the gap height on measured yield stresses were measured at 0.5, 1.5 and 2.5 A coil currents and with 0.25, 0.50 and 1.00 mm gap heights. The measured values are expected to grow when the gap height is raised in cases where the wall slip is present as demonstrated by Yoshimura and Prud'homme [79]. The measured static and dynamic yield stresses as function of the gap height at 1.5 A coil current are presented with continuous lines in figures 5.11a and 5.11b, respectively. Both yield stresses increase with increasing gap height in almost all cases. This is a bit unexpected, since based on the results of the previous section there should be no slippage with magnetic plates. However, it should be noted that the \bar{B} also increases about 4.5% when the gap height is raised by 0.25 mm as illustrated in figure 5.9. Based on equation 5.4 the increase in \bar{B} leads to 17-21% increase in yield stress when the gap height raised from 0.25 to 1.00 mm. When the value from the equation 5.5 is subtracted from the values measured with magnetic plates the gap dependency almost disappears as illustrated by the broken lines in figures 5.11a and 5.11b. For the non-magnetic plates a similar subtraction typically leads to decrease in yield stress with increasing gap height. Interestingly de Vicente et al. also observed a decrease in static yield stress with increasing gap height, which they postulated to be caused by wall slip [80]. Here the decrease

could also be caused by too strong compensation of the higher \bar{B} . Judging by the results it seems that with MR fluids the comparison of the results measured at different gap heights does not provide information if the wall slip is present in the measurements or not. The finding is important, since the existence of wall slip may lead to systematic underestimation of the yield stress.

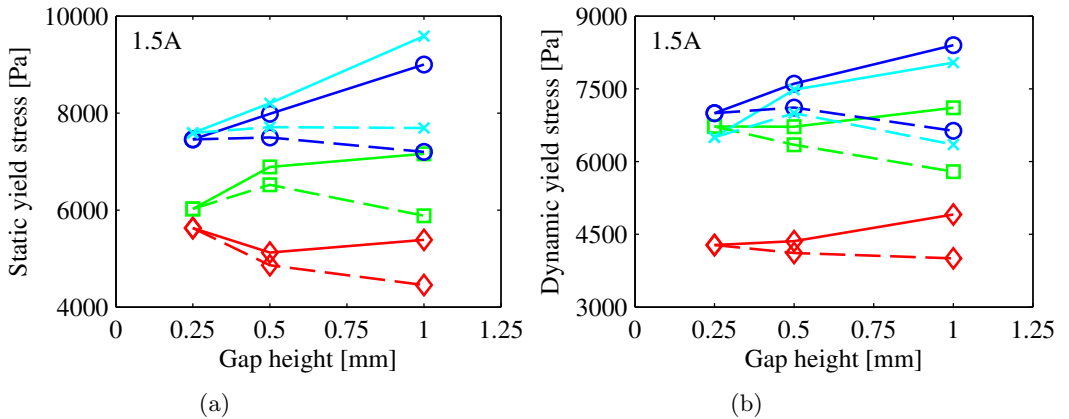


Figure 5.11: The static (a) and dynamic (b) yield stresses as function of the gap height. The continuous lines show the measured values and broken lines after subtraction of the value from the equation 5.5. Red diamonds = smooth non-magnetic, green cubes = rough non-magnetic, blue circles = smooth magnetic, light blue crosses = rough magnetic.

5.3 Properties of the bidisperse magnetorheological fluids

The effect of the carrier fluid on the properties of MR fluid was studied by dispersing micron-sized (BASF HQ) carbonyl iron particles and Nanofer Star nanoparticles into SO and IL. The nanoparticle fraction was varying from 0 to 10% while the total particle concentration was kept at 15 vol-%. Lecithin was used as a surfactant for the nanoparticles in the SO based MR fluids to avoid agglomeration.

5.3.1 Properties of the particles

The morphology of the nanoparticles was studied from the TEM images. The $\gamma - \text{Fe}_2\text{O}_3$ particles are shown in figure 5.12 and Nanofer Star particles in figure 5.13. Both $\gamma - \text{Fe}_2\text{O}_3$ 1 and 2 particles are spherical and have the arithmetic average diameters of 7.9 and 16.6 nm, respectively. The higher precursor feed rate during particle synthesis resulted to a larger particle size as expected. Most of the particles are clumped in clusters that is partly caused by the sample preparation. It is also evident from the images that there is no clear necking between the particles, which is characteristic for strong aggregates and could be expected for particles produced by flame spray pyrolysis. The Nanofer Star particles are more arbitrary in shape and have a considerably larger size as the arithmetic average diameter is 78.8 nm. Some Nanofer Star particles seem to be fused together forming aggregates. The exact synthesis method of the particles was unknown since the supplier was not willing to reveal the method, which they considered as a trade secret. It should be noted that all nanoparticle samples studied here have at least some particles larger than 15 nm and are

partly aggregated or agglomerated, which makes them potential to form nanoparticle halos around micron-sized particles [49].

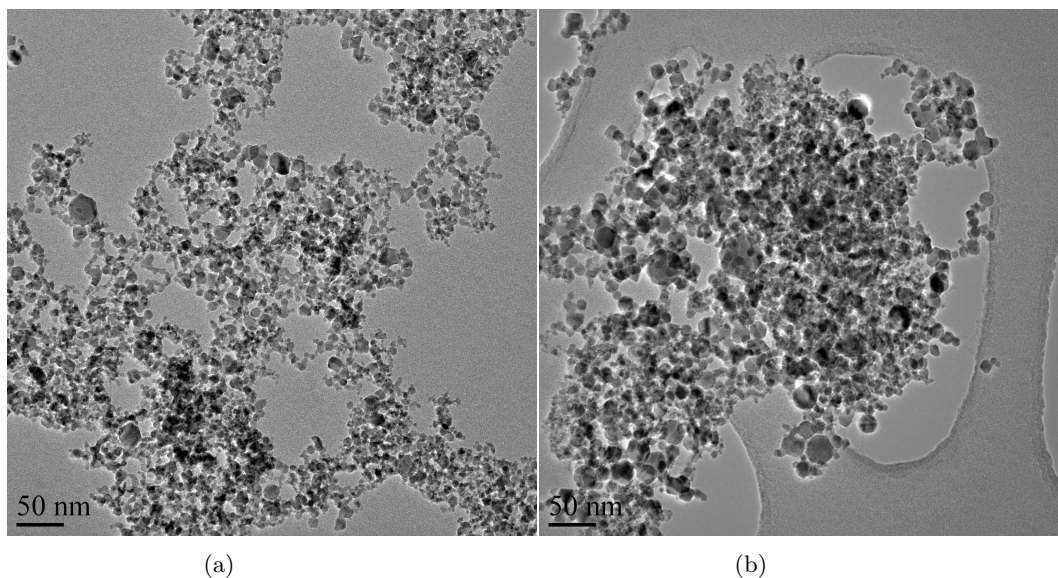


Figure 5.12: TEM images of the $\gamma - \text{Fe}_2\text{O}_3$ 1 (a) and $\gamma - \text{Fe}_2\text{O}_3$ 2 (b) nanoparticles.

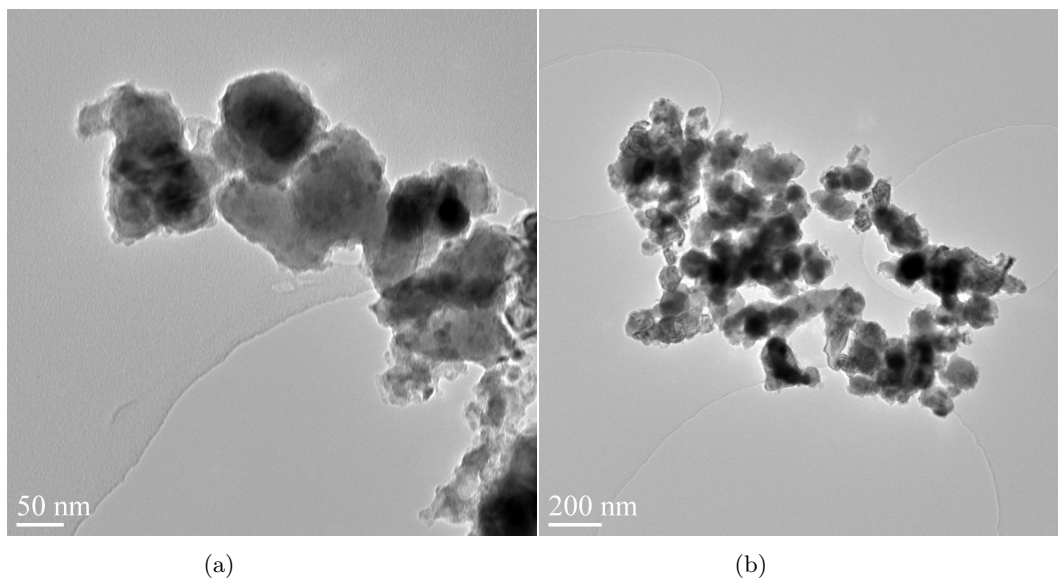


Figure 5.13: TEM images of the Nanofer Star nanoparticles with different magnifications(a) and (b).

XRD and Raman spectroscopy were used to study the composition of the particles. The XRD patterns are illustrated in figure 5.14. The peak positions for the synthesized $\gamma - \text{Fe}_2\text{O}_3$

particles can be indexed with (111), (220), (311), (400), (422), (511) and (440) planes of the inverse spinel structure of $\gamma - \text{Fe}_2\text{O}_3$. However, the compositions had to be studied further by Raman spectroscopy, since the the crystal structures of $\gamma - \text{Fe}_2\text{O}_3$ and Fe_3O_4 are so similar that reliable identification cannot be done based on the XRD data. The measured spectrum proved to have a slightly better correspondence to $\gamma - \text{Fe}_2\text{O}_3$. The peak positions for the Nanofer Star sample can be indexed with (110), (200) and (211) planes of the body centred cubic crystal structure of ferrite ($\alpha - \text{Fe}$). Based on the supplier information the Nanofer Star particles should be coated with $\text{FeO} - \text{Fe}_3\text{O}_4$ double cell, but since the $\alpha - \text{Fe}$ peaks have so high intensity, the weaker peaks are likely lost in the background noise.

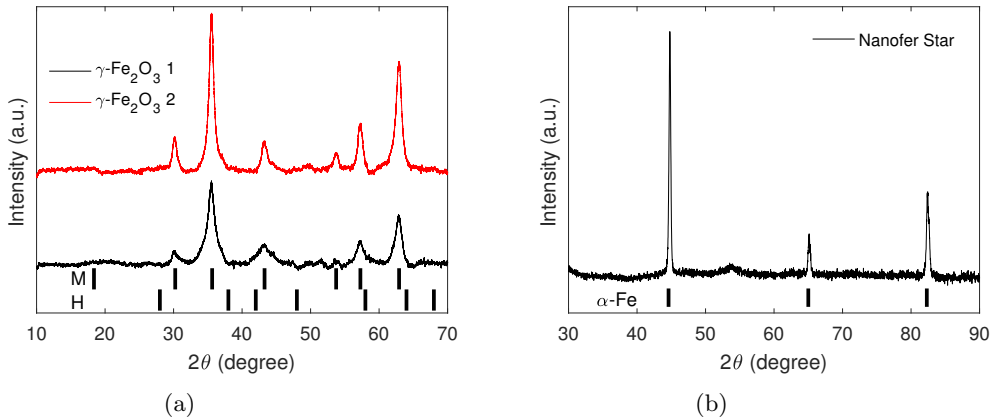


Figure 5.14: The XRD patterns of the $\gamma - \text{Fe}_2\text{O}_3$ (a) and Nanofer Star (b) particles. The characteristic peaks are marked in figures below the measured patterns, M stands for maghemite, H for hematite and $\alpha - \text{Fe}$ for ferrite

The magnetic properties of the particles were studied with SQUID magnetometry. The virgin curves measured at 300K are illustrated in figure 5.15. The saturation magnetization (M_s) of BASF HQ, Nanofer Star and $\gamma - \text{Fe}_2\text{O}_3$ 1 and 2 particles are about 227, 185, 22 and 43 Am^2/kg , respectively. M_s of micron-sized BASF HQ particles and Nanofer Star nanoparticles are considerably higher than $\gamma - \text{Fe}_2\text{O}_3$ particles as expected, since both are mostly elemental iron. The $\gamma - \text{Fe}_2\text{O}_3$ nanoparticles have clearly lower M_s than bulk $\gamma - \text{Fe}_2\text{O}_3$ (74 Am^2/kg [24]). The difference can be explained by the particle size; the particles tend to have a layer of disordered magnetic moments on the surfaces, as mentioned in section 2.2.2, which reduces the total M_s . The effect becomes stronger with decreasing particle size as the fraction of the disordered layer to the total volume of the particle increases [27]. The results are well in line with previous researches as Nurdin et al. reported M_s of 32 Am^2/kg at room temperature for Am^2/kg nanoparticles synthesized by chemical co-precipitation method [92].

Magnifications of the hysteresis loops measured at 300K between -2.5 and 2.5 T are illustrated in figure 5.16. The coercivity of $\gamma - \text{Fe}_2\text{O}_3$ particles is zero and the remanent magnetization is lacking indicating a superparamagnetic behaviour. The Nanofer Star particles however, have a coercivity of about 25 mT, which is higher than for the multidomain BASF HQ particles. A relatively large size (78.8 nm) of the Nanofer Star particles could explain the behaviour, as single domain magnetic nanoparticles that are not small enough to reach the superparamagnetic state possess high coercivity [26, 28, 29].

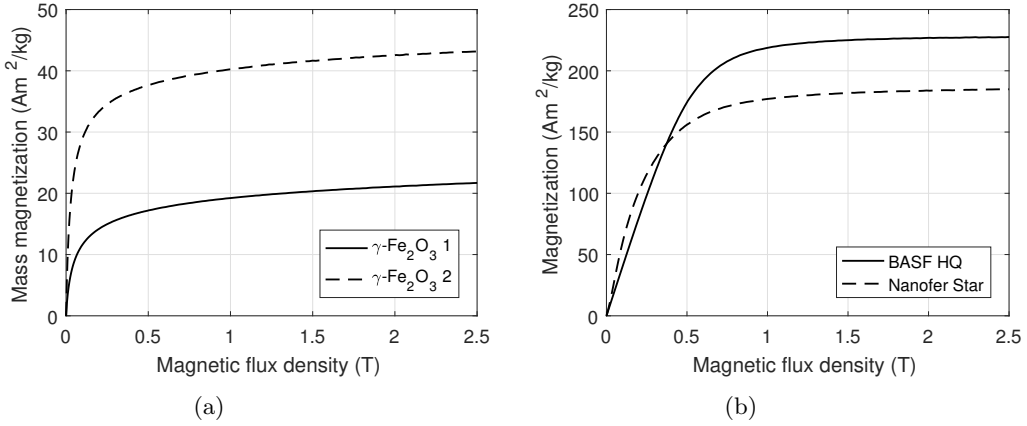


Figure 5.15: Virgin magnetization curves for the $\gamma - \text{Fe}_2\text{O}_3$ 1 and 2(a) BASF HQ and Nanofer Star (b) particles.

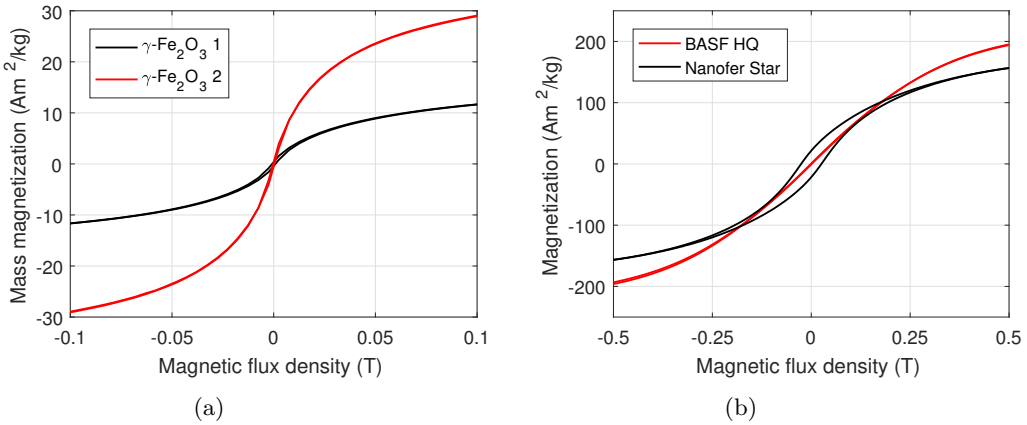


Figure 5.16: Hysteresis loops for the $\gamma - \text{Fe}_2\text{O}_3$ 1 and 2(a) BASF HQ and Nanofer Star (b) particles.

5.3.2 Field independent viscosity of the bidisperse MR fluids

The dispersion of the particles in the fluids was estimated from the viscosity curves measured with rotational rheometer without an external magnetic field. The relative viscosities determined from the measurements and theoretical predictions by the equation 2.11 are presented in figure 5.17. Only the down ramps of the measurements are shown for clarity, but it should be noted that they were practically overlapping with the up ramps. It is evident from the figures that all studied MR fluids are shear thinning, even though dilute suspensions with $\phi < 0.2$ are expected to behave in a Newtonian manner [53]. This indicates that the interactions between the particles are not just hydrodynamic, but it is likely that van der Waals and/or magnetostatic interactions exist as well. The shear thinning of the monodisperse IL based MR fluid is considerably weaker compared to SO based fluids and levels off around 100 s^{-1} where it becomes consistent with the theoretically predicted values. Corresponding predictions for the SO based fluid are clearly lower than the measured viscosities. Both the

stronger shear thinning and the deviation from the theoretical predictions implicate that the dispersion of the CI particles is poorer in SO than in IL.

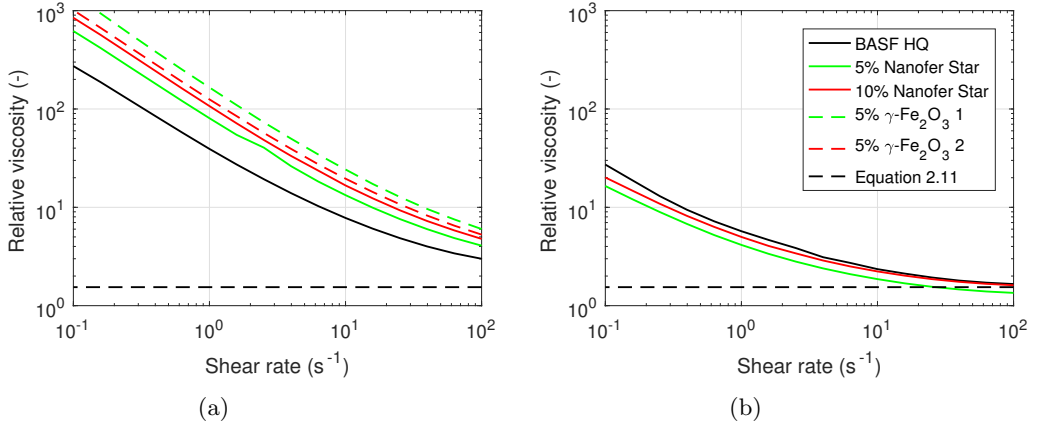


Figure 5.17: Relative viscosities of the MR fluids dispersed in (a) SO and (b) IL.

The viscosity of the SO based MR fluid increases when 5% of the micron-sized particles are replaced by the Nanofer Star nanoparticles and when the concentration is raised to 10%. The increase in viscosity seems to be related to the nanoparticle size as well, since the strongest change is observed with the smallest particles (7.8 nm $\gamma - \text{Fe}_2\text{O}_3$ 1) and the effect diminishes as the size doubles (16.6 nm $\gamma - \text{Fe}_2\text{O}_3$ 2) and decreases further when the size grows tenfold (78.8 nm Nanofer Star). Both an increase in nanoparticle concentration and decrease in particle size leads to a higher number of particles and surface area per solid content that can add drag of the particles in the carrier fluid. Contrary to the SO based fluids the viscosity of the IL based fluid decreases slightly when 5% of the micron-sized particles are replaced by Nanofer Star particles, even though the change is small.

The viscosity of ordinary well dispersed suspensions is expect to decrease when the particle distribution changes from mono- to bidisperse due to higher ϕ_m as discussed in section 2.4.1. However, an opposite behaviour has been observed for the MR fluids also before [17, 93–95]. The cause has proposed to be an increase in the surface area of particles per solid content [17, 93] or an existence of micron-sized particle agglomerates mediated by the nanoparticles [94]. The nanoparticle halos surrounding the micron-sized particles would increase the particle separation that leads to larger hydrodynamic size and higher effective particle volume fraction ϕ_{eff} expressed by

$$\phi_{eff} = \phi \left(1 + \frac{L}{r}\right)^3 \quad (5.6)$$

where L is the thickness of the nanoparticle halo.

5.3.3 Sedimentation of the bidisperse MR fluids

The sedimentation curves for the MR fluid specimen are illustrated in figure 5.18. The sedimentation behaviour was compared based on the sedimentation rate and particle packing density after settling. The sedimentation rate was determined by calculating the average

interface travel velocity between 0 and 100 h. The packing density (PD) of the particles was determined by

$$PD = \frac{\phi h_0}{h_{10000h}} \quad (5.7)$$

where h_0 is the initial height of the suspension in the tube and h_{10000} the height of the sediment layer after 10 000 h (after 600 h for the $\gamma - \text{Fe}_2\text{O}_3$), when the interface positions had stabilized. The sedimentation rates and the packing densities are tabulated in table 5.3.

Table 5.3: Sedimentation rates and particle packing densities

Specimen	Sedimentation rate ($\mu\text{m}/\text{s}$)	Packing density (-)
BASF HQ (SO)	0.0507	0.31
5% Nanofer Star (SO)	0.0340	0.28
10% Nanofer Star (SO)	0.0264	0.25
BASF HQ (IL)	0.1449	0.46
5% Nanofer Star (IL)	0.0580	0.39
10% Nanofer Star (IL)	0.0081	0.35
5% $\gamma - \text{Fe}_2\text{O}_31$ (SO)	0.0089	0.18 ⁽¹⁾
5% $\gamma - \text{Fe}_2\text{O}_32$ (SO)	0.0123	0.19 ⁽¹⁾

¹ after 600 hours

The effect of the viscosity of the carrier fluid on the sedimentation rate should be considered first since fluid's higher resistance to flow should cause slower particle settling. The Stokes' law can be used to determine the terminal velocity v_t of a single particle in a fluid as follows:

$$v_t = \frac{2g(\rho_p - \rho_f)r^2}{9\eta_f} \quad (5.8)$$

The equation can be used only for low particle concentrations where the hydrodynamic interactions by the nearby particles are neglected. Therefore, the sedimentation rate of the whole suspensions should be calculated by the semi-empirical Richardson and Zaki equation [96] in the following way:

$$v_s = v_t * (1 - \phi)^k \quad (5.9)$$

Here, k is an empirically determined exponent dependent on the Reynolds number that is the ratio of the inertial forces to the viscous forces. Here the Reynolds number is always $\ll 0.2$ and therefore, the exponent is 4.65 [96]. The sedimentation rates by the equation 5.9 are 0.1454 and 0.0226 $\mu\text{m}/\text{s}$ for the monodisperse SO and IL based fluids, respectively. The equation 5.9 corresponds quite well with measured the sedimentation behaviour of the monodisperse SO based fluid for the first 20 hours, as illustrated in figure 5.18a. Then the measured sedimentation slows down gradually. The deceleration might be caused by the formation of a large tube spanning network of loose particle agglomerates as the average interparticle distance decreases during settling and the effect of the attractive magnetostatic (due to small level remnant magnetization in the particles) and van der Waals forces becomes stronger. The agglomeration has been reported to slow down the settling during sedimentation measurements by friction of the particle structures with the tube walls [10, 35, 39].

The shape of the sedimentation curve for the monodisperse IL based fluid differs from the SO based fluid as seen from figure 5.18b. The sedimentation follows the equation 5.9 at the beginning of the measurement, but accelerates rapidly after about 20 h. It could be that the steric repulsion generated by the IL is not enough to prevent agglomeration when the particle distance decreases during settling, which would lead to formation of small agglomerates that settle faster than individual particles [38, 97]. The packing densities of both MR fluids are considerably lower than what is expected in free settling. The packing densities for SO and IL based fluids are 0.31 and 0.46, respectively, while the random close packing density for spherical particles is 0.64. This can also be associated with agglomeration that supports the conclusions made from the viscosity curves and sedimentation rates: the agglomerates in SO are larger and looser.

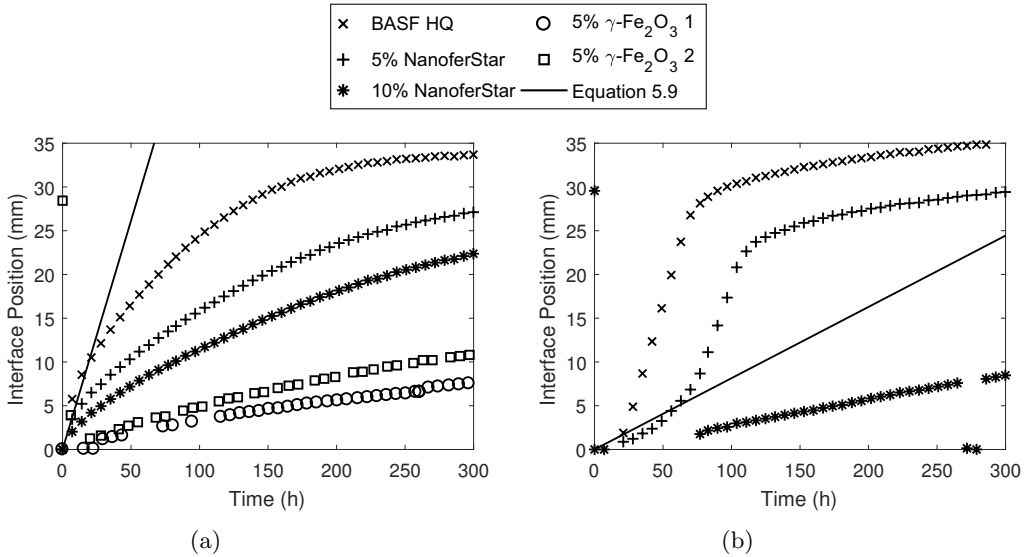


Figure 5.18: Sedimentation of particles in (a) SO and (b) IL. The solid lines represent the theoretically predicted values by equation 5.9.

The addition of nanoparticles reduces the sedimentation rate and the packing density with both carrier fluids. The effect is quite modest for the Nanofer Star particles in SO as 10% concentration about halves the sedimentation rate. Smaller nanoparticles reduce the sedimentation rate more efficiently; the rates for MR fluid with $\gamma - \text{Fe}_2\text{O}_3$ 1 and 2 particles were 0.0089 and 0.0123 $\mu\text{m/s}$, respectively, which are about 4.5 to 6 times slower than for the monodisperse fluid. The changes are more drastic for the IL based fluids as the 5% Nanofer Star concentration lengthens the initial slow sedimentation phase and 10% concentration keeps the sedimentation almost 20 times slower than for the monodisperse fluid over the whole measurement. However, it should be noted that the agglomeration of the particles in monodisperse fluids is now influencing on the interpretation of the results. Since the settling of the micron-sized particles is faster in IL and slower in SO than predicted theoretically, the relative improvement in sedimentation stability of the IL based fluids is higher. The situation is reversed, if the comparison is done to the theoretical predictions instead, which assume that all particles are completely dispersed in the carrier fluid. The changes in the shape of the sedimentation curves of the IL based fluids may be considered as an evidence that the nanoparticles are improving the dispersion stability. This is probably achieved by the nanoparticle halos that keep the micron-sized particles separated during settling, thus

reducing the effect of the relatively short distance magnetostatic and van der Waals attractions. Haloing will also lead to higher ϕ_{eff} that will reduce the packing density and slow the sedimentation as stated by the equation 5.9. It can be concluded that the nanoparticle concentration has to be high enough to surround the micron-sized particle completely by a halo with an appreciable thickness in order to achieve notable improvements in dispersion and sedimentation stabilities. The halo seems to become thicker when the number of nanoparticles grows by increase in concentration or decrease in size. Magnet et al. also reported thickening of the nanoparticle halo with increasing nanoparticle concentration [49]. The looser particle packing after the settling, which is likely induced by the nanoparticle halos as well, can be beneficial for the redispersibility since the attractive magnetostatic and van der Waals forces may lead to formation of tightly bound sediment that is difficult to disperse [50, 59, 98].

5.3.4 MR response of the bidisperse MR fluids

The impact of the carrier fluid, nanoparticle concentration and type on the MR response was estimated based on the dynamic yield stresses and oscillatory measurements.

5.3.4.1 Dynamic yield stress

The dynamic yield stresses were determined by fitting a Bingham model on the flow curves measured at magnetic flux densities ranging from 70 to 642 mT. The dynamic yield stresses as function of the magnetic flux density are illustrated in figures 5.19 - 5.21. The values are averages of two measurements and the standard errors are illustrated by the error bars. The effect of the carrier fluid and the particle dispersion is the most evident from figure 5.19 that illustrates dynamic yield stresses for the SO and IL based monodisperse MR fluids. The dynamic yield stress for the IL based fluid is 4-13% higher than for the SO based fluid, although the difference is within the standard error at higher flux densities. The increase is expected, since the well dispersed particles are able to form more ordered structures under magnetic field than particle agglomerates, which improves the magnetic interactions and leads to slightly higher dynamic yield stresses [12, 83].

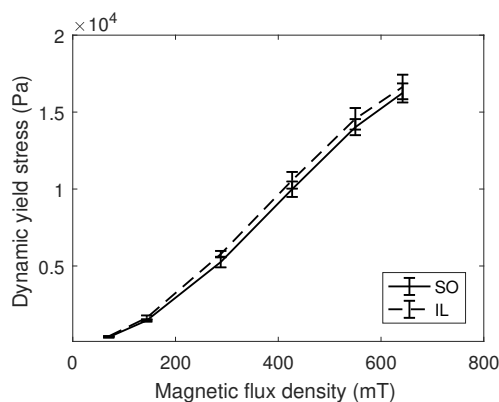


Figure 5.19: The dynamic yield stresses as function of the magnetic flux density for the SO (solid line) and IL based (broken line) monodisperse MR fluids.

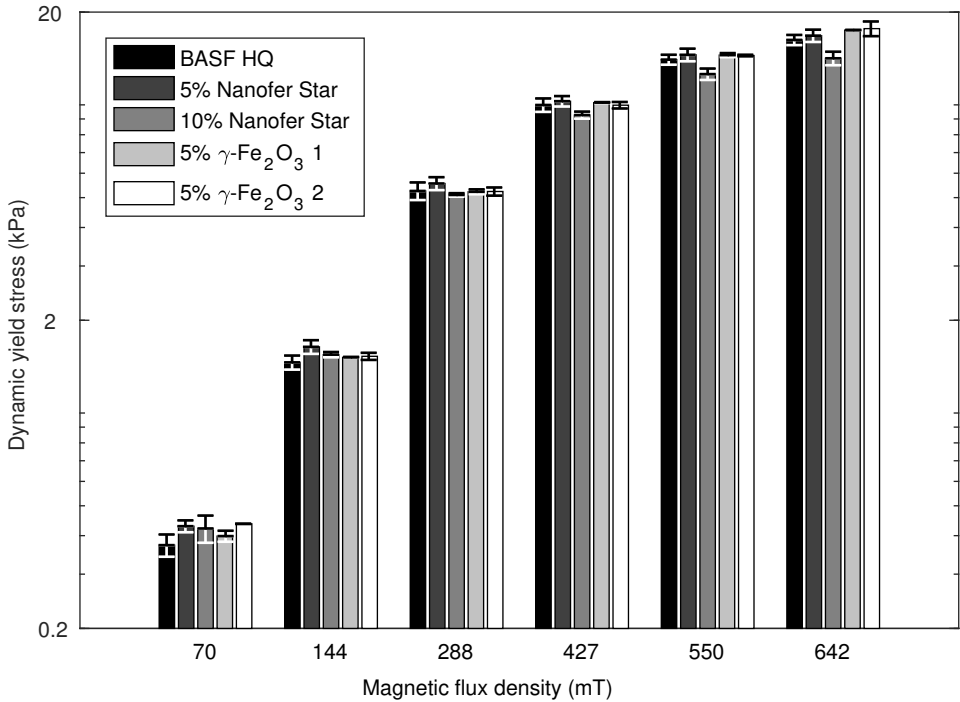


Figure 5.20: Dynamic yield stresses of SO based MR fluids.

The addition of nanoparticles had only a modest effect on the dynamic yield stress as illustrated in figures 5.20 and 5.21. The yield stresses of the SO based bidisperse MR fluids were slightly higher than for the monodisperse fluid at the lowest magnetic flux density (70 mT). This could be explained by higher initial permeability of the nanoparticles that is determined from the initial slope of the virgin magnetization curves in figure 5.15. The orientation of the magnetic moments parallel to the weak external magnetic field is easier for nanoparticles and therefore, stronger particles structures may be induced at low magnetic flux densities [14,99]. At higher flux densities the differences between bidisperse fluids with 5% of nanoparticles to the monodisperse fluid were generally within the standard error of the results. An increase in Nanofer Star concentration to 10% led to a reduction of the yield stress. With IL based bidisperse MR fluids both the addition of nanoparticles and the increase in the nanoparticle concentration decreased the yield stress. In previous studies on bidisperse MR fluids where part part of the micron-sized particles have been replaced by nanoparticles and the total particle fraction has kept constant, the addition of nanoparticles and an increase in the nanoparticle concentration has typically led to a decrease in the yield stress [47, 50, 94]. Increases in dynamic yield stress have also been reported at low nanoparticle concentrations, but a further increase in the concentration has eventually led to a decrease [17,18]. Interestingly, the magnetic properties of the nanoparticles do not seem to have a strong effect on the dynamic yield stress, but the fraction of the micron-sized particles is more important. The reduction of the yield stress as the concentration of the micron-sized particles decreases could partly be explained by the differences in magnetic properties of the nanoparticles and BASF HQ particles. The magnetic permeability is initially higher for

the nanoparticles, but decreases as the intensity of the external magnetic field is increased because of partial magnetic saturation of the nanoparticles. Since the nanoparticles have lower M_s than BASF HQ, also their magnetostatic interactions with each other and micron-sized particles are weaker at moderate and high magnetic fields, as expressed by the equations 2.4 and 2.5. The second explanation for the reduced dynamic yield stress could be the effect of the nanoparticle halos. It has been proposed that too thick nanoparticle halos around the larger particles could weaken the magnetic interactions [48, 50, 94]. This could explain why the improved dispersion of the particles in IL does not improve the yield stress of the bidisperse MR fluids.

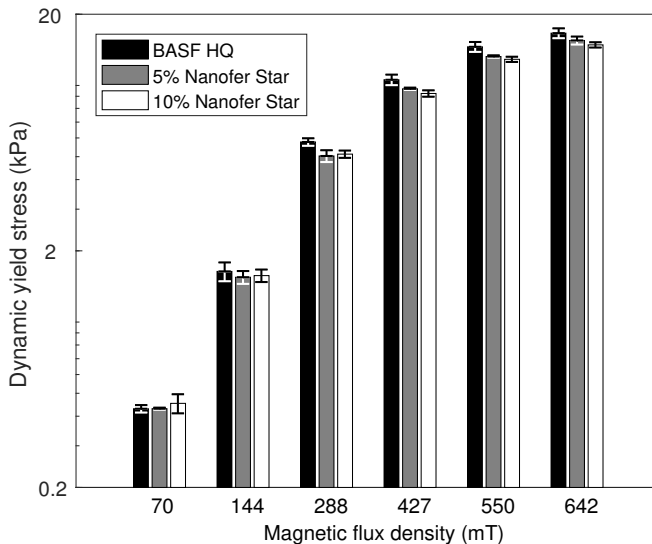


Figure 5.21: Dynamic yield stresses of IL based MR fluids.

5.3.4.2 Oscillatory measurements

The oscillatory measurements were done only for the monodisperse SO based fluid and bidisperse fluids with 5% of $\gamma - \text{Fe}_2\text{O}_3$ 1 and 2 nanoparticles. The amplitude sweeps at 70 and 427 mT magnetic flux densities are shown in figures 5.22 and 5.23. At 70 mT both storage G' and loss G'' moduli show a linear region at low strain amplitudes followed by a steady decrease. In the linear region the G' is higher than G'' indicating that the elastic deformation is dominating and the MR fluid behaves mainly in a solid like manner. The MR fluid deforms in the linear region by stretching and tilting of the particle structures. The linear region ends when the stress exceeds the yield stress and the particle structures begin to break. The viscous portion of deformation becomes stronger as more energy is dissipated and the behaviour of the MR fluid changes from solid to more liquid like. The addition of $\gamma - \text{Fe}_2\text{O}_3$ nanoparticles decreases both moduli, thus the particle structures become weaker. The effect is stronger for the $\gamma - \text{Fe}_2\text{O}_3$ 1 particles that have lower M_s . The weakening of the elastic response due to the nanoparticle addition is bit surprising, since the dynamic yield stresses of the same fluids show a slight increase. Similar observation was made by Wereley et al. earlier [17].

The increase of magnetic flux density to 427 mT raises the G' more than G'' , indicating a stronger elastic response due to greater magnetostatic attraction between the particles.

The linear region of the G' continues longer than G'' and reaches higher strain amplitudes than at 70 mT. The increase in magnetic flux density induces new type of behaviour for the G'' , as it first passes through a distinct maximum before a gradual decrease. The peaking of the G'' is called strain overshooting and it is caused by simultaneous breaking and reformation of the particle structures as discussed in section 5.1. Eventually the G'' begins to decrease as the formation of the new structures becomes increasingly difficult at higher shear amplitudes and the structures break into smaller clusters or individual particles [86]. The viscous portion of the deformation increases at expense of the elastic portion when the micron-sized particles are being replaced by $\gamma - \text{Fe}_2\text{O}_3$ particles. In other words the deformation of bidisperse MR fluids dissipates more energy than monodisperse fluid and less is stored into elastic deformation of the particle structures. Also the peaking of the G'' is weaker than for the monodisperse fluid, which could mean that the reformation of the particle structures is hindered by the nanoparticles.

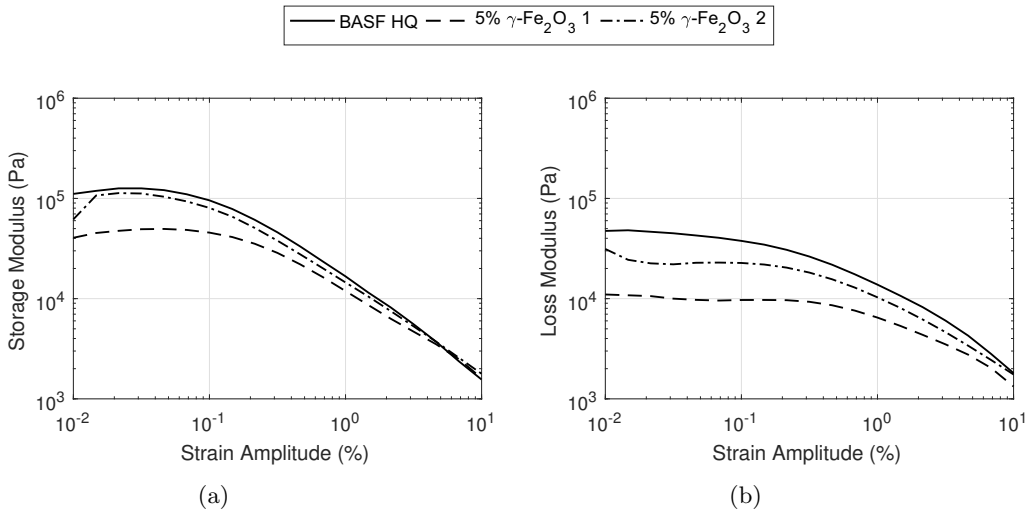


Figure 5.22: (a) Storage and (b) loss moduli for MR fluids at 70 mT magnetic flux density

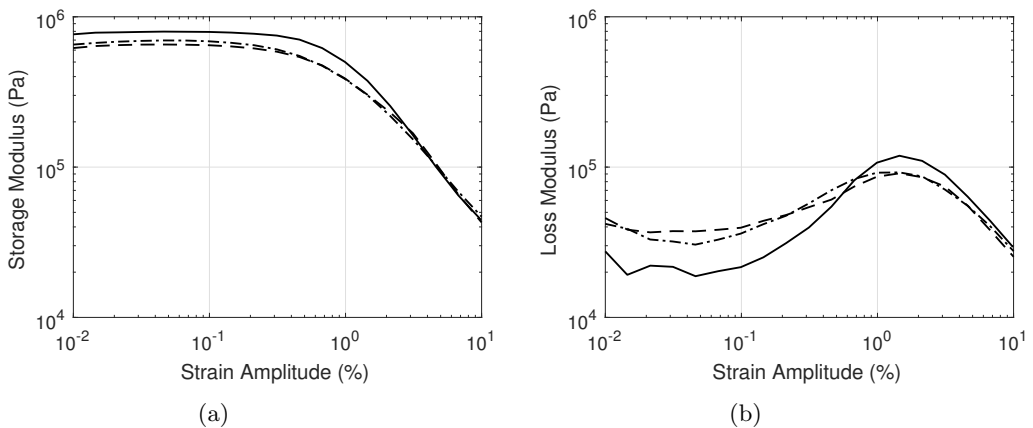


Figure 5.23: (a) Storage and (b) loss moduli for MR fluids at 427 mT magnetic flux density

6 Conclusions

The characterization of the field dependent yield stress is essential for the development of the MR technology. The aim of this thesis was to examine how the measuring procedure and system is affecting the results and to point out some important issues related to the measuring events. The outcomes were utilized in later pursue to study how the properties of bidisperse MR fluid are effected by its composition.

The measured static and dynamic yield stresses increased as the friction between the MR fluid and measuring plates was enhanced by roughening the plate surfaces or by applying magnetic surface materials. This was likely originated from elimination or reduction of the wall slip that was present with non-magnetic plates having lower surface roughness than the particle size. The effect was stronger for the dynamic yield stress and it was supposed to be caused by the differences in the slippage mechanisms. When wall slip is present in the measurements, an increase in the measuring gap height is expected to raise the measured yield stresses. However, the yield stresses proved to increase even when the wall slip was eliminated by roughened or magnetic plates. This was believed to be caused by increase of the magnetic flux density in the measuring gap, which was observed by simulations and measurements.

The results show that the existence of wall slip may lead to systematic underestimation of the yield stress especially as the magneto-cell is originally provided only with a smooth non-magnetic geometry. Furthermore, the wall slip may remain undetected as the measured shear stresses act in an unexpected manner when the gap height is raised.

In addition to eliminating the wall slip, the magnetic plates were found to provide more uniform magnetic flux density profile in the measuring gap. This reduces the probability of transient changes during measurement as the particles tend to migrate towards higher magnetic flux density intensities.

A better dispersion of the micron-sized carbonyl iron particles was reached in IL than in SO. However, the results of the sedimentation measurements suggested that some agglomeration may still happen under long term storage as the particle distance decreases during settling and the steric repulsion between the particles generated by the IL is not strong enough to counteract magnetostatic and van der Waals attractions. The dispersion and sedimentation stabilities improve significantly as the particle size distribution is turned to bidisperse by replacing part of the micron-sized particles with nanoparticles. This was believed to be caused by a combined effect the IL and halving of the nanoparticles around the larger particles. The nanoparticle fraction has to be high enough to provide a halo with an appropriate thickness. The fraction depends at least on the particle sizes.

The decrease of the nanoparticle size leads to both positive and negative effects on the properties of bidisperse MR fluids. On a positive side the sedimentation stability seems to improve with decreasing particle size. This may be caused by higher surface area per volume ratio that leads to higher resistance as the particles move in the carrier fluid or by formation of thicker nanoparticle halos around the larger particles as the number of the

particles increases. On a negative side the phenomenon also causes higher field independent viscosity that leads to weaker relative change in the rheological properties as the external magnetic field is applied. However, the same problem arises with thixotropic agents that are commonly used to improve the sedimentation stability of MR fluids and in addition they can weaken the MR effect and make the redispersion of particles more difficult.

The properties of the LFS synthesized $\gamma - \text{Fe}_2\text{O}_3$ nanoparticles were comparable to ones prepared by chemical co-precipitation. The method provides an interesting alternative for particle production especially as it is considered optional for up-scaling. The LFS process is also versatile as it can be used to create a broad spectrum metal and metal oxide nanoparticles, which may be one- or multi-component.

6.1 Suggestions for the future work

The results presented in this thesis show that a slight modification of composition of bidisperse MR fluids may cause significant changes in its properties. The modifications were not thoroughly examined and further work is still needed. Since the IL seems to be a potential carrier fluid for the bidisperse fluids, it should be tested with other nanoparticles having different compositions, sizes and concentrations to fully understand how the improved dispersion and sedimentation stability is reached. Also as the LFS process seems as a promising way to prepare nanoparticles for the bidisperse MR fluids, its capabilities should be studied further. The options for using new materials to prepare the particles as well particles having multi-component structures are intriguing and might help to solve the wear and sedimentation issues.

Bibliography

- [1] M Schwartz. *Smart materials*. CRC Press, 2008.
- [2] DJ Carlson and MR Jolly. Mr fluid, foam and elastomer devices. *Mechatronics*, 10(4):555–569, 2000.
- [3] DJ Carlson. Magnetorheological fluids. In Mel Schwartz, editor, *Smart materials*, chapter 17. CRC Press, 2008.
- [4] J Rabinow. The magnetic fluid clutch. *Electrical Engineering*, 67(12):1167–1167, 1948.
- [5] MR Jolly, JW Bender, and JD Carlson. Properties and applications of commercial magnetorheological fluids. *Journal of intelligent material systems and structures*, 10(1):5–13, 1999.
- [6] DJ Klingenberg. Magnetorheology: Applications and challenges. *AIChE Journal*, 47(2):246–249, 2001.
- [7] M Kciuk and R Turczyn. Properties and application of magnetorheological fluids. *Journal of Achievements in Materials and Manufacturing Engineering*, 18(1-2):127–130, 2006.
- [8] I Bica, YD Liu, and HJ Choi. Physical characteristics of magnetorheological suspensions and their applications. *Journal of Industrial and Engineering Chemistry*, 19(2):394–406, 2013.
- [9] C Fei, T Zuzhi, and W Xiangfan. Novel process to prepare high-performance magnetorheological fluid based on surfactants compounding. *Materials and Manufacturing Processes*, 30(2):210–215, 2015.
- [10] J Yang, H Yan, Z Hu, and D Ding. Viscosity and sedimentation behaviors of the magnetorheological suspensions with oleic acid/dimer acid as surfactants. *Journal of Magnetism and Magnetic Materials*, 417:214–221, 2016.
- [11] MT López-López, A Zugaldia, F González-Caballero, and JDG Durán. Sedimentation and redispersion phenomena in iron-based magnetorheological fluids. *Journal of Rheology*, 50(4):543–560, 2006.
- [12] MT López-López, A Zugaldia, A Gómez-Ramirez, F González-Caballero, and JDG Durán. Effect of particle aggregation on the magnetic and magnetorheological properties of magnetic suspensions. *Journal of Rheology*, 52(4):901–912, 2008.
- [13] R Patel. Mechanism of chain formation in nanofluid based mr fluids. *Journal of Magnetism and Magnetic Materials*, 323(10):1360–1363, 2011.
- [14] JL Viota, JDG Durán, F Gonzalez-Caballero, and AV Delgado. Magnetic properties of extremely bimodal magnetite suspensions. *Journal of magnetism and magnetic materials*, 314(2):80–86, 2007.

- [15] D Susan-Resiga and L Vékás. Yield stress and flow behavior of concentrated ferrofluid-based magnetorheological fluids: the influence of composition. *Rheologica Acta*, 53(8):645–653, 2014.
- [16] MT López-López, P Kuzhir, S Laciş, G Bossis, F González-Caballero, and JDG Durán. Magnetorheology for suspensions of solid particles dispersed in ferrofluids. *Journal of Physics: Condensed Matter*, 18(38):S2803, 2006.
- [17] NM Wereley, A Chaudhuri, J-H Yoo, S John, S Kotha, A Suggs, R Radhakrishnan, BJ Love, and TS Sudarshan. Bidisperse magnetorheological fluids using fe particles at nanometer and micron scale. *Journal of Intelligent Material Systems and Structures*, 17(5):393–401, 2006.
- [18] A Chaudhuri, G Wang, NM Wereley, V Tasovksi, and R Radhakrishnan. Substitution of micron by nanometer scale powders in magnetorheological fluids. *International Journal of Modern Physics B*, 19(07n09):1374–1380, 2005.
- [19] J de Vicente, DJ Klingenberg, and R Hidalgo-Alvarez. Magnetorheological fluids: a review. *Soft Matter*, 7(8):3701–3710, 2011.
- [20] HM Laun, G Schmidt, C Gabriel, and C Kieburg. Reliable plate–plate mrf magnetorheometry based on validated radial magnetic flux density profile simulations. *Rheologica acta*, 47(9):1049–1059, 2008.
- [21] E Lemaire and G Bossis. Yield stress and wall effects in magnetic colloidal suspensions. *Journal of Physics D: Applied Physics*, 24(8):1473, 1991.
- [22] HM Laun, C Gabriel, and C Kieburg. Wall material and roughness effects on transmittable shear stresses of magnetorheological fluids in plate–plate magnetorheometry. *Rheologica acta*, 50(2):141–157, 2011.
- [23] A Aharoni. *Introduction to the theory of ferromagnetism*. Oxford science publications, 2000.
- [24] CJ Serna and MP Morales. Maghemite ($\gamma\text{-Fe}_2\text{O}_3$): A versatile magnetic colloidal material. In *Surface and colloid science*, pages 27–81. Springer, 2004.
- [25] HK Kammler, L Mädler, and SE Pratsinis. Flame synthesis of nanoparticles. *Chemical engineering & technology*, 24(6):583–596, 2001.
- [26] X Batlle and AI Labarta. Finite-size effects in fine particles: magnetic and transport properties. *Journal of Physics D: Applied Physics*, 35(6):R15–R42, 2002.
- [27] YW Jun, JWk Seo, and J Cheon. Nanoscaling laws of magnetic nanoparticles and their applicabilities in biomedical sciences. *Accounts of chemical research*, 41(2):179–189, 2008.
- [28] C Kittel. Theory of the structure of ferromagnetic domains in films and small particles. *Physical Review*, 70(11-12):965, 1946.
- [29] JS Lee, JM Cha, HY Yoon, J-K Lee, and YK Kim. Magnetic multi-granule nanoclusters: A model system that exhibits universal size effect of magnetic coercivity. *Scientific reports*, 5:12135, 2015.

- [30] L Vékás. Ferrofluids and magnetorheological fluids. In *Advances in science and technology*, volume 54, pages 127–136. Trans Tech Publ, 2008.
- [31] L Vekas, D Bica, and MV Avdeev. Magnetic nanoparticles and concentrated magnetic nanofluids: synthesis, properties and some applications. *China Particuology*, 5(1-2):43–49, 2007.
- [32] KN Marsh, JA Boxall, and R Lichtenthaler. Room temperature ionic liquids and their mixtures—a review. *Fluid Phase Equilibria*, 219(1):93–98, 2004.
- [33] C Guerrero-Sanchez, T Lara-Ceniceros, E Jimenez-Regalado, M Raşa, and US Schubert. Magnetorheological fluids based on ionic liquids. *Advanced Materials*, 19(13):1740–1747, 2007.
- [34] FCC Oliveira, LM Rossi, RF Jardim, and JC Rubim. Magnetic fluids based on γ -Fe₂O₃ and CoFe₂O₄ nanoparticles dispersed in ionic liquids. *The Journal of Physical Chemistry C*, 113(20):8566–8572, 2009.
- [35] A Gómez-Ramírez, MT López-López, F González-Caballero, and JDG Durán. Stability of magnetorheological fluids in ionic liquids. *Smart Materials and Structures*, 20(4):045001, 2011.
- [36] M Ashtiani, SH Hashemabadi, and A Ghaffari. A review on the magnetorheological fluid preparation and stabilization. *Journal of Magnetism and Magnetic Materials*, 374:716–730, 2015.
- [37] VR Iyengar, SM Yurgelevic, and RT Foister. Magnetorheological fluid with a fluorocarbon thickener, June 8 2010. US Patent 7,731,863.
- [38] MT López-López, J De Vicente, F González-Caballero, and JDG Durán. Stability of magnetizable colloidal suspensions by addition of oleic acid and silica nanoparticles. *Colloids and Surfaces A: Physicochemical and Engineering Aspects*, 264(1):75–81, 2005.
- [39] MT López-López, J De Vicente, G Bossis, F González-Caballero, and JDG Durán. Preparation of stable magnetorheological fluids based on extremely bimodal iron–magnetite suspensions. *Journal of materials research*, 20(4):874–881, 2005.
- [40] DS Jang, YD Liu, JH Kim, and HJ Choi. Enhanced magnetorheology of soft magnetic carbonyl iron suspension with hard magnetic γ -Fe₂O₃ nanoparticle additive. *Colloid and Polymer Science*, 293(2):641–647, 2015.
- [41] HA Barnes and K Walters. The yield stress myth? *Rheologica Acta*, 24(4):323–326, 1985.
- [42] HA Barnes. The yield stress—a review or -everything flows? *Journal of Non-Newtonian Fluid Mechanics*, 81(1-2):133–178, 1999.
- [43] HM Laun, C Gabriel, and Ch Kieburg. Magnetorheological fluid in oscillatory shear and parameterization with regard to MR device properties. *Journal of Intelligent Material Systems and Structures*, 2009.
- [44] H See. Mechanisms of magneto-and electro-rheology: Recent progress and unresolved issues. *Applied rheology*, pages 70–82, 2001.

- [45] G Bossis, S Lacis, A Meunier, and O Volkova. Magnetorheological fluids. *Journal of magnetism and magnetic materials*, 252:224–228, 2002.
- [46] G Bossis, O Volkova, S Lacis, and A Meunier. Magnetorheology: fluids, structures and rheology. In *Ferrofluids*, pages 202–230. Springer, 2002.
- [47] GT Ngatu and NM Wereley. Viscometric and sedimentation characterization of bidisperse magnetorheological fluids. *IEEE Transactions on Magnetics*, 43(6):2474–2476, 2007.
- [48] MT López-López, AY Zubarev, and G Bossis. Repulsive force between two attractive dipoles, mediated by nanoparticles inside a ferrofluid. *Soft Matter*, 6(18):4346–4349, 2010.
- [49] C Magnet, P Kuzhir, G Bossis, A Meunier, L Suloeva, and A Zubarev. Haloing in bimodal magnetic colloids: The role of field-induced phase separation. *Physical Review E*, 86(1):011404, 2012.
- [50] GR Iglesias, MT López-López, JDG Duran, F González-Caballero, and AV Delgado. Dynamic characterization of extremely bidisperse magnetorheological fluids. *Journal of colloid and interface science*, 377(1):153–159, 2012.
- [51] SG Sherman, AC Becnel, and NM Wereley. Relating mason number to bingham number in magnetorheological fluids. *Journal of Magnetism and Magnetic Materials*, 380:98–104, 2015.
- [52] J Mewis and NJ Wagner. *Colloidal Suspension Rheology*. Cambridge University Press, 2012.
- [53] S Mueller, EW Llewellyn, and HM Mader. The rheology of suspensions of solid particles. In *Proceedings of the Royal Society of London A: Mathematical, Physical and Engineering Sciences*, volume 466, pages 1201–1228. The Royal Society, 2010.
- [54] IM Krieger and TJ Dougherty. A mechanism for non-newtonian flow in suspensions of rigid spheres. *Transactions of the Society of Rheology*, 3(1):137–152, 1959.
- [55] MD Rintoul and S Torquato. Computer simulations of dense hard-sphere systems. *The Journal of chemical physics*, 105(20):9258–9265, 1996.
- [56] AJF Bombard, M Knobel, MR Alcantara, and I Joeques. Evaluation of magnetorheological suspensions based on carbonyl iron powders. *Journal of intelligent material systems and structures*, 13(7-8):471–478, 2002.
- [57] F Qi and RI Tanner. Relative viscosity of bimodal suspensions. *Korea-Australia Rheology Journal*, 23(2):105–111, 2011.
- [58] SG Ward and RL Whitmore. Studies of the viscosity and sedimentation of suspensions Part 1.-The viscosity of suspension of spherical particles. *British Journal of Applied Physics*, 1(11):286, 1950.
- [59] PP Phulé, MP Mihalcin, and S Genc. The role of the dispersed-phase remnant magnetization on the redispersibility of magnetorheological fluids. *Journal of materials research*, 14(7):3037–3041, 1999.

- [60] L Rodríguez-Arco, MT López-López, F González-Caballero, and JDG Durán. Steric repulsion as a way to achieve the required stability for the preparation of ionic liquid-based ferrofluids. *Journal of colloid and interface science*, 357(1):252–254, 2011.
- [61] CW Macosko and RG Larson. *Rheology: principles, measurements, and applications*. VCH New York, 1994.
- [62] QD Nguyen and DV Boger. Measuring the flow properties of yield stress fluids. *Annual Review of Fluid Mechanics*, 24(1):47–88, 1992.
- [63] C Tiu, J Guo, and PHT Uhlherr. Yielding behaviour of viscoplastic materials. *Journal of Industrial and Engineering Chemistry*, 12(5):653–662, 2006.
- [64] A Sun and S Gunasekaran. Yield stress in foods: measurements and applications. *International Journal of Food Properties*, 12(1):70–101, 2009.
- [65] YL Yeow, Y-K Leong, and A Khan. Error introduced by a popular method of processing parallel-disk viscometry data. *Applied Rheology*, 17(6):66415–66493, 2007.
- [66] QD Nguyen, T Akroyd, DC De Kee, and L Zhu. Yield stress measurements in suspensions: an inter-laboratory study. *Korea-Australia Rheology Journal*, 18(1):15–24, 2006.
- [67] JC Ulicny and MA Golden. Evaluation of yield stress measurement techniques on a parallel plate magnetic rheometer. *International Journal of Modern Physics B*, 21(28n29):4898–4906, 2007.
- [68] S Genc and PP Phulé. Rheological properties of magnetorheological fluids. *Smart Materials and Structures*, 11(1):140, 2002.
- [69] S Mantripragada, X Wang, F Gordaninejad, B Hu, and A Fuchs. Characterization of rheological properties of novel magnetorheological fluids. In *Proceedings of the 10th International Conference on Electrorheological Fluids and Magnetorheological Suspensions: Lake Tahoe, USA, 18-22 June, 2006*, page 180. World Scientific Publishing Company Incorporated, 2007.
- [70] W Kordonski, S Gorodkin, and N Zhuravski. Static yield stress in magnetorheological fluid. *International journal of modern physics B*, 15(06n07):1078–1084, 2001.
- [71] G Bossis, P Khuzir, S Lacis, and O Volkova. Yield behavior of magnetorheological suspensions. *Journal of Magnetism and Magnetic Materials*, 258:456–458, 2003.
- [72] Y Yang, L Li, and G Chen. Static yield stress of ferrofluid-based magnetorheological fluids. *Rheologica acta*, 48(4):457–466, 2009.
- [73] MT López-López, P Kuzhir, J Caballero-Hernández, L Rodríguez-Arco, JDG Durán, and G Bossis. Yield stress in magnetorheological suspensions near the limit of maximum-packing fraction. *Journal of rheology*, 56(5):1209, 2012.
- [74] M Keentok and H See. Behaviour of field-responsive suspensions under oscillatory shear flow. *Korea-Australia Rheology Journal*, 19(3):117–123, 2007.
- [75] I Masalova, AY Malkin, and R Foudazi. Yield stress of emulsions and suspensions as measured in steady shearing and in oscillations. *Applied Rheology*, 18(4), 2008.

- [76] RP Chhabra and JF Richardson. *Non-Newtonian flow and applied rheology: engineering applications*. Butterworth-Heinemann, 2011.
- [77] HA Barnes. A review of the slip (wall depletion) of polymer solutions, emulsions and particle suspensions in viscometers: its cause, character, and cure. *Journal of Non-Newtonian Fluid Mechanics*, 56(3):221–251, 1995.
- [78] MT López-López, L Rodríguez-Arco, A Zubarev, L Iskakova, and JDG Durán. Effect of gap thickness on the viscoelasticity of magnetorheological fluids. *Journal of Applied Physics*, 108(8):083503, 2010.
- [79] A Yoshimura and RK Prud’homme. Wall slip corrections for couette and parallel disk viscometers. *Journal of Rheology*, 32(1):53–67, 1988.
- [80] J de Vicente, MT López-López, JDG Durán, and F González-Caballero. Shear flow behavior of confined magnetorheological fluids at low magnetic field strengths. *Rheologica acta*, 44(1):94–103, 2004.
- [81] A Gómez-Ramírez, MT López-López, F González-Caballero, and JDG Durán. Wall slip phenomena in concentrated ionic liquid-based magnetorheological fluids. *Rheologica acta*, 51(9):793–803, 2012.
- [82] J Caballero-Hernandez, A Gomez-Ramirez, JDG Duran, F Gonzalez-Caballero, A Zubarev, and MT Lopez-Lopez. On the effect of wall slip on the determination of the yield stress of magnetorheological fluids. *Applied Rheology*, 27(1), 2017.
- [83] MT López-López, P Kuzhir, G Bossis, and P Mingalyov. Preparation of well-dispersed magnetorheological fluids and effect of dispersion on their magnetorheological properties. *Rheologica Acta*, 47(7):787–796, 2008.
- [84] WH Li, H Du, G Chen, SH Yeo, and N Guo. Nonlinear viscoelastic properties of MR fluids under large-amplitude-oscillatory-shear. *Rheologica Acta*, 42(3):280–286, 2003.
- [85] WH Li, H Du, and NQ Guo. Dynamic behavior of MR suspensions at moderate flux densities. *Materials Science and Engineering: A*, 371(1):9–15, 2004.
- [86] HG Sim, KH Ahn, and SJ Lee. Three-dimensional dynamics simulation of electrorheological fluids under large amplitude oscillatory shear flow. *Journal of Rheology*, 47(4):879–895, 2003.
- [87] M-C Yang, LE Scriven, and CW Macosko. Some rheological measurements on magnetic iron oxide suspensions in silicone oil. *Journal of Rheology*, 30(5):1015–1029, 1986.
- [88] HJ Walls, SB Caines, AM Sanchez, and SA Khan. Yield stress and wall slip phenomena in colloidal silica gels. *Journal of Rheology*, 47(4):847–868, 2003.
- [89] JC Ulicny, MA Golden, CS Namuduri, and DJ Klingenberg. Transient response of magnetorheological fluids: Shear flow between concentric cylinders. *Journal of Rheology*, 49(1):87–104, 2005.
- [90] H See and R Tanner. Shear rate dependence of the normal force of a magnetorheological suspension. *Rheologica acta*, 42(1-2):166–170, 2003.
- [91] J De Vicente, F González-Caballero, G Bossis, and O Volkova. Normal force study in concentrated carbonyl iron magnetorheological suspensions. *Journal of Rheology*, 46(5):1295–1303, 2002.

- [92] I Nurdin, MR Johan, II Yaacob, BC Ang, and A Andriyana. Synthesis, characterisation and stability of superparamagnetic maghemite nanoparticle suspension. *Materials Research Innovations*, 18(sup6):S6–200, 2014.
- [93] N Rosenfeld, NM Wereley, R Radakrishnan, and TS Sudarshan. Behavior of magnetorheological fluids utilizing nanopowder iron. *International Journal of Modern Physics B*, 16(17n18):2392–2398, 2002.
- [94] JL Viota, JDG Durán, and AV Delgado. Study of the magnetorheology of aqueous suspensions of extremely bimodal magnetite particles. *The European Physical Journal E*, 29(1):87–94, 2009.
- [95] D Susan-Resiga and L Vékás. Ferrofluid-based magnetorheological fluids: tuning the properties by varying the composition at two hierarchical levels. *Rheologica Acta*, 55(7):581–595, 2016.
- [96] JF Richardson and WN Zaki. The sedimentation of a suspension of uniform spheres under conditions of viscous flow. *Chemical Engineering Science*, 3(2):65–73, 1954.
- [97] J De Vicente, AV Delgado, RC Plaza, JDG Durán, and F González-Caballero. Stability of cobalt ferrite colloidal particles. effect of pH and applied magnetic fields. *Langmuir*, 16(21):7954–7961, 2000.
- [98] M Aguilera Portillo and GR Iglesias. Magnetic nanoparticles as a redispersing additive in magnetorheological fluid. *Journal of Nanomaterials*, 2017, 2017.
- [99] C Kormann, HM Laun, and HJ Richter. MR fluids with nano-sized magnetic particles. *International Journal of Modern Physics B*, 10(23n24):3167–3172, 1996.

Appendix: Original publications

Publication I

Ilari Jönkkäri and Seppo Syrjälä

Evaluation of techniques for measuring the yield stress of a magnetorheological fluid

Applied Rheology 20 (2010) 45875-45882

© 2010 Kerschensteiner Verlag GmbH
Reprinted with permission

EVALUATION OF TECHNIQUES FOR MEASURING THE YIELD STRESS OF A MAGNETORHEOLOGICAL FLUID

ILARI JÖNKKÄRI AND SEPPO SYRJÄLÄ

Department of Materials Science, Tampere University of Technology, P.O. 589,
33101 Tampere, Finland

* Email: ilari.jonkkari@tut.fi

Fax: +358.83.31152765

Received: 18.12.2009, Final version: 12.4.2010

ABSTRACT:

The yield stress of a magnetorheological fluid was measured as a function of magnetic flux density using different techniques. The yield stress values were determined by extrapolating the experimental shear stress-shear rate data to zero shear rate with the help of Bingham and Herschel-Bulkley models, and by using stress ramp and dynamic oscillatory tests. To obtain the rheological data, the rotational rheometer equipped with a magnetic field generator and a plate-and-plate measuring geometry was used. The different methods produced yield stress values which were in reasonable agreement with each other.

ZUSAMMENFASSUNG:

Die Fließgrenze einer magnetorheologischen Flüssigkeit wurde als Funktion der magnetischen Flussdichte mittels verschiedener Techniken gemessen. Die Werte der Fließgrenze wurden aus einer Extrapolation der experimentellen Schubspannungs- und Scherraten auf den Nullpunkt der Scherrate bestimmt. Für die Extrapolation wurden die Modelle nach Bingham und Herschel-Bulkley angewendet. Weiterhin wurden Messungen mit einer Spannungsrampe und dynamisch oszillatorische Tests durchgeführt. Um die rheologischen Daten messen zu können, wurde ein Rotationsrheometer mit einem Magnetfeldgenerator und einem Platte-Platte-Messsystem eingesetzt. Die unterschiedlichen Methoden liefern Werte für die Fließgrenze, die untereinander vergleichbar sind.

RÉSUMÉ:

La contrainte seuil d'un fluide magnétorhéologique a été mesurée en fonction de la densité de flux magnétique en utilisant différentes techniques. Les valeurs de contrainte seuil ont été mesurées en extrapolant les données contrainte de cisaillement-vitesse de cisaillement jusqu'à une vitesse nulle, à l'aide des modèles de Bingham et de Herschel-Bulkley, et en utilisant des rampes de contrainte ainsi que des tests dynamiques en oscillation. Afin d'obtenir les données rhéologiques, on a utilisé le rhéomètre rotationnel équipé d'un générateur de champ magnétique et d'une géométrie plan-plan. Les différentes méthodes produisent des valeurs de contrainte seuil qui sont en harmonie les unes avec les autres.

KEY WORDS: magnetorheological fluid, yield stress, rotational rheometer

1 INTRODUCTION

Magnetorheological (MR) fluids are suspensions of magnetizable particles in a carrier liquid such as mineral, silicone or synthetic oil. When exposed to an external magnetic field these materials show sudden, significant and reversible rheological property changes. Upon the application of a magnetic field the suspended particles interact with each other and aggregate into chain-like structures aligned in the field direction, which gives rise to an increase in the suspension viscosity and the appearance of a yield stress. The yield stress, which indicates the

threshold stress to break down the structure and initiate flow, is one of the key properties of the MR fluid. With increasing magnetic flux density, the yield stress of the fluid increases until the saturation magnetization of the particles is reached. Detailed discussions on the mechanisms, rheology and potential applications of MR fluids are available in recent review articles [1–3].

Although the existence of a true yield stress in fluids has been questioned [4, 5], it is generally recognized that a variety of fluids exhibit a limiting stress below which appreciable flow does not occur. A number of techniques have been

devised for measuring the yield stress directly or indirectly; reviews of these techniques have been presented by various authors (e.g. [6–8]). A widely used indirect procedure is based simply on extrapolating the experimental flow curve, i.e., the steady shear stress versus shear rate data, to zero shear rate and taking the shear stress intercept as the yield value. Most conveniently the extrapolation can be carried out by fitting one of the viscoplastic flow models to the relevant experimental data. Direct measurement of the yield stress relies on an independent assessment of the stress at which the material starts to flow. Creep, stress ramp and stress growth tests are among the techniques that have been used to directly determine the yield stress. The yield values determined by direct and indirect means are sometimes referred to as the static and dynamic yield stresses, respectively. An alternative way of evaluating the yield stress is to conduct dynamic oscillatory experiments as a function of increasing strain/stress amplitude. From these experiments, the stress recorded at the crossover point of the storage and loss moduli has been used as one estimate of the yield stress, but there are other possibilities as well. As evident on the basis of a recent inter-laboratory collaborative study reported by Nguyen et al. [9], markedly different values of yield stress of the same material may be obtained with different techniques and/or instruments. In general, direct methods were found to produce more reliable and reproducible results than indirect methods.

For MR fluids, the values of the yield stress have mostly been determined indirectly from the extrapolation of steady shear stress versus shear rate data using the Bingham model (see e.g. [10–13]). For obtaining the shear stress as a function of shear rate, a customary approach is to use the rotational rheometer equipped with an appropriate magnetic field generator and a plate-and-plate measuring geometry. This geometry offers many advantages, but suffers from a drawback in that the flow field is inhomogeneous, that is, the shear rate and shear stress within the sample vary with radial position. As a consequence, the determination of the true shear stress versus shear rate from the plate-and-plate experiment requires numerical differentiation of the raw data. This is typically not provided by the rheometer software, but the pertinent correction needs to be made separately. It appears that in many reported mea-

surements for MR fluids this correction has been ignored and only the apparent data have been presented. For fluids exhibiting yield stress this may lead to the overestimation of the shear stress by 25 %, as discussed by Yeow et al. [14]. The consequent error in the extrapolated yield stress may be even larger.

A number of studies have reported on the direct measurement of the yield stress of MR fluids [15–18]. In all of these contributions, the rotational rheometer with a plate-and-plate configuration was employed. The stress ramp technique was used by Kordonski et al. [15] and Bombard et al. [16]; the obtained yield stress values were lower than those produced by the indirect extrapolation method. Ulicny et al. [17] employed the stress ramp and stress growth techniques as well as the indirect extrapolation method based on the Bingham model. In addition to using the plate-and-plate measuring system for all of these test types, the stress growth experiment was also conducted with the concentric cylinder geometry. The results showed that the stress ramp method gives the lowest yield stress values and also leads to the highest scatter of measured data. The extrapolation method showed the lowest scatter and produced the yield stress values that were in accord with those obtained by the stress growth test with the concentric cylinder geometry; these two test methods were favoured by the authors as the most reliable. Yang et al. [18] compared the yield stresses measured by three different direct testing methods, namely the stress growth, strain ramp and stress ramp techniques. The yield stresses measured with the strain ramp and stress ramp methods were quite close to each other while the stress growth method gave significantly higher values.

A creep/recovery experiment has been attempted for MR fluids by Li et al. [19]. It was shown that this type of test can be used to deduce the yield stress of the MR fluid. Yet, this is a very time-consuming approach for determining the yield stress because a series of experiments at successively higher shear stresses needs to be accomplished. Shear oscillatory measurements have also been carried out for MR fluids [20, 21]. If the results of the amplitude sweep are plotted against the stress amplitude, both the storage and loss moduli exhibit a rapid decrease at a value corresponding closely to the yield stress, as noted by Laun et al. [21].

In this study, the yield stress of a commercial MR fluid as a function of magnetic flux density was experimentally determined with several methods. The yield stress values were obtained by means of steady shear, stress ramp and dynamic oscillatory tests. To extrapolate the shear stress versus shear rate data to zero rate, Bingham and Herschel-Bulkley models were used. In dynamic measurements the maximum of the elastic stress was used as an estimate of the yield stress.

2 EXPERIMENTAL

All the measurements were carried out using Anton Paar Physica MCR301 rotational rheometer equipped with an MRD180/1T magneto-cell; see Lauger et al. [22]. The rheometer is basically stress-controlled but also permits a rate-controlled mode of operation. The plate-and-plate measuring geometry (made of non-magnetic metal) with a plate diameter of 20 mm and a gap height of 1 mm was employed throughout. The supply of the electric current to the cell coil generates a magnetic field that passes through the tested fluid between the measuring plates. The maximum input current is 5 A which results in a magnetic flux density of around 1 T. A Hall probe was used to relate the input current to the magnetic flux density within the gap containing the fluid. The fluid temperature in all experiments was maintained at 30°C using a Haake DC30-K10 circulator bath. It is worth mentioning that the magneto-cell used here includes modifications suggested by Laun et al. [23]. As a result of the modifications, the radial magnetic flux density profile in the sample is much more uniform than in the manufacturer's original design.

The MR sample used for measurements was MRF-132DG from Lord Corp., which is a suspension of 32 vol-% micron-sized carbonyl iron particles in hydrocarbon oil with a density of 3.09 g/cm³. Before each measurement the MRF fluid was thoroughly mixed to distribute the particles uniformly. The sample was then magnetized in a stationary stage for 1 min. The yield stress values as a function of magnetic flux density were determined through the use of steady shear, stress ramp and dynamic oscillatory experiments.

For the plate-and-plate experiment, the shear rate and shear stress vary with radial position complicating the conversion of the measured

torque and angular speed of rotation into shear stress and shear rate. The usual practice is to determine the rheological properties of the fluid at the rim of the plate. For a given plate of radius R , specified gap height h , and angular speed Ω , the rim shear rate, $\dot{\gamma}_R$, can be readily obtained as

$$\dot{\gamma}_R = \frac{\Omega R}{h} \quad (1)$$

By contrast, the rim shear stress, $\tau_{R'}$, cannot be related to the torque, M , by an algebraic equation. The rheometer software used here only calculates the so-called apparent rim shear stress, τ_{Ra} , which is strictly valid for Newtonian fluids only. This is given by

$$\tau_{Ra} = \frac{2M}{\pi R^3} \quad (2)$$

A correction to provide the true rim shear stress can be expressed as (see e.g. [24])

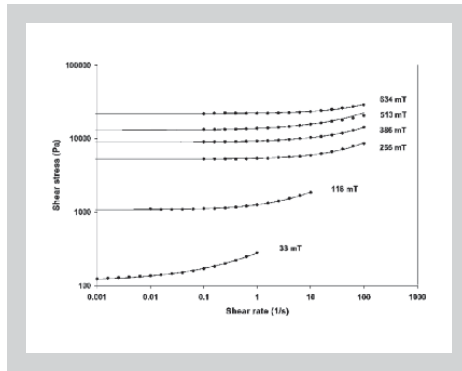
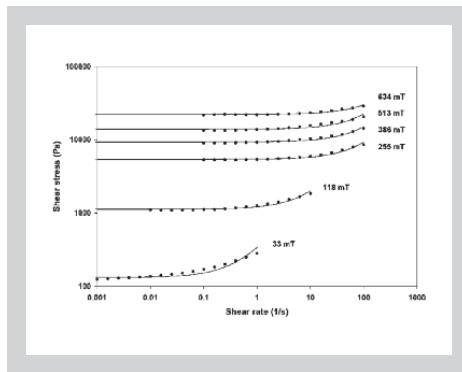
$$\tau_R = \tau_{Ra} \left(\frac{3+n'}{4} \right) = \frac{2M}{\pi R^3} \left(\frac{3+n'}{4} \right) \quad \text{with } n' = \frac{d(\log M)}{d(\log \dot{\gamma}_R)} \quad (3)$$

The derivative required for estimating n' can be obtained by numerical differentiation of the pertinent data. This was accomplished using a two-point central difference approximation, except for the first and last data points where a two-point forward/backward difference approximation was used.

Steady shear measurements were performed in two phases: first the shear rate was increased in logarithmic steps from 0.1 to 100 1/s and then decreased from 100 to 0.1 1/s. At lowest magnetic flux densities (33 and 118 mT) the measuring range was extended to lower shear rates in order to better capture the yield stress. All steady shear results presented in this paper are taken from the second phase, although there were no significant differences between the two results. Extrapolation was then performed to obtain the yield stress as the shear stress limit at zero rate of shear. To facilitate extrapolation, the two-parameter Bingham model and the three-parameter Herschel-Bulkley model were fitted to the experimental data. These can be written as follows:

Figure 1 (above): Shear stress versus shear rate data (symbols) for various flux densities fitted by the Bingham model (lines).

Figure 2: Shear stress versus shear rate data (symbols) for various flux densities fitted by the Herschel-Bulkley model (lines).



$$\tau = \tau_y + \eta_p \dot{\gamma} \quad (4)$$

$$\tau = \tau_y + K \dot{\gamma}^n \quad (5)$$

Here $\dot{\gamma}$ is the shear rate, τ is the shear stress, τ_y is the yield stress, η_p is the plastic viscosity, K is the Herschel-Bulkley parameter and n is the power-law index. To find the best-fit parameters, the method of least squares was used to minimize the overall difference between the experimental data and the model predictions.

In the ramp experiment under the stress-controlled condition, the tested material was subjected to a shear stress that increases logarithmically with time from a very low value to a level well above the yield stress and the resulting shear strain rate was monitored. When the applied stress approaches the yield stress, a sudden increase in the slope of the plot of strain rate versus stress occurs, indicating the onset of flow. Strictly speaking, the variable primarily controlled by the rheometer is the torque from which the stress follows. The rheometer software again uses Equation 2 to relate τ to M , which leads to erroneous results for non-Newtonian fluids. Hence, we use the equation which holds for yield stress fluids close to the yield point (see [25]), that is

$$\tau = \frac{3M}{2\pi R^3} \quad (6)$$

In dynamic testing, the sample between the measuring plates is subjected to sinusoidal oscillatory shear strain with amplitude γ_o and angular frequency ω . In the linear regime for sufficiently small strain amplitude the resulting stress will also be sinusoidal of the same frequency with amplitude τ_o and phase shift δ . The in-phase and out-of-phase components of the response give, respectively, the storage modulus G' and the loss modulus G'' as follows:

$$G' = \frac{\tau_o}{\gamma_o} \cos \delta$$

$$G'' = \frac{\tau_o}{\gamma_o} \sin \delta \quad (7)$$

The strain and stress amplitudes are related to the actual test variables of the plate-and-plate rheometry as $\gamma_o = \phi_o R/h$ and $\tau_o = 2M_o/\pi R^3$, where ϕ_o is the angular amplitude and M_o is the torque amplitude. Dynamic oscillatory experiments were performed with increasing strain amplitude. To extract the yield stress, the concept of the elastic stress ($= G' \gamma_o$) was introduced and the value of the yield stress was taken to be the maximum in the elastic stress when plotted as a function of strain amplitude; such an approach to find the yield stress has been used in some previous studies [26, 27].

3 RESULTS AND DISCUSSION

For the indirect determination of the yield stress, the best fits of the Bingham and Herschel-Bulkley models to the measured steady shear data at different magnetic flux densities need to be established, as illustrated in Figures 1 and 2. Generally the two models appear to perform fairly similarly, with slightly higher extrapolated yield stress estimates being always obtained by the Bingham model. At low magnetic flux densities of 33 and 118 mT the difference between the models becomes somewhat more apparent, yet the yield stress values obtained are still reasonably close to each other.

In the direct measurement of the yield stress with the aid of the stress ramp method, the ramp rate obviously has an effect on the ensuing yield values. To elucidate this matter, measurements were undertaken for three different ramp rates at 513 mT. In these tests, the shear stress was

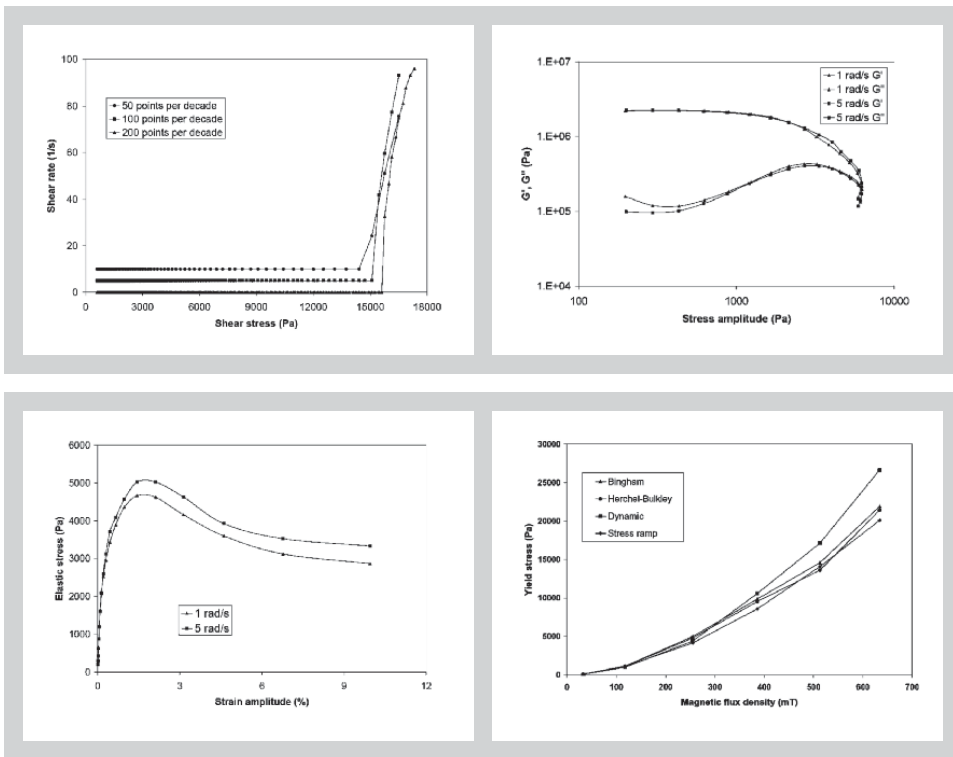


Figure 3 (left above): Stress ramp data obtained for three ramp rates with 513 mT (the data sets for 50 and 100 points per decade are shifted upward for clarity).

Figure 4 (right above): Storage, G' , and loss, G'' , moduli versus strain amplitude for 255 mT with 1 and 5 rad/s.

Figure 5 (left below): Elastic stress versus strain amplitude for 255 mT with 1 and 5 rad/s.

Figure 6 (right below): Yield stress versus magnetic flux density estimated using different techniques.

increased stepwise logarithmically with 200, 100 or 50 stress levels per decade and 3 seconds per data point. As revealed by Figure 3, the shear strain rate first remains virtually at zero indicating solid-like behaviour (note that, for clarity, two of the data sets in this figure have been shifted vertically). When a certain stress is exceeded, the flow initiates and the slope of the shear strain rate versus shear stress curve rapidly increases; the yield stress was determined as the stress on the last data point before this change of slope. It can be seen that the lower the applied ramp rate, the higher the yield stress observed. It is worth noting that this is in contrast to that reported for conventional yield stress fluids [9]. To explain this, one might envisage that when the duration of exposure to magnetic field increases the structure of the MR fluid becomes stronger giving rise to a higher yield stress. Indeed, there is some indication about the transient response of MR fluids over long periods of time. However, the reported observations are contradictory since, under constant shear rate, the shear stress has been found both to gradually increase [28] and decrease [29] with time. The rest of the ramp tests in this work were run using the intermediate rate of 100 steps per decade.

In the dynamic oscillatory experiments, the storage (G') and loss (G'') moduli of the sample were determined as a function of the strain amplitude. With increasing amplitude both

moduli eventually show a distinct decrease, which is particularly clearly seen when G' and G'' are plotted against the stress amplitude (see Figure 4). From this kind of experiment the stress amplitude value at the inflection point of G' or at the crossover point of G' and G'' can be interpreted as the yield stress. In the present study, however, the maximum of the elastic stress ($= G'\gamma_0$) was chosen as an estimate of the yield stress. Since the value of the angular frequency used in the experiments can affect the obtained results, two different values, 1 and 5 rad/s, were tried out under the magnetic flux density of 255 mT. As seen from Figures 4 and 5, the angular frequency has an influence on G' and G'' as well as on the resulting yield stress. The angular frequency of 1 rad/s was chosen for subsequent experiments. It is worth mentioning that the applicability of the dynamic oscillatory testing for determining the yield stress has been questioned by some researchers by the arguments that such inferred yield stress is always frequency dependent and that at no frequency does it correlate with the yield stress extrapolated from the flow curve [30].

The yield stresses as a function of magnetic flux density estimated using different techniques are compared in Figure 6. All values are averages of two measurements. The yield stresses determined by the indirect method and the stress ramp test compare quite well with each

other through the whole flux density range. The values obtained by the dynamic oscillatory testing are at the same level with others at low flux densities, but become higher when the flux density increases. It is worth noting that the stress ramp test gave the lowest values of all, which is in accordance with the results of Ulicny et al. [17].

All measurements were made for at least two samples to get some information about the reliability and reproducibility of the measurements. In general, it turned out that the scatter associated with the measurements decreases with increasing magnetic flux density regardless of the test method. It is evident, however, that no definite judgments can be made on the merits of different techniques studied here. Yet, particularly at higher magnetic flux densities the extrapolation of the steady flow curve appears to be a rather straightforward and reliable way to determine the yield stress of the MR fluid. At low magnetic flux densities the scatter with this method is quite large (more than $\pm 10\%$), but decreases clearly with increasing magnetic flux density. The stress ramp technique, on the other hand, exhibits the lowest scatter (less than $\pm 5\%$), but the yield stress results tend to be dependent on the ramp rate at least within the experimental parameter range used here. A similar drawback is encountered with the dynamic oscillatory testing, that is, the yield stress values attained are frequency dependent. The scatter with this type of experiment was between $\pm 5 - 15\%$ depending on the applied magnetic flux density.

In the present work, the interpretation of the rheological data was based on the assumption that the no-slip condition prevails at the fluid-plate interfaces of the rheometer. It is, however, well known that slip may occur particularly for complex fluids like suspensions and emulsions. It is possible to detect the presence of slip with the plate-and-plate measuring geometry by varying the gap between the plates. If slip occurs, the measured shear stress at a fixed nominal shear rate appears to decrease with decreasing gap. To examine this matter, a couple of steady shearing experiments were also conducted with gaps less than 1 mm. A point worth noting here is that for a given coil current the magnetic flux density within the sample increases with decreasing gap, as demonstrated by Mazlan et al. [31]. Thus, in order to allow for a meaningful evaluation of slip the input current needs to be

adjusted to give a comparable flux density for each gap. Within the experimental uncertainty, the data measured with different gaps coincided with each other implying the absence of slip.

4 CONCLUSIONS

The characterization of the field-dependent yield stress is essential for the development of MR fluid technology. Using the rotational rheometer with a magnetic field generator and a plate-and-plate configuration, we compared a variety of techniques for determining the yield stress of a commercial MR fluid as a function of magnetic flux density. The yield stress values were determined using steady shear, stress ramp and dynamic oscillatory measurements. Comparison of the results showed relatively good agreement between the methods.

REFERENCES

- [1] Bossis G, Volkova O, Laciş S, Meunier A: Magnetorheology: fluids, structures and rheology, in: Ferrofluids: Magnetically Controllable Fluids and Their Applications, Odenbach S (Ed), Springer, Berlin (2002).
- [2] Goncalves, FD, Koo J-H, Ahmadian M: A review of the state of the art in magnetorheological fluid technologies - Part I: MR fluid and MR fluid models, Shock Vib. Dig. 38 (2006) 203-219.
- [3] Wang X, Gordaninejad F: Magnetorheological materials and their applications, in: Intelligent Materials, Shahinpoor M, Schneider H-J (Ed), RSC Publishing, Cambridge (2007).
- [4] Barnes HA, Walters K: The yield stress myth?, Rheol. Acta 24 (1985) 323-326.
- [5] Barnes HA: The yield stress – a review or ‘*πει παντα*’ – everything flows?, Non-Newtonian Fluid Mech. 81 (1999) 133-178.
- [6] Nguyen QD, Boger DV: Measuring the flow properties of yield stress fluids, Annu. Rev. Fluid. Mech. 24 (1992) 47-88.
- [7] Tiu C, Guo J, Uhlherr PHT: Yielding behaviour of viscoplastic materials, J. Ind. Eng. Chem. 12 (2006) 653-662.
- [8] A. Sun, S. Gunasekaran. Yield stress in foods: measurements and applications. Int. J. Food Prop. 12 (2009) 70-101.
- [9] Nguyen QD, Akroyd T, De Kee DC, Zhu L: Yield stress measurements in suspensions: an inter-laboratory study, Korea-Australia Rheol. J. 18 (2006) 15-24.
- [10] Genc S, Phule PP: Rheological properties of magnetorheological fluids, Smart Mater. Struct. 11 (2002) 140-146.
- [11] Li WH, Du H: Design and experimental evalua-

- tion of a magnetorheological brake, *Int. J. Adv. Manuf. Technol.* 21 (2003) 508-515.
- [12] Mantripragada S, Wang X, Gordaninejad F, Hu B, Fuchs A: Characterization of Rheological Properties of Novel Magnetorheological Fluids, *Proc. 10th Int. Conf. on ER Fluids and MR Suspensions* (2006) 180-186.
- [13] Ngatu GT, Wereley NM: High versus low field viscometric characterization of bidisperse MR fluids, *Proc. 10th Int. Conf. on ER Fluids and MR Suspensions* (2006) 263-269.
- [14] Yeow YL, Leong Y-K, Khan A: Error introduced by a popular method of processing parallel-disk viscometry data, *Appl. Rheol.* 17 (2007) 664-15.
- [15] Kordonski W, Gorodkin, S, Zhuravski N: Static Yield Stress in Magnetorheological Fluid, *Int. J. Mod. Phys. B15* (2001) 1078-1084.
- [16] Bombard AJF, Knobel M, Alcantara MR, Joekes I: Evaluation of magnetorheological suspensions based on carbonyl iron powders, *J. Int. Mat. Syst. Struct.* 13 (2002) 471-478.
- [17] Ulicny JC, Golden MA: Evaluation of yield stress measurement techniques on a parallel plate magnetic rheometer, *Int. J. Mod. Phys. B21* (2007) 4898-4906.
- [18] Yang Y, Li L, Chen G: Static yield stress of ferrofluid-based magnetorheological fluids, *Rheol. Acta* 48 (2009) 457-466.
- [19] Li WH, Du H, Chen G, Yeo SH: Experimental investigation of creep and recovery behaviors of magnetorheological fluids, *Mater. Sci. Eng. A333* (2002) 368-376.
- [20] Keentok M, See H: Behavior of field-responsive suspensions under oscillatory shear flow, *Korea-Australia Rheol. J.* 19 (2007) 117-123.
- [21] Laun HM, Gabriel C, Kieburg CH: Magnetorheological fluid (MRF) in oscillatory shear and parameterization with regard to MR device properties, *J. Phys.: Conf. Ser.* 149 (2009) 012067.
- [22] Laeuger J, Wollny K, Stettin H, Huck S: A new device for the full rheological characterization of magneto-rheological fluids, *Proc. 9th Int. Conf. on ER Fluids and MR Suspensions* (2004) 370-376.
- [23] Laun, HM, Schmidt G, Gabriel C, Kieburg C: Reliable plate-plate MRF magneto-rheometry based on validated radial magnetic flux density profile simulations, *Rheol. Acta* 47 (2008) 1049-1059.
- [24] Macosko CW: *Rheology: Principles, Measurements, and Applications*. VCH Publishers, New York (1994).
- [25] Brunn PO, Asoud H: Analysis of shear rheometry of yield stress materials and apparent yield stress materials, *Rheol. Acta* 41 (2002) 524-531.
- [26] Yang MC, Scriven LE, Macosko CW: Some rheological measurements on magnetic iron oxide suspensions in silicone oil, *J. Rheol.* 30 (1986) 1015-1029.
- [27] Walls HJ, Caines SB, Sanchez AM, Khan SA: Yield stress and wall slip phenomena in colloidal silica gels, *J. Rheol.* 47 (2003) 847-868.
- [28] Ulicny JC, Golden MA, Namuduri CS, Klingenberg DJ: Transient response of magnetorheological fluids: shear flow between concentric cylinders. *J. Rheol.* 49 (2005) 87-104.
- [29] Ciocanel C, Molyet K, Yamamoto H, Vieira SL, Naganathan NG: Magnetorheological fluid behavior under constant shear rates and high magnetic fields over long time periods, *ASME J. Eng. Mater. Technol.* 128 (2006) 163-168.
- [30] Masalova I, Malkin AY, Foundazi R, Yield stress of emulsions and suspensions as measured in steady shearing and in oscillations, *Appl. Rheol.* 18 (2008) 44790.
- [31] Mazlan SA, Issa A, Chowdhury HA, Olabi AG: Magnetic circuit design for the squeeze mode experiments on magnetorheological fluids, *Mater. Des.* 30 (2009) 1985-1993.



Publication II

Ilari Jönkkäri, Esa Kostamo, Jari Kostamo, Seppo Syrjälä and Matti Pietola

Effect of the plate surface characteristics and gap height on yield stress of a magnetorheological fluid

Journal of Smart Materials and Structures 21(7) (2012) 075030

© 2012 IOP Publishing
Reprinted with permission

Effect of the plate surface characteristics and gap height on yield stresses of a magnetorheological fluid

I Jonkkari¹, E Kostamo², J Kostamo², S Syrjala¹ and M Pietola²

¹ Department of Materials Science, Tampere University of Technology, PO 589, FI-33101 Tampere, Finland

² Department of Engineering Design and Production, Aalto University, PO 14400, FI-02150 Helsinki, Finland

E-mail: ilari.jonkkari@tut.fi

Received 28 February 2012, in final form 16 May 2012

Published 28 June 2012

Online at stacks.iop.org/SMS/21/075030

Abstract

Effects of the plate material, surface roughness and measuring gap height on static and dynamic yield stresses of a magnetorheological (MR) fluid were investigated with a commercial plate–plate magnetorheometer. Magnetic and non-magnetic plates with smooth ($R_a \sim 0.3 \mu\text{m}$) and rough ($R_a \sim 10 \mu\text{m}$) surface finishes were used. It was shown by Hall probe measurements and finite element simulations that the use of magnetic plates or higher gap heights increases the level of magnetic flux density and changes the shape of the radial flux density profile. The yield stress increase caused by these factors was determined and subtracted from the measured values in order to examine only the effect of the wall characteristics or the gap height. Roughening of the surfaces offered a significant increase in the yield stresses for non-magnetic plates. With magnetic plates the yield stresses were higher to start with, but roughening did not increase them further. A significant part of the difference in measured stresses between rough non-magnetic and magnetic plates was caused by changes in magnetic flux density rather than by better contact of the particles to the plate surfaces. In a similar manner, an increase in gap height from 0.25 to 1.00 mm can lead to over 20% increase in measured stresses due to changes in the flux density profile. When these changes were compensated the dynamic yield stresses generally remained independent of the gap height, even in the cases where it was obvious that the wall slip was present. This suggests that with MR fluids the wall slip cannot be reliably detected by comparison of flow curves measured at different gap heights.

(Some figures may appear in colour only in the online journal)

1. Introduction

Magnetorheological (MR) fluids are suspensions of magnetizable particles in a non-magnetic Newtonian liquid. The particles are typically spherical and composed of a ferromagnetic material such as carbonyl iron. The MR effect is seen as a rise in the apparent suspension viscosity and appearance of the yield stress upon the application of a magnetic field. The effect is caused by the formation of particle structures that hinder fluid flow. Structures are

columnar at static no-flow conditions and become lamellar under shearing [1].

Rheological properties of MR fluids are typically measured with a rotational rheometer and plate–plate geometry. Measurement is based on the assumption that there is no slip between the measured fluid and the measuring geometry. If the sample slips on the surfaces, the measured values are smaller than true values and incorrect interpretations can therefore be made from the results. This kind of wall slip phenomenon is common when measuring

suspensions. There are two types of wall slip: true and apparent. True slippage appears as adhesive failure between the fluid and the measuring geometry in direct violation of the no-slip condition. In apparent wall slip the dispersed phase of the suspension is displaced away from the surface of the measuring geometry, leaving a depleted layer of liquid that has lower viscosity. A common way to determine whether slip occurs with a particular material is to change the gap between measuring plates. If the wall slip is present, the measured values should increase with increasing gap [2]. Another way is to make measurements with different geometries, for example with smooth and rough surfaces, and compare the results. The values should be the same if slippage is absent in both cases.

The effect of the gap height in the rotational rheometry of MR fluids has been studied in a couple of papers. López-López *et al* used the plate–plate geometry with a gap height of 0.01–0.4 mm and measuring plates that were roughened by gluing sandpaper on the plate surfaces. The results showed that in the pre-yield regime there is a strong increase in the shear stress as the gap height is increased. Similar gap dependence was not observed in the measured static and dynamic yield stress values [3]. In their study, de Vicente *et al*, using stainless steel plates with 0.1, 0.3 and 0.5 mm gap heights, also reported a negligible gap dependence of the dynamic yield stress at low magnetic field strengths. By contrast, the static yield stress decreased with increasing gap height. The authors postulated that this could be related to the wall slip [4].

A typical method to eliminate the effect of slippage is to change the physical nature of the plate surfaces usually by roughening or grooving them. The effect of the surface roughness on wall slip with MR fluids has been briefly covered in papers by López-López *et al* and de Vicente *et al*. In both studies rougher surfaces proved to suppress the wall slip effects efficiently. A more thorough study was provided by Laun *et al* using the rotational rheometer with plate–plate geometry. The authors studied the effect of the plate material and the plate surface roughness on the transmittable shear stresses. Non-magnetic brass and magnetic iron materials were used with different surface roughness. Generally, magnetic geometries gave higher shear stress values than non-magnetic, but the grooving of the surfaces did not further increase the values. The measured shear stresses with non-magnetic plates could be increased up to the level of magnetic plates by roughening or grooving the plates [5]. Lemaire and Bossis also studied the effect of the surface characteristics on the measured yield stress values. They used non-magnetic stainless steel and magnetic iron plates with surface roughness of about 10 μm . Ferromagnetic plates gave significantly higher yield stresses. This was proposed to be caused by strong attractive interactions between the wall and the particles. Very low yield stresses were measured with non-magnetic plates which had a glass layer embedded on the surface of the plates. The surface roughness was smaller than the particle size and particles could therefore slip easily on the surface [6].

In this study we report the effect of the plate material, surface roughness and measuring gap height on static and

dynamic yield stresses of a MR fluid. First, we address the influence of magnetic geometries and gap height variation on the level of magnetic flux density and the shape of radial flux density profile by means of Hall probe measurements and finite element simulations. Then we present a method to calculate the increase in yield stress caused by these factors. Finally, the calculated values are used to subtract the influence of the flux density changes from the measured yield stresses, making it possible to compare only the effect of the wall characteristics or the gap height. The results show that the changes in magnetic flux density due to plate materials or gap height can have a significant effect on the measured stresses. It seems that in our study the higher yield stresses measured with magnetic geometries are mostly caused by increased magnetic flux density rather than by a better contact of the particles to the plate surfaces. Also an increase in gap height will result in higher flux densities that have to be taken into account when comparing measured stresses. The seemingly small changes in magnetic flux density profile can lead to significant changes in measured stresses, since the MR fluids yield stress increases exponentially with the flux density.

2. Experimental details

2.1. Sample

The MR fluid was prepared by mixing 80 wt% carbonyl iron particles (CIP) into a carrier fluid. The carrier fluid was Dow Corning® 200/50cS silicone oil. The oil has a viscosity of 0.05 Pa s and density of 0.96 g cm⁻³. The particle was a mechanically hard BASF OM grade with a diameter from 3.9 to 5.2 μm . The fluid remained stable against sedimentation during measurements, thus no additives were needed for the stabilization. Particles and carrier fluid were first mixed by hand and then in an ultrasonic mixer for half an hour. Fluid was always remixed prior to measurements. The dosing of the sample to the measuring gap was done with a syringe.

2.2. Rheometer

Rheological properties of the MR fluid were measured with an Anton Paar Physica MCR301 rotational rheometer equipped with a MRD180/1T magneto-cell. The measuring system uses plate–plate measuring geometry that consists of a stationary bottom plate and a rotating top plate. The schematic of the magneto-cell is given in figure 1. The temperature of the cell was held at 30 °C with a circulating bath.

2.3. Measuring geometries

Custom plate–plate geometries with different plate materials and surface roughness were used in measurements. The rotor was designed in a way that the aluminum plate part was changeable and the steel adaptor remained the same (figure 2).

The shape and dimensions of the plates were mainly equivalent to the original Anton Paar design with 21 mm plate diameter. The thickness of the bottom plate was slightly

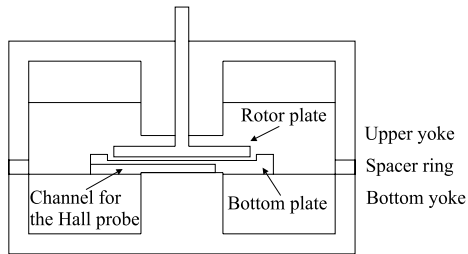


Figure 1. Schematic of the MRD180/IT magneto-cell.



Figure 2. Custom made geometry with and without the adaptor.

larger than the original (1.8 mm versus 2.2 mm). Additional vertical space for the plate was obtained by raising the upper yoke of the magneto-cell 0.5 mm by machining a thicker ferromagnetic spacer ring between the yokes. The total number of geometries was four, two of which were manufactured completely from aluminum and two had a 0.2 mm thick ferromagnetic plate embedded on the top. Smooth and roughened configurations were manufactured from both types (figure 3). Ra surface roughness was measured to be about $0.30 \mu\text{m}$ for the smooth and $10 \mu\text{m}$ for the rough surfaces. The bottom plate had a similar surface to the rotor.

2.4. Magnetic field

The magneto-cell generates a vertical magnetic field that passes through the measuring gap. In the literature, it has been reported that the radial magnetic flux density profile in the gap is not completely flat but shows peaking at the rim of the measuring geometry [7]. However, the measured values fail to tell the precise magnetic flux density profile in the middle plane of the measuring gap as it is measured from a slightly different location. The thickness of the Hall probe also limits the possibilities to directly measure the magnetic flux density in the fluid gap since in many cases the thickness of the Hall probe is greater than the height of the fluid gap.

To be able to estimate the distribution of the magnetic flux density in the fluid gap, a magnetic model of the rheometer was created by using finite element method magnetics (FEMM) software. In FEMM software the non-linear magnetic properties of the MR fluid and the yoke material can be taken into account, and for the model creation the details of

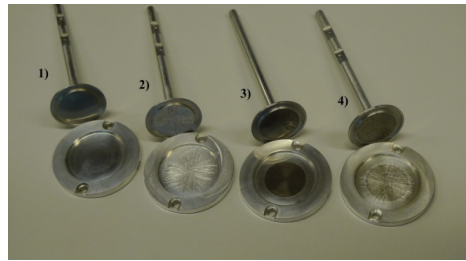


Figure 3. Measuring geometries, (1) smooth non-magnetic, (2) roughened non-magnetic, (3) smooth magnetic, (4) roughened magnetic.

the MRD180/IT magneto-cell were kindly provided by Anton Paar GmbH.

Figure 4 presents a detailed view of the fluid gap area of one of the meshed FEMM models used in this study. In figure 4 the fluid gap height is set to 0.5 mm and the model includes the magnetic geometries (i.e. ferromagnetic plates in the MR fluid gap) and MR fluid in the gap. The fluid gap region is limited with a curve from the right-hand side and with a horizontal line from the top in order to be able to use finer mesh sizes in the magnetically most interesting area. The size of the triangular mesh in the MR fluid and the ferromagnetic plates was set to 0.02 mm, which corresponds to the average height of the element.

Material specific details of the FEMM model are also pointed out in figure 4. In order to attain quantitatively reliable results by finite element modeling, it is important to pay attention to the magnetization properties of the materials used in the model. The permeability related properties of the modeled materials may be found in the literature or may be selected from the material library of the software, but it should be noticed that mechanical machining or thermal treatments of the core parts may change their magnetic properties notably compared to the ideal material properties and consequently yield inaccurate results.

While building up the FEMM model there was no precise information available on the magnetic properties of the yoke material of the MRD180/IT magneto-cell, and therefore the magnetic characteristics of the yoke material were defined semi-experimentally. As a starting point for the yoke material, Hiperco-50 magnetic alloy was used, and the final magnetic properties were found by modification of the Hiperco-50 material based on the magnetic flux density measurements.

The radial profiles of the magnetic flux densities were measured with a FW Bell Model 5180 T meter and STD18-0404 Hall probe. The channel for the flux density measurement was machined underneath the bottom plate in such a way that the Hall probe was located 1.7 mm underneath the surface of the bottom plate. Measurement in the radial direction was carried out by moving the probe in 0.5 mm steps from the middle of the plate towards the rim. A custom made actuator was manufactured to ensure precise and repetitive movement of the probe. The vertical location and the radial range of the measurement are illustrated in figure 4 by the

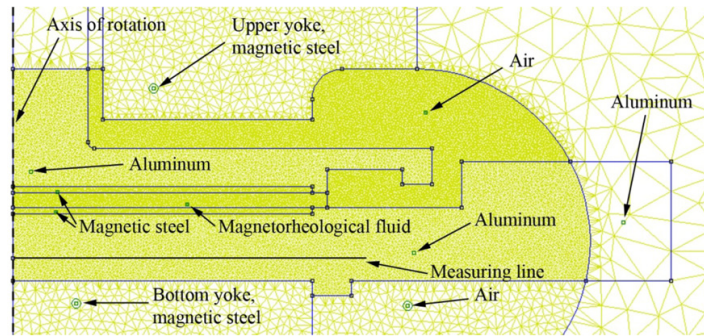


Figure 4. Meshed FEMM model of the MRD180/1 T magneto-cell.

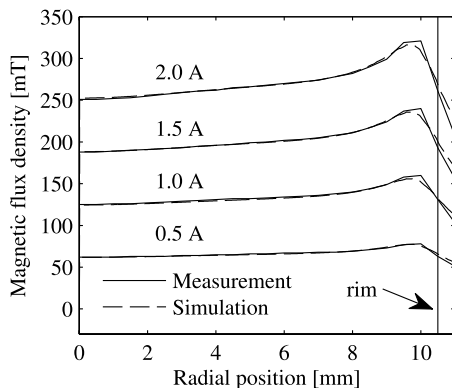


Figure 5. Comparison of the measured and simulated radial flux density profiles for the non-magnetic geometry with a 0.25 mm high empty gap.

measurement line. In the identification measurements of the magnetic flux density, non-magnetic geometries were used with an empty fluid gap with a height of 0.5 mm.

After identification the yoke material was named in a non-specific way as magnetic steel (figure 4). The magnetic properties of the yoke material were validated by repeating the magnetic flux density measurements with a fluid gap height of 0.25 mm and by comparing measured results with the simulated responses. The comparison of the measured and simulated responses is shown in figure 5 where a good agreement between these two responses, at each value of the electric current, can be found. In figure 5 the fluid gap related rim of the rotating geometry is indicated with a vertical solid line.

The magnetization curve of the identified magnetic steel is presented in figure 6(a). In the identification of the yoke material it was assumed that the absolute value of the magnetic saturation of the yoke material is not essential in this study, since the yoke material will not reach the saturation point in the measurements. From figure 5 it can be seen that with an empty fluid gap the magnetic density responds linearly to the applied electric current, i.e. if the electric current is doubled the magnetic flux density is also

doubled, illustrating no saturation in the yoke material. The magnetization properties of the 80 wt% (32 vol%) MR fluid, used in the FEMM model, are presented in figure 6(b).

The reliability of the FEMM model was also validated with MR fluid in the fluid gap. Figure 7 presents the simulated and measured results where non-magnetic geometries have been used with a 0.5 mm fluid gap filled with MR fluid. From figure 7 it can be seen that the shape of the radial distribution of the magnetic flux density is fairly flat with only slightly increasing trend in the direction of the rim. The simulated responses can be found to correlate accurately with the measured results with only 3% systematic underestimation at each value of electric current. The accuracy of the FEMM modeling was found to be the same between the similar measurements and simulations where 0.25 mm or 1.0 mm fluid gaps were used.

To study and validate the difference between the non-magnetic and magnetic geometries from the magnetic flux density profile point of view, the same measurements as described in figure 7 were repeated with the magnetic geometries, and the responses were also simulated. The comparison of the simulated and measured results is presented in figure 8. From the results it can be seen that the magnetic flux density distribution is perfectly flat with only a small increase of the intensity near the rim. Based on the results in figure 8 it can be perceived that only a 0.2 mm thick ferromagnetic plate, embedded in the magnetic geometries, is thick enough to equalize even the small radial magnetic flux density gradient that was found with the non-magnetic geometries in figure 7. The evenly distributed magnetic flux density in the radial direction in the fluid gap is important in order to minimize the CIP migration towards higher magnetic flux density intensities with time.

By comparing the measured and simulated responses with magnetic geometries in figure 8, a nearly identical 3% underestimation of the simulated response can be observed in respect to non-magnetic geometries (figure 7). One possibility for this difference was estimated to be caused by the inaccurate dosing or insufficient homogenization of the sample fluid before dosing into the fluid gap. On the other hand, all the fluid samples were thoroughly mixed with an ultrasound mixer and mechanically stirred before

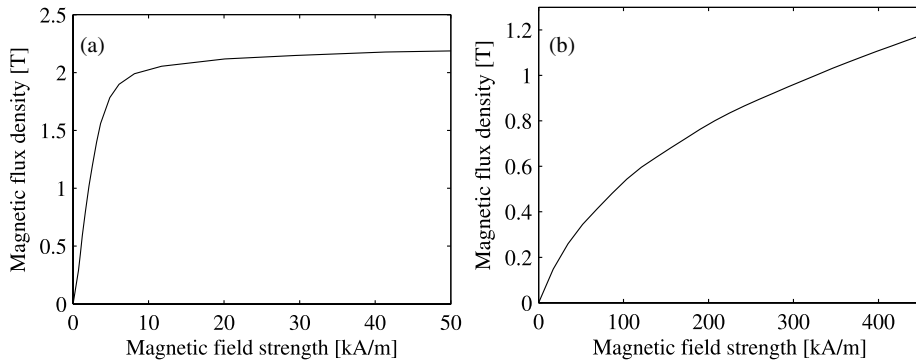


Figure 6. (a) Magnetization curve of the magnetic steel (modified Hiperco-50). (b) Magnetization curve of the MR fluid (80 wt%) [8].

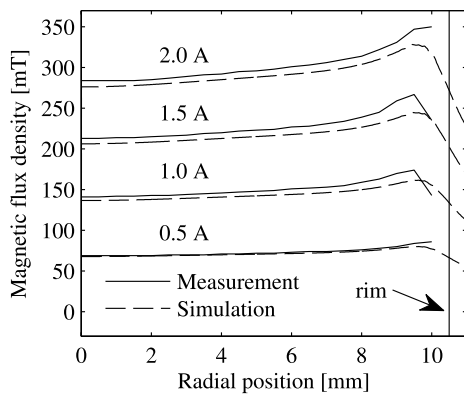


Figure 7. Comparison of measured and simulated radial flux density profiles with a 0.5 mm fluid gap, 80 wt% MR fluid and non-magnetic geometries.

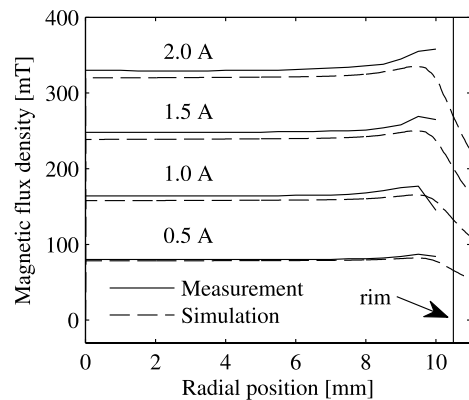


Figure 8. Comparison of measured and simulated radial flux density profiles with a 0.5 mm fluid gap, 32 vol% MR fluid and magnetic geometries.

dosing into the fluid gap in order to ensure a homogeneous composition of the MR fluid. It was assumed that if large variation had occurred in the CIP concentration in the MR fluid sample or the dosing volume had been inaccurate, these issues would have caused a larger and more unsystematic error between the measured and simulated responses while using magnetic or non-magnetic geometries. Another possible cause for the difference between the simulated and measured results was considered to be the slightly different magnetization properties of the sample MR fluid compared to the magnetization characteristics of the MR fluid presented in figure 5(b) that was used in the FEMM model. This kind of difference could be based on the difference between the magnetization properties of the CIP used in the sample MR fluid and in the MR fluid that is validated in figure 5(b). However, by taking into account that the FEMM model was based on the real geometry and material properties of the magneto-cell, the accuracy of the simulated results was proven to be satisfactory in order to be able to estimate the magnetic flux density in the middle of the fluid gap.

Figure 9 depicts the simulated radial magnetic flux density profiles in the middle of the fluid gap filled by MR fluid for three applied electric currents and for three different fluid gap heights with magnetic geometries. In figure 9 the solid lines represent a 1.0 mm fluid gap height, the broken line a 0.5 mm fluid gap height and the dash-dot line a 0.25 mm fluid gap height, respectively. The results reveal that the shape of the radial magnetic flux distribution is fairly flat up to the radius of 9.7 mm, followed by a drop next to the rim of the rotating geometry. The increase of the magnetic flux density as a consequence of the elevation of the fluid gap height can be clearly noticed at each value of the electric current. This can be considered logical, since by the elevation of the fluid gap height the amount of higher permeable material (i.e. MR fluid), compared to air, is increased between the upper and bottom yokes of the magneto-cell, and thereby the total reluctance between the upper and lower yokes is diminished and the magnetic flux in the fluid gap is strengthened.

In order to be able to study and compare the difference between different radial magnetic flux density distributions in the fluid gap, the rheology-relevant average magnetic flux

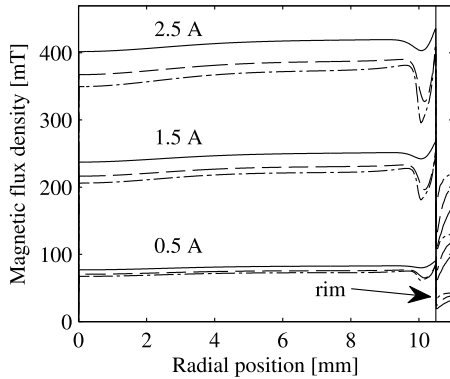


Figure 9. Simulated magnetic flux densities in the middle of the fluid gap filled by MR fluid, at different electric currents and fluid gap heights. Solid line: 1.0 mm fluid gap, broken line: 0.5 mm fluid gap, dash-dot line: 0.25 mm fluid gap.

density \bar{B} [5] has been calculated by equation (1) for all the fluid gap heights and all the applied electric currents.

$$\bar{B} = \frac{\sum_0^R B(r_i) r_i^2 \Delta r}{\sum_0^R r_i^2 \Delta r}. \quad (1)$$

This is particularly necessary while comparing the simulated flux densities between the magnetic and non-magnetic geometries, since the general shape of the radial magnetic flux density distribution is slightly different depending on the magnetic material properties of the geometries. By using the rheology-relevant average magnetic flux density, the dominating effect of the intensity of the magnetic flux density B at greater radial locations r_i will be also taken into account.

For the magnetic geometries, the rheology-relevant average magnetic flux densities are shown in figure 10 as a function of the electric current and the fluid gap height filled by MR fluid. The results in figure 10 are calculated based on the simulations presented in figure 9, and a linear correspondence between the electric current and the average magnetic flux density can be found at each fluid gap height. In figure 10 the average flux density intensities have been calculated from the center axis up to a radius of 10.5 mm. By analyzing the influence of the fluid gap height it can be estimated that an elevation of 0.25 mm of the fluid gap height increases the intensity of the average magnetic flux density by approximately 4.5%.

The same analysis for the rheology-relevant average magnetic flux density was repeated with the non-magnetic rheometer geometries, and the simulated results are presented in figure 11. By comparing the magnetic flux density responses between different fluid gap heights, the same increase of approximately 4.5% in the magnetic flux density per 0.25 mm in the fluid gap height can be found as estimated in the case of magnetic geometries in figure 10. Further, by comparing the absolute values of magnetic flux density between magnetic and non-magnetic geometries it can be

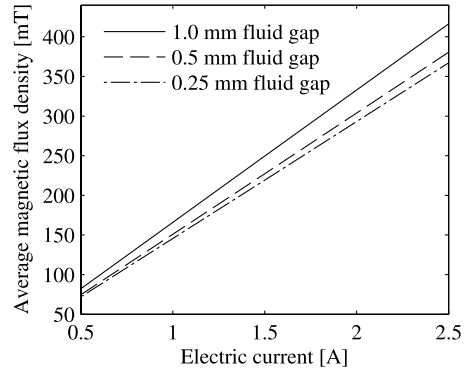


Figure 10. Rheology-relevant average magnetic flux density in the middle of the fluid gap as a function of the fluid gap height and electric current. The fluid gap is filled by MR fluid and magnetic geometries are used.

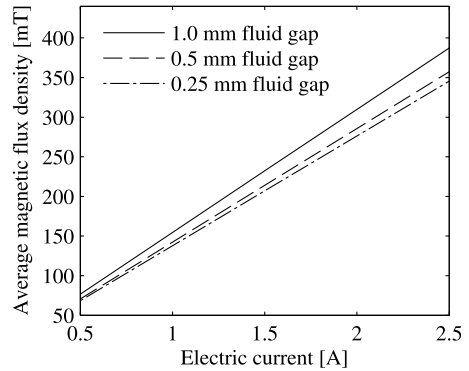


Figure 11. Rheology-relevant average magnetic flux density in the middle of the fluid gap as a function of the fluid gap height and electric current. The fluid gap is filled by MR fluid and non-magnetic geometries are used.

analyzed that the magnetic geometries, used in this study, yield a 7% higher magnetic flux density in the fluid gap than non-magnetic geometries. The result is quite obvious since the ferromagnetic plates, embedded in the magnetic geometries, strengthen the magnetic flux between the upper and lower yokes and thus also between the MR fluid gap. However, the magnetic flux strengthening characteristics of the magnetic geometries are important to be taken into account while analyzing and comparing the rheology measurements with the MR fluid.

2.5. Rheological measurements

The dynamic yield stress was evaluated from the flow curve measured in strain controlled mode. During the measurement the shear rate was logarithmically increased from 0.001 to 100 1/s and the resulting stress was monitored. The rheometer software used here calculates the true rim shear rate $\dot{\gamma}_R = \Omega R/h$, where Ω is angular velocity, R plate radius and h gap

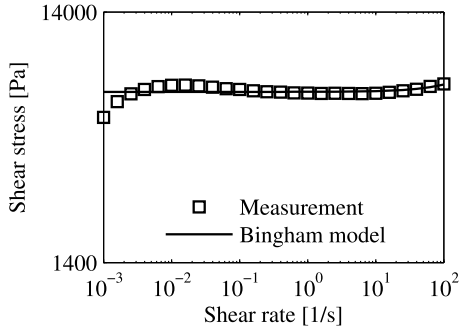


Figure 12. Extraction of the dynamic yield stress from the flow curve using the Bingham model.

height. The shear stress, however, is the so-called apparent rim shear stress $\tau_{Ra} = 2M/\pi R^3$, where M is the torque, which is strictly valid for Newtonian fluids only. Therefore a correction to provide the true rim shear stress τ_R was applied to data as follows:

$$\tau_R = \tau_{Ra} \left(\frac{3 + n'}{4} \right) \quad \text{where } n' = \frac{d(\log M)}{d(\log \dot{\gamma}_R)}. \quad (2)$$

The correction is expressed in more detail elsewhere [9]. The Bingham model was then fitted on corrected data to extrapolate the shear stress to a zero shear rate that was determined as the dynamic yield stress. The principle is illustrated in figure 12. The Bingham model is as follows:

$$\tau = \tau_y + \eta_p \dot{\gamma} \quad (3)$$

here η_p is the plastic viscosity.

The static yield stress was measured in a stress controlled mode with a tangent method. The sample was sheared at 10 1/s prior to measurement for 1 min and then let rest under magnetic field for half a minute. During the measurement the sample was subjected to shear stress that increased logarithmically with time from a very low value to a level well above the static yield stress, and the resulting strain was monitored. When the applied stress approaches the static yield stress, the slope of the strain versus stress suddenly increases, as illustrated in figure 13. The static yield stress was determined from the point where the tangent, which was fitted to the portion of the curve after the slope change, crossed the x -axis. A correction to provide the true rim shear stress is needed here also. We use the equation which holds for yield stress fluids close to the yield point (see [10]):

$$\tau = \frac{3M}{2\pi R^3}. \quad (4)$$

2.6. Effect of the magnetic flux density on the yield stress

As presented in section 2.4, the magnitude of the magnetic flux density depends not only on the electric current but also on the amount of material with high magnetic permeability between the upper and bottom yokes. At moderate flux

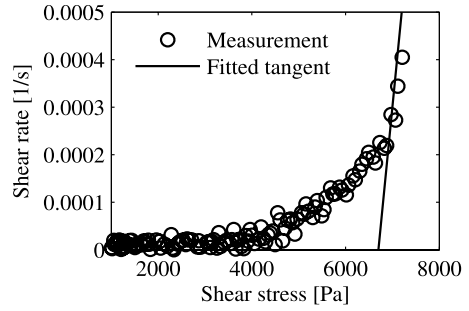


Figure 13. Determination of the static yield stress with a tangent method.

densities, the yield stress of MR fluids has been shown to be proportional to the magnetic flux density with an exponent of 1.5 by theoretical and experimental studies [11, 12]. Increase in magnetic flux density due to the use of magnetic plates or higher gap heights may therefore have a significant influence on the strength of the MR fluid and should be taken into account when comparing results of the rheological measurements. A power law model was fitted on measured yield stresses $\tau_{y,meas}$ as a function of \bar{B} by minimizing the sum of squares of the relative deviation between measured and fitted data points.

$$\tau_y = A\bar{B}^n. \quad (5)$$

The value of exponent n for our system varied from 1.66 to 1.72 with static and from 1.78 to 1.81 with dynamic yield stresses and was highest for magnetic geometries. Dynamic yield stress has been reported to increase faster than static yield stress also by Kordonski *et al* [11]. Generally the power law model fits reasonably well on the measured values, but slightly overshoots static yield stresses measured using non-magnetic geometries and a 2.5 A electric current as presented in figure 14. The measured values are drawn with symbols (smooth plates = diamonds, rough plates = circles) and the power law fits with solid lines. The overshoot is more likely caused by differences in the MR fluid–plate interface rather than in the saturation behavior of the CIP since similar behavior was not observed with magnetic surfaces.

A linear relationship between rheology-relevant average magnetic flux densities measured at different gap heights or non-magnetic and magnetic geometries was observed in section 2.4. A theoretical increase in yield stress $\Delta\tau_y$ caused by the increase in \bar{B} can therefore be calculated as follows:

$$\bar{B}_h = K\bar{B}_{ref} \quad (6)$$

$$\Delta\tau_y = A[(K\bar{B}_{ref})^n - \bar{B}_{ref}^n]. \quad (7)$$

Here \bar{B}_h represents the system with the same electric current as \bar{B}_{ref} , but using a higher gap height or magnetic plates. An increase of similar degree was also expected in the measured yield stress:

$$\Delta\tau_{y,meas} = \tau_{y,meas} \frac{(K\bar{B}_{ref})^n - \bar{B}_{ref}^n}{\bar{B}_{ref}^n}. \quad (8)$$

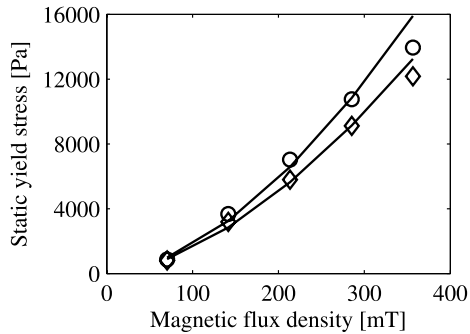


Figure 14. Fits between measured static yield stresses (symbols) and the power law model (solid lines). The results for smooth non-magnetic plates are drawn with diamonds and for rough plates with circles.

It should be noted that the normal forces arising from multiparticle interactions in MR fluid will also have an effect on gap height, as Laun *et al* show in their paper [5]. However, the gap opening due to normal forces is small compared to the overall change here, thus it will be neglected.

Accuracy of the equation (8) was studied by performing two sets of dynamic yield stress measurements with smooth magnetic plates. In the first set electric currents were kept the same as with non-magnetic plates and the effect of the higher magnetic flux density was compensated by subtracting the value of equation (8) from the measured value. In the second set the electric currents were manually adjusted so that the magnitude of the average magnetic flux density was the same as with non-magnetic plates. Electric currents used in this case were 0.47, 0.95, 1.41, 1.88 and 2.35 A. The results are presented in figure 15. Original results from the first set are drawn with diamonds, the same results with calculated compensation with circles and results from the second set with cubes.

Values of the two compensations correlate well up until 2 A electric current, after which the calculated compensation becomes slightly too large. The slight difference is not surprising since the calculated values are based on models and fittings. We can conclude that equation (8) seems to give reasonably accurate results.

3. Results and discussion

3.1. Static and dynamic yield stress

Deformations of the particle structures are different when measuring the MR fluid's dynamic or static yield stress. At low stress levels the particle structures only deform elastically, thus deformations will recover if the stress is removed. When the static yield stress is reached, the structures begin to slip on the plate surfaces or rupture. This can be seen in figure 13 as a sudden increase in shear rate. If the shear rate is increased further, the dynamic yield stress will be eventually reached. At this point the fluid is flowing and the particle structures are constantly breaking and reforming.

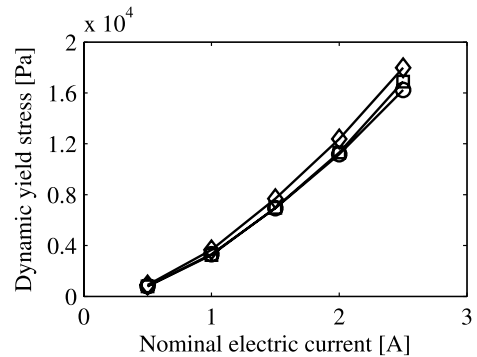


Figure 15. Dynamic yield stresses for smooth magnetic plates as originally measured (diamonds) and after calculated (circles) and manual (cubes) compensations.

3.2. Effect of the plate surface characteristics on yield stresses

The effect of the plate material and surface roughness on the measured static and dynamic yield stresses were studied with 0.5, 1.0, 1.5, 2.0 and 2.5 A electric currents. Measured yield stresses and relative differences between smooth and rough configurations are listed in tables 1 and 2, Magnetic flux densities in the tables are rheology-relevant average magnetic flux densities. The lowest values are measured with smooth non-magnetic plates, as expected. The plate surface roughness is smaller than the particle size, thus the normal forces pushing on the particles are not able to produce enough friction to prevent slippage on the surface [6]. Roughening of the surfaces increases values significantly; measured dynamic yield stresses are about 25% higher than with a smooth surface. The surface roughness is now larger than the particle size, effectively decreasing the slippage. Laun *et al* demonstrated via finite element simulations that the grooves and other defects on the non-magnetic surface will also form local increases in flux density that act as anchor points for the particles [5]. Roughly 12% higher values are measured with smooth magnetic rather than rough non-magnetic plates. Part of the difference could be caused by strong attractive forces between the surface and particles that are present with magnetic surfaces in addition to normal forces. However it should also be noted that since the average magnetic flux density is about 7% higher with magnetic plates it will also correspond for part of the increase. In fact after the difference in flux densities is compensated by subtracting the values of equation (8) from the measured values, as has been done in table 3, the difference almost disappears. This point out that here the higher values measured with magnetic plates seem to be mostly caused by differences in magnetic flux densities rather than by attractive forces between the particles and the surface. Roughening of the magnetic plates does not provide any significant increase in yield stress (typically less than 5%). The amount of the wall slip is already small to start with and roughening will not form similar anchor points as with non-magnetic plates to decrease it further [6].

Table 1. Measured static and dynamic yield stresses for non-magnetic plates.

\bar{B} (mT)	Static yield stress			Dynamic yield stress		
	Smooth (Pa)	Rough (Pa)	Relative difference (%)	Smooth (Pa)	Rough (Pa)	Relative difference (%)
70	807	860	6	633	794	22
142	3 184	3 678	14	2 629	3 436	27
213	5 789	7 027	19	5 193	6 719	26
285	9 110	10 761	17	8 296	10 559	24
357	12 175	13 947	14	11 513	14 932	26

Table 2. Measured static and dynamic yield stresses for magnetic plates.

\bar{B} (mT)	Static yield stress			Dynamic yield stress		
	Smooth (Pa)	Rough (Pa)	Relative difference (%)	Smooth (Pa)	Rough (Pa)	Relative difference (%)
75	1 066	1 129	6	907	886	2
150	3 691	3 969	7	3 567	3 729	4
227	7 982	8 202	3	7 605	7 480	2
304	11 827	12 263	4	11 484	11 996	4
380	17 055	17 412	2	18 120	17 597	3

Table 3. Static and dynamic yield stresses for magnetic plates where the effect of the higher magnetic flux density has been compensated.

\bar{B} (mT)	Static yield stress		Dynamic yield stress	
	Smooth (Pa)	Rough (Pa)	Smooth (Pa)	Rough (Pa)
70	953	1 011	804	786
142	3 297	3 552	3 164	3 307
213	7 132	7 341	6 745	6 634
285	10 567	10 975	10 185	10 639
357	15 237	15 583	16 071	15 607

The improved surface friction by roughening or by use of magnetic surfaces seems to have a greater impact on dynamic than on static yield stresses. In dynamic yield stress roughening for example typically provides relative increases of about 25% when the increase with static yield stresses is about 15%. This difference could be associated to different slippage mechanisms. When we are measuring the dynamic yield stress, the MR fluid is flowing. In the case of the smooth non-magnetic plates, the wall slip could be apparent, that is, there could be a layer of fluid on the plate surface that has a smaller concentration of particles than the rest of the fluid, effectively decreasing the measured values. Roughening may prevent the formation of such a layer, providing a significant increase in measured stresses. At no-flow conditions associated with static yield stress particles are in good contact with plates because of the gap-spanning particle structures, and the slippage will happen directly between particles and the surface. This has been called a true wall slip. In this case the friction with a smooth plate is probably higher to start with than when measuring dynamic yield stress, and the relative increase provided by the roughening therefore remains smaller.

3.3. Gap dependence of yield stress

The effect of the gap height was studied with 0.5, 1.5 and 2.5 A electric currents and 0.25, 0.50 and 1.00 mm gap heights. FEM simulations presented in section 2.4 show that the rheologically relevant average flux density in the gap increases about 4.5% when the gap height is raised by 0.25 mm. Calculations based on equation (8) show that this should lead to 5–6% increase in yield stress, which is a relatively small effect. The effect becomes more meaningful when the change is larger, since the yield stress increases exponentially with magnetic flux density. The increase should be approximately 17–21% when the gap height rises from 0.25 to 1.0 mm. Calculated values therefore show that the effect of the gap height can be significant and should be taken into account when comparing results.

In figure 16 the static yield stresses are as measured (solid line) and after subtracting the calculated increase caused by gap height change from the value (dashed line). The results for smooth non-magnetic plates are drawn with red diamonds, rough non-magnetic with green cubes, smooth magnetic with blue circles and rough magnetic with light blue crosses. Measured values do not show any significant gap dependence for non-magnetic plates, but for magnetic plates there is a clear increase in yield stress with increasing gap height. The increase is quite well in line with calculations, since after subtraction of the calculated increase the effect of the gap height almost disappears. Similar subtraction with non-magnetic surfaces leads to a decrease in yield stress with increasing gap height. Similar observations were done by de Vicente *et al* with smaller magnetic fields which they proposed could be caused by wall slip [4]. In our case at least some of the decrease might also be caused by a slight overshoot of the power law model mentioned in section 2.6. Therefore the subtracted increase, at least with 2.5 A electric current, is probably slightly too high. It is evident from

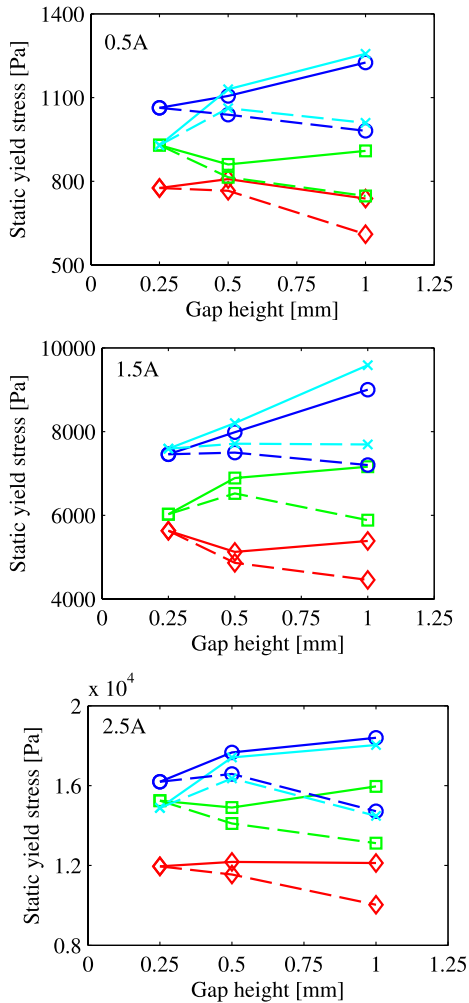


Figure 16. Static yield stresses as a function of the gap height with 0.5, 1.5 and 2.5 A electric currents measured with different types of measuring plates (red diamonds = smooth non-magnetic, green cubes = rough non-magnetic, blue circles = smooth magnetic, light blue crosses = rough magnetic). Solid lines present the measured values and dashed lines values after subtraction of the calculated increase.

section 3.2 that there is wall slip at least with the smooth non-magnetic plate. However, the behavior of the yield stress with increasing gap height is opposite to what is generally expected in the situations where the wall slip is present [2]. The phenomenon should be examined in more detail before further conclusions can be made.

Figure 17 show the dynamic yield stresses. All measured yield stresses increase with increasing gap height, which is opposite to what was previously observed by other authors [3, 4]. However, they used lower magnetic fields and/or smaller changes in gap height in which case the increase in yield stress due to changed magnetic flux density remains relatively small.

In fact, after subtraction of the calculated increases, the gap dependence mostly disappears. In some cases the yield stress seems to decrease with gap height, but this is probably mainly due to too high calculated values rather than the fluid's true behavior. Measurements therefore show that wall slip of MR fluids cannot be detected by comparison of flow curves, which is a common way to detect slippage with normal suspensions. The lack of the gap dependence could be explained by the MR fluid's flow behavior. Deformations may be concentrated at certain slip planes which are located at the weakest points of the system, whereas the rest of the fluid mainly remains intact. Slip planes may be at the plate–fluid interface or in the fluid, depending on plate properties. Therefore, the dynamic yield stress could be mainly dependent on forces acting between these slip planes rather than on the strength of the whole structure. In some situations MR fluid can also form distinct stripes in the flow direction where particle-rich and depleted layers alternate [1, 13]. Deformations are concentrated on the depleted layers while particle rich layers mainly remain unreformed and only slip past each other. However, this has been reported to happen at the high end of the shear rate range used in this study, thus it is not likely to be the dominant effect here [13].

4. Conclusions

Effects of the plate material, surface roughness and measuring gap height on static and dynamic yield stresses of an MR fluid were studied. Hall probe measurements and finite element simulations showed that the use of a magnetic plate or higher gap height increases the level of magnetic flux density and changes the shape of the radial flux density profile. Calculations based on these changes concluded that this can lead to over 20% increase in measured yield stress and has therefore be compensated when comparing the result. Calculated values were checked against measurement where a similar compensation was done by adjusting the electric current and fairly good agreement was found.

Roughening of the non-magnetic surfaces offered approximately a 25% increase in the dynamic and 15% increase in static yield stress. This difference could be associated to different slippage mechanisms; wall slip could be apparent when measuring dynamic yield stress and true with static yield stress because of the gap-spanning structures. Measured yield stresses were higher for smooth magnetic than smooth non-magnetic plates to start with, but roughening did not increase them further. The higher values measured with magnetic rather than rough non-magnetic plates seem to be mostly caused by differences in magnetic flux densities rather than by magnetic interactions between the particles and the surface.

It is obvious that there has to be slippage at the plate surfaces, at least with smooth non-magnetic plates, since the difference to yield stresses measured with rough plates is significant. Still the dynamic yield stresses generally remained independent of the gap height, after compensation for the magnetic flux density was applied. The wall slip cannot therefore be reliably detected with MR fluids by comparison

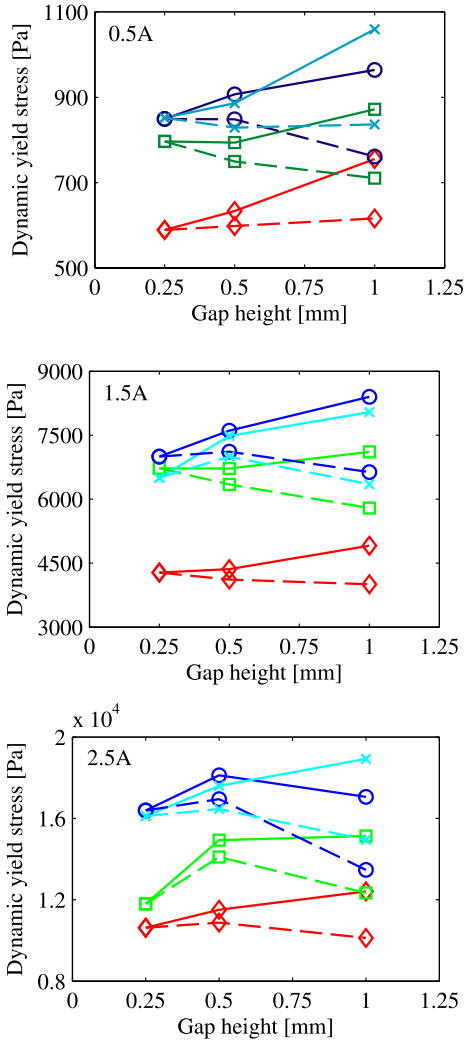


Figure 17. Dynamic yield stresses as a function of the gap height with 0.5, 1.5 and 2.5 A electric currents measured with different types of measuring plates (red diamonds = smooth non-magnetic, green cubes = rough non-magnetic, blue circles = smooth magnetic, light blue crosses = rough magnetic). Solid lines present the measured values and dashed lines values after subtraction of the calculated increase.

of flow curves measured at different gap heights, which is commonly used to detect slippage with normal suspensions.

Even though the relationship between the magnetic flux density and the shear stress of MR fluids is well known, the

seemingly small changes caused by different plate materials or gap heights are sometimes neglected [3, 4, 6]. These small differences can become meaningful, since the magnetic flux density and MR fluids' yield stresses are generally related by the power law function.

Acknowledgment

We thank Dr Lauger of Anton Paar GmbH for providing details of the MRD180/IT magneto-cell for flux density simulations.

References

- [1] Pfeil K, Graham M D and Klingenberg D J 2003 Structure evolution in electrorheological and magnetorheological suspensions from a continuum perspective *J. Appl. Phys.* **93** 5769–79
- [2] Yoshimura A and Prud'homme R K 1988 Wall slip corrections for couette and parallel disk viscometers *J. Rheol.* **32** 53–67
- [3] Lopes-Lopes T M, Rodrıguez-Arco L, Zubarev A and Dura'n J D G 2010 Effect of gap thickness on the viscoelasticity of magnetorheological fluids *J. Appl. Phys.* **108** 083503
- [4] de Vicente J, Lopes-Lopes T M, Dura'n J D G and Gonzalez-Caballero F 2004 Shear flow behavior of confined magnetorheological fluids at low magnetic field strengths *Rheol. Acta* **44** 94–103
- [5] Laun H M, Gabriel C and Kieburg C 2011 Wall material and roughness effects on transmittable shear stress of magnetorheological fluids in plate–plate magnetorheometry *Rheol. Acta* **50** 141–57
- [6] Lemaire E and Bossis G 1991 Yield stress and wall effects in magnetic colloidal suspensions *J. Phys. D: Appl. Phys.* **24** 1473–7
- [7] Laun H M, Schmidt G, Gabriel C and Kieburg C 2008 Reliable plate–plate MRF magnetorheometry based on validated radial magnetic flux density profile simulations *Rheol. Acta* **47** 1049–59
- [8] Carlson D J 2008 *Smart Materials* ed M Schwartz (Boca Ration, FL: CRC Press) chapter 17, p 17.4
- [9] Jonkkari I and Syrjala S 2010 Evaluation of techniques for measuring the yield stress of a magnetorheological fluid *Appl. Rheol.* **20** 45875
- [10] Kordonski W, Gorodkin S and Zhuravski N 2001 Static yield stress in magnetorheological fluid *Int. J. Mod. Phys.* **15** 1078–84
- [11] Ginder J M, Davis L C and Elie L D 1996 Rheology of magnetorheological fluids: models and measurements *Int. J. Mod. Phys. B* **10** 3293–303
- [12] Gec S and Phul P P 2002 Rheological properties of magnetorheological fluids *Smart Mater. Struct.* **11** 140–6
- [13] Volkova O, Cutilas S and Bossis G 1998 Shear banded flows and nematic-to-isotropic transition in ER and MR fluids *Phys. Rev. Lett.* **82** 233–6

Publication III


Ilari Jönkkäri, Matti Isakov and Seppo Syrjäla

**Sedimentation stability and rheological properties of ionic liquid-based
bidisperse magnetorheological fluids**

Journal of Intelligent Materials Systems and Structures 26(16) (2015) 2256-2265

© 2014 SAGE Publications
Reprinted with permission

Sedimentation stability and rheological properties of ionic liquid-based bidisperse magnetorheological fluids

Journal of Intelligent Material Systems and Structures
1–10
© The Author(s) 2014
Reprints and permissions:
sagepub.co.uk/journalsPermissions.nav
DOI: 10.1177/1045389X14551436
jim.sagepub.com


Ilari Jönkkäri, Matti Isakov and Seppo Syrjälä

Abstract

The sedimentation stability and rheological properties of ionic liquid-based magnetorheological fluids comprising a mixture of micron- and nano-sized particles were experimentally studied. Three different fluids with the same total particle concentration of 15 vol% were prepared for testing: one containing only microparticles and two others in which 5 or 10 wt% of the microparticles were replaced by nanoparticles. The nanoparticles were surface stabilized against oxidation. For comparison purposes, silicon oil-based magnetorheological fluids with similar solid fractions were also prepared and tested. The results indicate that, with ionic liquid as a carrier fluid, the addition of nanoparticles at 10 wt% reduces the sedimentation rate almost by an order of magnitude from that without nanoparticles, while the reduction in the dynamic yield stress is only marginal. The ionic liquid-based fluids also had a better dispersion of particles.

Keywords

Magnetorheology, ionic liquid, nanoparticles, sedimentation, yield stress

Introduction

Magnetorheological (MR) fluids are smart materials which show significant changes in rheological properties under magnetic field. They are suspensions of magnetic particles in a non-magnetic carrier fluid such as mineral or silicone oil (SO). The particles are typically spherical carbonyl iron particles 1–10 μm in diameter. Upon application of the magnetic field, the particles form chain structures in the direction of the magnetic field which hinders fluid flow. This so-called MR effect can be seen as a rise in fluid viscosity and appearance of distinct yield stress. The magnitude of the MR effect depends mainly on particle concentration and saturation magnetization of the particles (Bossis et al., 2002; Carlson and Jolly, 2000; De Vicente et al., 2011; Goncalves et al., 2006; Wang and Gordaninejad, 2008). Since the MR effect happens in a matter of milliseconds, fluid properties can be adjusted almost in real time. One of the main drawbacks of MR fluids is the tendency towards sedimentation. In this context, the sedimentation means that the particles settle to the bottom of the fluid over time due to gravitational forces unless the fluid is regularly mixed or under magnetic field. The remixing of the particles after the settling can be difficult because of the remnant magnetism that keeps them aggregated. Sedimentation of the particles is typically controlled with the use of thixotropic agents

and surfactants. These additives are materials like xanthan gum, silica gel, stearates and carboxylic acids that can form network structures in the fluid near no-flow conditions and increase the viscosity to nearly infinite. When the shear rate increases, the structures break down and the viscosity decreases (Carlson and Jolly, 2000). The more recent approaches to improve sedimentation stability involve the use of magnetic nanoparticles and ionic liquids (ILs).

Ferrofluids that are composed solely of magnetic nanoparticles (diameter <10 nm) do not settle due to the predominance of thermodynamic forces caused by thermal convection which can counteract gravitational forces. However, the yield stress of these fluids remains at a drastically lower level than in conventional MR fluids (Carlson and Jolly, 2000; Chaudhuri et al., 2005). Nanoparticles also need to be stabilized against irreversible aggregation. This is typically done by generating steric repulsion between particles with surfactants such as oleic acids (Chaudhuri et al., 2005; Tadmor et al., 2000). It is possible to maintain high level of MR effect

Tampere University of Technology, Tampere, Finland

Corresponding author:

Ilari Jönkkäri, Tampere University of Technology, Korkeakoulunkatu 6,
33101 Tampere, Finland.
Email: ilari.jonkkari@tut.fi

while reducing the rate of sedimentation by replacing only part of the micron-sized particles in MR fluid with nanoparticles (Chin et al., 2001; Ngatu and Wereley, 2007; Wereley et al., 2006). These fluids that contain both micro- and nanoparticles are called bidisperse MR fluids. The addition of small amounts of magnetic nanoparticles has been reported to increase the yield stress of a MR fluid (Chaudhuri et al., 2005; Chin et al., 2001; Wereley et al., 2006). This is believed to be caused by the smaller particles filling the voids between microparticles which locally enhance the magnetic field (Ngatu and Wereley, 2007). Wereley et al. (2006) prepared MR fluid samples composed of micron- and nano-sized iron particles with solid loading of 60 wt%. The concentration of nanoparticles varied between 2.5 and 30 wt% of the total particle loading. A significant improvement in the stability against sedimentation was found when more than 17.5 wt% of the particles were nano-sized. The addition of nanoparticles in small concentrations increased the yield stress. The yield stress was the highest with 7.5 wt% nanoparticle concentration after which it began to decrease, but was still slightly higher than in a MR fluid composed solely of micron-sized particles, when the nanoparticle concentration was around 20 wt%. In contrast, there are also studies in which the addition of nanoparticles resulted in a decrease in the yield stress (Ngatu and Wereley, 2007; Rosenfeld et al., 2002).

ILs are substances composed entirely of ions which are in liquid state at ambient temperature. They have a number of beneficial properties, such as low vapour pressure, non-flammability, high thermal stability and recyclability, which make them promising candidates as carrier fluids for MR fluids. ILs and magnetic particles have recently been studied in numerous articles (Dodbiba et al., 2008; Gómez-Ramírez et al., 2011, 2012; Guerrero-Sanchez et al., 2007, 2009; Huang and Wang, 2012; Oliveira et al., 2009; Rodríguez-Arco et al., 2011). ILs have offered both improved dispersion stability (Gómez-Ramírez et al., 2011; Guerrero-Sanchez et al., 2007; Oliveira et al., 2009) and decreased sedimentation rate (Guerrero-Sanchez et al., 2007) compared to conventional carriers.

Guerrero-Sanchez et al. (2007) were the first to propose the use of IL as a carrier fluid in MR fluids. They prepared MR fluid samples using eight different ILs and micron-sized iron oxide particles. One sample containing 1-butyl-3-methylimidazolium trifluoromethanesulfonate as IL showed an outstanding stability against sedimentation over a period of 1680 h. This was proposed to be related to the chemical characteristics of the IL as well as to its high affinity for the magnetic material. Not all ILs showed good characteristics. One MR sample was prepared by mixing IL and magnetite nanoparticles to study whether the IL could provide high enough colloidal stability to the nanoparticles so that no additional stabilization against aggregation

would be needed; however, this was not observed. Later, Oliveira et al. (2009) reported that they had prepared a ferrofluid based on IL and magnetic nanoparticles, which was stable without any stabilizing additive. This has recently been questioned since there are articles presenting that the electrostatic repulsion, which may exist between particles in IL, is not sufficient to prevent aggregation, and therefore, a strong steric repulsion is required to stabilize IL-based ferrofluids (Huang and Wang, 2012; Rodríguez-Arco et al., 2011).

Gómez-Ramírez et al. (2011) studied the stability and re-dispersibility of micron-sized carbonyl iron particles in ILs. Stability against aggregation as well as re-dispersibility was improved compared to samples with mineral oil as a carrier. The best results were achieved when 1-ethyl-3-methylimidazolium diethylphosphate was used as a carrier. Sedimentation, however, was faster in ILs than in mineral oil. It was proposed that the particle aggregates present in the mineral oil would slow down the sedimentation.

The aim of this work was to study whether the use of IL as a carrier could lead to an improvement in the dispersion and sedimentation stability of the bidisperse MR fluids. The sedimentation stability of the MR fluids was studied by optical tracking of the interface between the clear carrier fluid and the particle suspension that formed in the fluids over time. The MR response and viscosity of the fluids without magnetic field were measured with a rotational rheometer to reveal whether some properties were sacrificed when better sedimentation stability was attained. The viscosity of the fluids was compared with theoretical estimations to predict whether the particles were well dispersed in the carrier fluid.

Experimental

Preparation of MR fluids

A total of six MR fluids with different compositions were prepared for the analysis. Three fluids had SO (Rhodorsil 47 v 50) as a carrier fluid, and the rest were dispersed in 1-ethyl-3-methylimidazolium diethylphosphate IL (supplied by Merck). The IL was chosen based on earlier work by Gómez-Ramírez et al. (2011). They found that as a carrier fluid it provided high stability against aggregation. Viscosity of the SO was 48 ± 2.4 mPa s and the density 0.96 g/cm³ according to the manufacturer. Values for the IL were 317 ± 16 mPa s and 1.14 g/cm³, respectively. All MR fluids contained a total of 15 vol% magnetic particles. The particle concentration was kept low since sedimentation is typically faster with small particle concentrations (Ngatu and Wereley, 2007). The size distributions of the magnetic particles within a carrier fluid were different: one MR fluid had only micron-sized carbonyl iron particles (BASF, HQ) with mean particle size of

Table 1. Composition of MR fluids prepared for the analysis.

MR fluid no.	Size distribution of particles (total loading of 15 vol%)		Carrier fluid	Lecithin
	Micron-sized (wt%)	Nano-sized (wt%)		
1	100	0	Silicone oil	No
2	95	5	Silicone oil	Yes
3	90	10	Silicone oil	Yes
4	100	0	Ionic liquid	No
5	95	5	Ionic liquid	No
6	90	10	Ionic liquid	No

MR: magnetorheological.

2 μm , while in the two others, 5 or 10 wt% of the microparticles were replaced with nano-sized iron particles (Nanoiron, Nanofer Star). Nanoparticles were surface stabilized against oxidation with $\text{FeO-Fe}_3\text{O}_4$ double shell and had a mean particle size of 50 nm. The magnetization of both particles was measured as a function of the magnetic field with Quantum Design MPMS XL magnetic property measurement system at 27°C. As discussed earlier, the nanoparticles need also to be stabilized against aggregation. In total, 2 wt% of lecithin was added as a surfactant to the MR fluids which were composed of SO and nanoparticles. No additional stabilization was applied in IL-based MR fluids since some authors have speculated that the use of IL as a carrier fluid alone might provide an improved dispersion of particles (Gómez-Ramírez et al., 2011; Guerrero-Sanchez et al., 2007; Oliveira et al., 2009). Mixing of MR fluid components was done with a high-shear rate mixer at 2000 r/min. The container with MR fluid was held in ultrasonic bath while shearing to promote mixing and produce a more homogenized suspension. The mixing time for particles and the carrier fluid was 20 min. In cases in which lecithin was applied, the carrier fluid and lecithin were pre-mixed for 20 min before addition of the particles. The fluids were always remixed prior to the measurements. Table 1 tabulates the composition of the MR fluids.

Sedimentation measurements

The sedimentation behaviour of the test fluids was studied by optical tracking of the interface between the clear carrier fluid and the particle suspension that formed in the fluids over time after the mixing. Samples of 5 mL were poured into test tubes and held in a static fixture up to 800 h. A digital image was taken from the tubes every 60 min up to 800 h. The final image for the particle packing density determination was taken after 10,000 h. The images were converted to greyscale and analysed with MATLAB® software. Figure 1 presents an example of the pictures taken during the test. The boundary between the clear carrier fluid and the suspension could be numerically detected as a steep

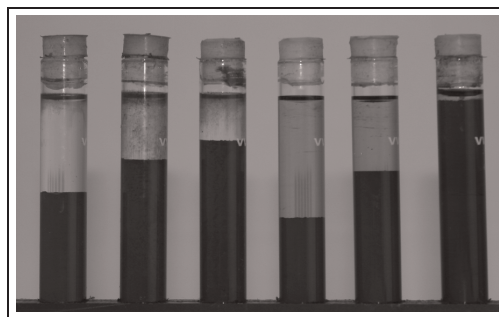


Figure 1. A clear boundary was formed between the clear carrier fluid and the suspension over time. The difference in sedimentation rate is distinct in the picture that was taken 100 h after the MR fluids were poured in.
MR: magnetorheological.

gradient in the greyscale values, when scanned along the vertical direction of the test tube as illustrated in Figure 2. The boundary motion could then be automatically tracked using a house-built MATLAB script.

Measurement of rheological properties

The rheological properties of the prepared MR fluid samples were measured with Anton Paar MCR 301 rotational rheometer. The measurements were conducted with magnetic field (on-state) and without magnetic field (off-state). Because without an applied magnetic field MR fluids are suspensions of relatively low viscosity, the concentric cylinder geometry was used for off-state rheological measurements. Owing to large shearing surface, this geometry offers good sensitivity when measuring low-viscosity materials. The CC17 geometry used consists of a rotating inner cylinder (bob) with a diameter D_c of 16.66 mm and a stationary outer cylinder (cup) with a diameter D_b of 18.08 mm as illustrated in Figure 3(a). Hence, the annular gap between the cylinders, where the fluid sample is confined, has a width of 0.71 mm. The stationary cylinder is made of aluminium, while the rotating

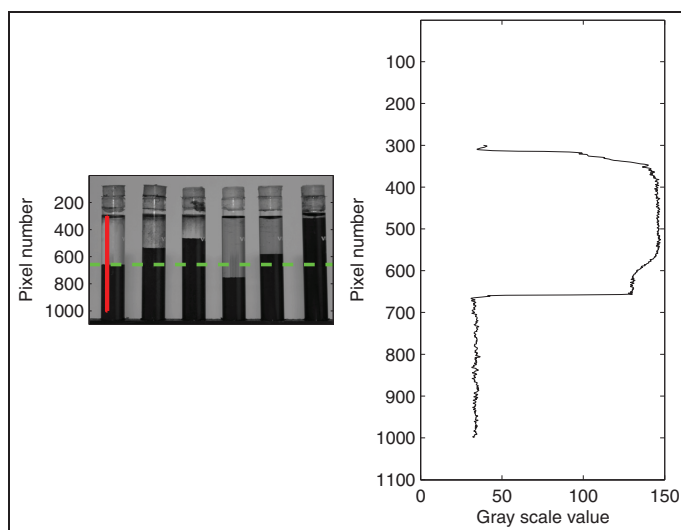


Figure 2. The MATLAB script detects the steep gradient in the greyscale values between the clear carrier fluid and the suspension (graph on the right side). In the figure, only the leftmost tube is analysed. The dashed line represents the level detected by the MATLAB script.

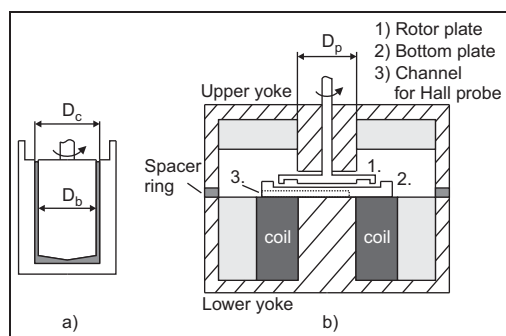


Figure 3. Schematics of (a) the CC17 concentric cylinder geometry and (b) MRD180/IT magneto-cell.

cylinder is made of stainless steel and has a rough surface to reduce slip, which is a typical source of error when suspensions are measured (Yoshimura and Prud'homme, 1988). During the measurement, the shear rate was first logarithmically increased in steps from 0.01 to 100 s^{-1} (up curve) and then decreased back to 0.01 s^{-1} (down curve). At each shear rate, the measuring time was predetermined so as to ensure reasonably steady values of viscosity and shear stress. In the on-state measurements, the rheometer was equipped with a MRD180/IT magneto-cell. The magneto-cell applies a plate–plate measuring geometry that consists of a stationary bottom plate and a rotating top plate. The fluid sample is placed in the gap

between the plates. Otherwise, the test procedure is similar to the one adopted in the off-state measurements. A schematic depiction of the magneto-cell is presented in Figure 3(b). Both bottom and top plates were custom-made from aluminium with a roughened surface and plate diameter D_p of 21 mm. The magneto-cell generates a vertical magnetic field that passes through the measuring gap. The strength of the field can be adjusted by changing the coil current inside the cell. Currents used here were 0.5, 1, 2, 3, 4 and 5 A, and the resulting magnetic flux density was measured with a Hall probe. It is well known that with this set-up, the radial magnetic flux density profile inside the measuring gap is not completely flat but peaks at the rim (Jönkkäri et al., 2012; Laun et al., 2008). In this article, the flux densities were measured from a channel underneath the measuring gap at 6 mm from the plate rim. More detailed information about the magneto-cell, custom geometries and the magnetic flux density profile can be found elsewhere (Jönkkäri et al., 2012). The temperature of the cell was held at 30°C during the measurements with a circulating water bath.

The influence of the composition of the MR fluid on the MR effect was evaluated by comparing the dynamic yield stresses of the fluids under various magnetic fields. The dynamic yield stress was evaluated from the flow curve that was measured by increasing the shear rate logarithmically from 0.001 to 100 s^{-1} and monitoring the resulting shear stress. The Bingham model was then fitted to the data to extrapolate the shear stress to a zero shear rate, which corresponds to the dynamic yield stress. The Bingham model is written as follows

$$\tau_R = \tau_y + \eta_p \dot{\gamma}_R \quad (1)$$

where τ_y is the yield stress and η_p the plastic viscosity

Results and discussion

Magnetic properties of the powders

The initial magnetization curves for the particles are presented in Figure 4. The external magnetic flux density is used on the x-axis instead of the magnetic field strength to facilitate better comparison with MR properties. It is evident from the figure that the saturation magnetization is smaller for the nanoparticles. The complete saturation of the particles happens around 2 T, where the (mass) magnetization is 18.36 Am²/kg for the nanoparticles and 22.69 Am²/kg for the microparticles. A gradual magnetic saturation, which is seen at the end of the linear portion of the curve, begins around 100 mT (6.07 Am²/kg) for the nanoparticles and 350 mT (13.33 Am²/kg) for the microparticles.

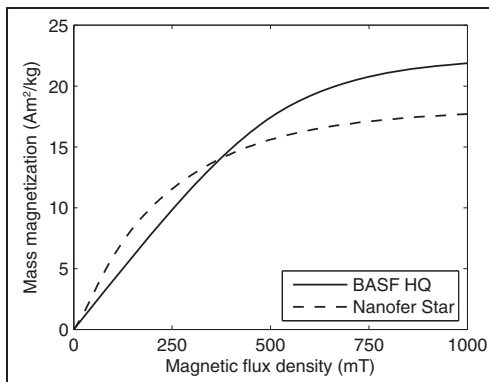


Figure 4. The magnetization curves for nanoparticles (broken line) and microparticles (solid line).

The inferior magnetic properties of the nanoparticles result likely from their smaller size and because part of the nano-sized iron is in oxide form that is known to have weaker magnetic properties than metallic iron.

Sedimentation of the particles

The results of the sedimentation experiments are presented in Figure 5. It depicts the location of the clear liquid–suspension interface as a function of time. The overall time of the experiment was 10,000 h, but the differences in the interface travel rate between the MR fluids were most significant at the beginning, and therefore, only the first 300 h are presented here. The behaviour of different SO-based MR fluids (see Figure 5(a)) is quite similar: the rate of the sedimentation decreases over time as the distance between particles diminishes causing more and more particle interactions. Both the addition of nanoparticles and the increase in nanoparticle concentration decrease the sedimentation rate. The decrease might be caused by the combined effect of the thermodynamic forces and increased frictional forces between the particles and the carrier fluid that reduce the settling rate. The frictional forces are greater with nanoparticles because the surface area of the nanoparticles per solid content is much higher than with microparticles. For the SO-based MR fluid 1 that contains only microparticles, the average sedimentation rate during the first 7.5-mm interface travel is 0.0548 $\mu\text{m/s}$, while for the fluid having 10% of nanoparticles the rate is 0.0254 $\mu\text{m/s}$. The improvement is modest.

The sedimentation behaviour of the IL-based MR fluids (see Figure 5(b)) is quite different from the SO-based fluids. The interface travel rate is initially small for MR fluid 4, which contains only microparticles, but the rate increases over the first 15–20 h and eventually becomes much higher than in SO. The rate decreases over time as the distance between particles becomes smaller. The faster sedimentation in IL is rather

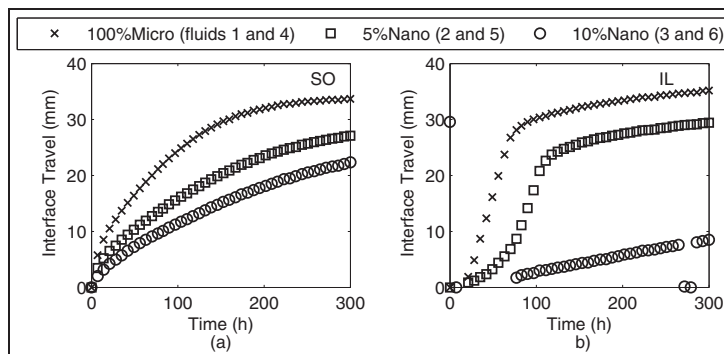


Figure 5. Sedimentation curves for the (a) SO- and (b) IL-based MR fluids.
SO: silicone oil; IL: ionic liquid.

surprising if only the viscosity of the carrier fluid is considered. Viscosity is related to the shear forces induced by the carrier fluid on the particles that resist gravitational forces during sedimentation. Since the viscosity of IL is about six times that of SO, the sedimentation rate should be slower. The same phenomenon was observed by Gómez-Ramírez et al. (2011) when using IL and mineral oil as carrier fluids. It was proposed that there are more and larger particle aggregates in the mineral oil which reduce the sedimentation rate. As shown in Figure 5(b), the addition of 5% nanoparticles extends the slow sedimentation phase at the beginning of the experiment. The rate still increases gradually and becomes similar to that of the MR fluid 4 after about 45 h. The increase in the nanoparticle concentration from 5% to 10% changes the sedimentation behaviour drastically; the low sedimentation rate remains low over time. The average sedimentation rate for the MR fluid 6 is about $0.008 \mu\text{m/s}$. This is almost an order-of-magnitude improvement compared to the MR fluid 4 which has a mean sedimentation rate of $0.063 \mu\text{m/s}$ during the first 7.5-mm interface travel. Ngatu and Wereley (2007) determined a sedimentation rate of $0.0058 \mu\text{m/s}$ for their MR fluid, having total iron particle loading of 70 wt% with 10% nanoparticle concentration. Our results are thus in good agreement with theirs especially when taking into account that the sedimentation is typically slower with higher particle loadings.

The dispersion of the particles was estimated by calculating the particle packing density for the MR fluids at the end of the sedimentation experiment. The particle packing density should be higher for fluids with well-dispersed particles since individual spheres can pack more tightly than arbitrary agglomerates. Table 2 tabulates particle packing densities that were determined at 10,000 h using equation (2)

$$\varphi = \frac{\phi h_0}{h_e} \quad (2)$$

where φ is the particle packing density, ϕ is the volume fraction of the particles, h_0 is the initial height of the suspension in the tube and h_e is the height of the sediment layer after 10,000 h.

Based on Table 2, higher packing densities are obtained when the carrier fluid is IL. The difference in packing density between the carrier fluids could be partly explained by the lecithin that was added to some of the SO-based MR fluids. Since the lecithin generates steric repulsion between the nanoparticles thus preventing irreversible aggregation, it is also likely to increase the inter-particle distance of the microparticles, resulting in looser packing. The lecithin, however, cannot explain the large difference which is observed between the SO- and IL-based MR fluids containing only microparticles. This suggests that there are more particle

Table 2. Particle packing densities for MR fluids after 10,000 h.

MR fluid no.	Size distribution of magnetic particles		Particle packing density
	Micron-sized (wt%)	Nano-sized (wt%)	
1	100	0	0.31
2	95	5	0.28
3	90	10	0.26
4	100	0	0.46
5	95	5	0.39
6	90	10	0.35

MR: magnetorheological.

aggregates in the SO-based fluids. The particle aggregation could explain why nanoparticles do not reduce the sedimentation rate as effectively in SO as in IL. If the nanoparticles are well dispersed in the carrier fluid, the combined effect of the thermodynamic forces and greater internal frictional forces reduces the settling rate of a single nanoparticle effectively. In contrast, if the nanoparticles are in the fluid as micron-sized aggregates, the effect probably remains at a drastically lower level.

Off-state rheological properties

The carrier fluids behave in a Newtonian manner, as expected. The measured viscosities were 45 and 304 mPa s for the SO and IL, respectively. These values agree well with the values given by the manufacturer (48 ± 2.4 mPa s for SO and 317 ± 16 mPa s for IL). The addition of lecithin increases the viscosity of the SO by about 2 mPa s.

The viscosity curves for MR fluids are presented in Figure 6. When particles are added to the carrier fluid, the behaviour changes to non-Newtonian; all MR fluids show shear-thinning behaviour. Shear thinning is typically present in concentrated suspensions where it is caused by particle–particle interactions. It can also be related to the existence of particle aggregates in the fluid: particle structures that have one or two dimensions larger than the others can orient themselves in the direction of the flow, or the particle structures can break up to smaller clusters. Both phenomena lead to a decrease in viscosity. The viscosity model by Qi and Tanner (2011), which is suitable for both mono- and bidisperse suspensions, was used in this study in order to calculate the relative viscosities of the suspensions

$$\eta_r = \left[\left(1 - \frac{\varphi_l}{1 - c_l \varphi_l} \right) \left(1 - \frac{\varphi_s}{1 - c_s \varphi_s} \right) \right]^{-\frac{5}{2}} \quad (3)$$

where η_r is the relative viscosity of the suspension and φ_l and φ_s are the volume fractions of the large and small particles, respectively. The parameters c_l and c_s

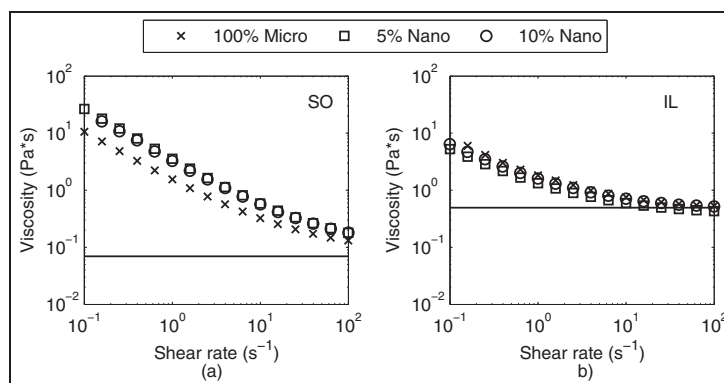


Figure 6. Viscosity curves for (a) SO- and (b) IL-based MR fluids without magnetic field.

SO: silicone oil; IL: ionic liquid.

Solid lines represent the estimate and symbols for the measured data.

depend on the particle size ratio, random close packing densities and so on and are presented in more detail elsewhere (Qi and Tanner, 2011). The model is a modified version of the earlier model for monodisperse fluids by Mendoza and Santamaria-Holek (2009). The relative viscosities for the MR fluids given by the model are 1.5644 (microparticles), 1.5526 (5% nanoparticles) and 1.5422 (10% nanoparticles). It has been shown by Ward and Whitmore (1950) that suspensions composed mainly of large particles and a few small particles show a decrease in viscosity when compared to suspensions of only large particles. It was proposed that smaller particles fill the empty spaces between the larger particles and generate a lubricating effect that reduces particle impacts (Ward and Whitmore, 1950). The relative viscosity is the ratio of the viscosity of the suspension η_s to the viscosity of the carrier fluid η_0 . Theoretical viscosities for the MR fluids can, therefore, be estimated as

$$\eta_s = \eta_0 \eta_r \quad (4)$$

The theoretical viscosities calculated by equation (4) are shown in Figure 6(a) and (b) for the 5% nanoparticle concentration only since the differences in predicted viscosities between different concentrations are too small to be seen on the logarithmic scale. As Figure 6(b) depicts, the viscosity of the IL-based MR fluid 4 that contains only microparticles levels off with increasing shear rate, and the estimation based on equation (3) becomes valid near 100 s^{-1} . In contrast, the SO-based MR fluids presented in Figure 6(a) show continued shear thinning at 100 s^{-1} , and equation (3) underestimates the viscosities. Both the deviation of the measured viscosities from the estimate and the stronger shear thinning suggest that the SO-based fluids have more particle aggregates. In IL-based fluids, the change in viscosity due to nanoparticle addition was smaller

than the variance of the results. The changes predicted by the model are, in fact, so small that it is quite probable that they remain undetected, as implied by the results. In SO-based fluids, the addition of nanoparticles always leads to increase in viscosity, which is in contradiction to the theory. A possible reason is that the nanoparticles are not fully dispersed in SO and remain in the fluid as micron-sized aggregates. In general, the off-state measurements show that it is easier to achieve good dispersion of particles in IL than in SO.

On-state rheological properties

On-state rheological properties were measured with 0.5, 1, 2, 3, 4 and 5 A coil currents that resulted in 70, 144, 288, 427, 550 and 642 mT flux densities, respectively. The yield stresses were determined from the shear stress versus shear rate flow curves with a Bingham model as illustrated in Figure 7 for MR fluid 4.

The yield stresses of the MR fluids are presented in Figures 8 to 10. The values are averages of two measurements, and the error bars illustrate the standard errors of the results. All MR fluids behaved as expected; yield stresses increased with magnetic flux density. As illustrated by Figure 8, the yield stresses of the IL-based MR fluid 4 were 4%–13% higher compared to SO-based MR fluid 1. However, it should be noted that the difference is within the standard error at higher flux densities. It is known that the carrier fluid influences the yield stress of a MR fluid (Carlson, 2005; López-López et al., 2008). This may be related to the affinity between the carrier fluid and the particles; when the affinity is high, the particles are in the fluid as individual particles. These particles can form regular chain structures that have high packing density under magnetic field, whereas particle aggregates form more irregular structures. The effect of the particle dispersion on

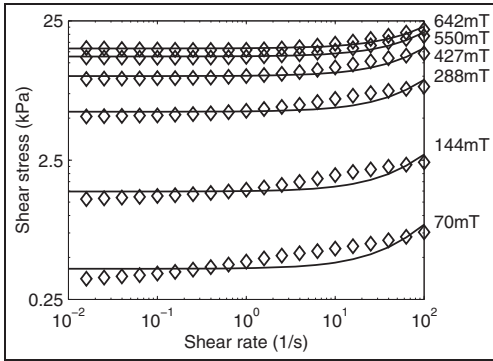


Figure 7. Determination of the yield stresses from the MR fluid 4 flow curves by using the Bingham model. MR: magnetorheological. Solid lines represent Bingham model and symbols represent measured data.

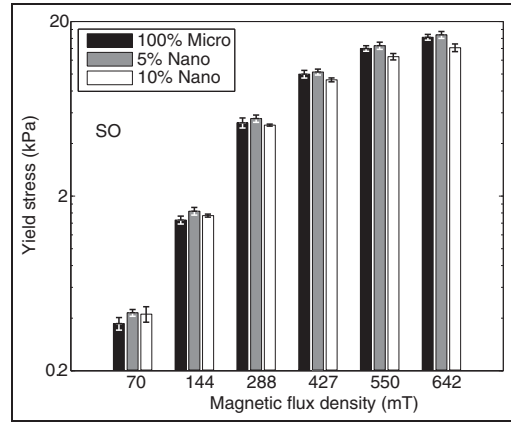


Figure 9. Yield stresses for the SO-based MR fluid as a function of magnetic flux density. SO: silicone oil; MR: magnetorheological.

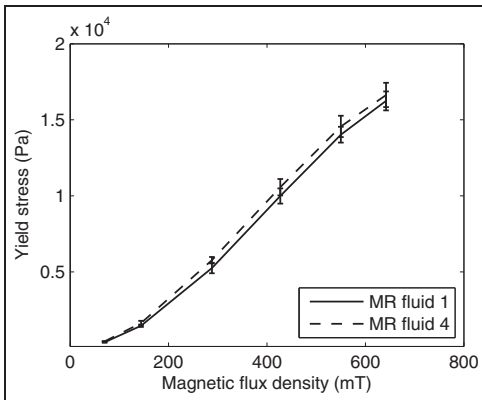


Figure 8. The yield stress as a function of magnetic flux density for the SO- (solid line) and IL-based (broken line) MR fluids that contain only microparticles. SO: silicone oil; MR: magnetorheological; IL: ionic liquid.

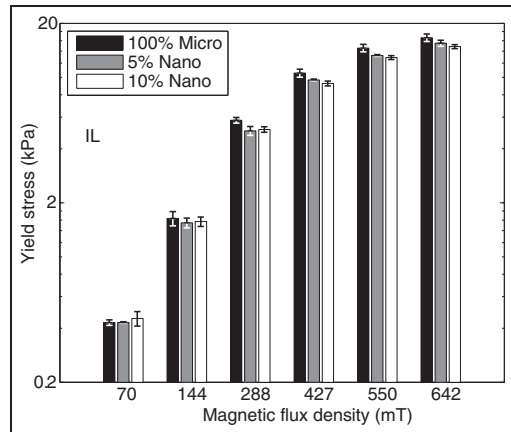


Figure 10. Yield stresses for the IL-based MR fluid as a function of magnetic flux density. IL: ionic liquid; MR: magnetorheological.

MR properties has been studied in more detail by López-López et al. (2008). They reached a general conclusion that well-dispersed MR fluids carry slightly higher dynamic yield stresses than ill-dispersed fluids.

The effect of the nanoparticles on the yield stress of MR fluids is presented in Figures 9 and 10. The yield stress increased by 3%–13% in SO-based fluid when 5% of the microparticles were replaced with nanoparticles. The increase was higher with small flux densities and diminished as the magnetic field grew stronger. The increase in nanoparticle concentration to 10% resulted in 12% increase in yield stress with the smallest flux density compared to MR fluid 1 that contained only microparticles. The initial increase turned to a decrease when the flux density exceeded 144 mT, and

the yield stress at the highest flux density was about 15% below the value that was measured for the MR fluid 1. The measured yield stresses agree qualitatively with the magnetization behaviour of the particles presented in Figure 4 (see section ‘Magnetic properties of the powders’). The slope of the linear portion of the magnetization curve is initially steeper for nanoparticles, which corresponds to the higher initial growth rate in yield stress for the MR fluids 2 and 3 compared to MR fluid 1. However, the gradual magnetic saturation of the nanoparticles begins already at small magnetic flux densities, and therefore, the growth rate decreases as the flux density increases. In IL-based fluids, an increase in yield stress due to particle loading was only

observed with MR fluid 6 at the smallest flux density. The increase in nanoparticle concentration from 5% to 10% resulted in only minor changes in the properties of the MR fluids, that is, the decrease in yield stress was slightly higher under highest flux densities. Earlier studies have reported both an increase (Chaudhuri et al., 2005; Chin et al., 2001; Wereley et al., 2006) and a decrease (Ngatu and Wereley, 2007; Rosenfeld et al., 2002) in the yield stress of MR fluids when part of the microparticles is replaced by nanoparticles. The increase has been explained by smaller particles filling the empty spaces between microparticles, which locally raise the magnetic permeability of the carrier fluid and results in higher magnetic flux density (Ngatu and Wereley, 2007). Since the magnetic properties of the nanoparticles are generally inferior when compared to microparticles, the rise in concentration eventually leads to a decrease in yield stress. Therefore, there is an optimum nanoparticle concentration with which the highest yield stress is reached. The optimum seems to depend at least on total particle concentration: Chaudhuri et al. (2005) reached highest yield stresses with 5% nanoparticle concentration when total particle loading was 45 wt%, whereas Wereley et al. (2006) measured highest yield stresses with 7.5% concentrations of 60 wt% particle loading. Based on our results, it seems that the dispersion of particles may also play a role in the optimum concentration, but a comprehensive study on the dispersion of the nanoparticles is needed before further conclusions can be made.

Conclusion

In this work, we have experimentally studied the effect of the carrier fluid on the sedimentation stability, MR response and off-state viscosity of MR fluids. A total of six MR fluid samples were prepared with total particle concentration of 15 vol% and SO or IL as a carrier fluid. One of the samples of both carrier fluids contained only microparticles, whereas in others 5% or 10% of the particles were nano-sized.

The sedimentation rate was greatly reduced in IL-based MR fluid when 10% of the microparticles were replaced with nanoparticles. In contrast, only a small reduction was observed in SO-based fluid with similar particle fractions. A better dispersion of nanoparticles in IL was proposed as a plausible reason for the difference in behaviour. The packing density of the particles at the end of the sedimentation experiment was calculated in order to estimate the dispersion of the particles. The density was lower in SO-based fluids, which suggests that there are more particle aggregates. The viscosity measurements without the magnetic field support the observation since the shear thinning of the SO-based fluids was stronger and the measured viscosities deviated from the level that was estimated with the

equation by Qi and Tanner (2011). At higher shear rates, the measured viscosities of the IL-based MR fluids seemed to level off to a Newtonian plateau, in which the measured values for the MR fluid that contained only microparticles correlated well with the estimate. This suggests that the particles were well dispersed. It can be concluded from the sedimentation and viscosity measurements that a better dispersion of the particles is always reached in IL when the same mixing procedure is used.

Finally, the effect of the carrier fluid and nanoparticles on MR response was investigated by comparing the dynamic yield stresses at different magnetic flux densities. The yield stresses were 4%–13% higher in the IL-based MR fluid when only microparticles were used. A general observation that slightly higher dynamic yield is generated in well-dispersed MR fluids has also been made in earlier studies. The yield stresses increased 3%–13% in SO-based fluid when 5% of the particles were nano-sized, but an increase in nanoparticle concentration led to the reduction in the yield stress at higher magnetic flux densities. This was likely due to inferior magnetic properties of the nanoparticles compared to microparticles that led to gradual magnetic saturation already at low magnetic flux densities. In the case of the IL-based MR fluids, the yield stresses were almost always smaller with fluids that contained nanoparticles.

As a summary, it was shown that IL can be used as a carrier fluid with nano- and microparticles in order to produce a MR fluid that has significantly improved sedimentation stability. Furthermore, the magnetic field-induced yield stress of the MR fluid suffered only a small reduction compared to a MR fluid that contains only micron-sized particles.

Acknowledgements

We thank Dr H Huhtinen (University of Turku) for measuring the magnetic properties of the particles.

Declaration of conflicting interests

The authors declared no potential conflicts of interest with respect to the research, authorship and/or publication of this article.

Funding

This research received no specific grant from any funding agency in the public, commercial or not-for-profit sectors.

References

- Bossis G, Volkova O, Laci S, et al. (2002) Magnetorheology: fluids, structures and rheology. *Lecture Notes in Physics* 594: 202–230.
- Carlson JD (2005) MR fluids and devices in real world. *International Journal of Modern Physics B: Condensed Matter Physics, Statistical Physics, Applied Physics* 19: 1463–1470.

- Carlson JD and Jolly MR (2000) MR fluid, foam and elastomer devices. *Mechatronics* 10: 555–569.
- Chaudhuri A, Wang G and Wereley NM (2005) Substitution of micron by nanometer scale powders in magnetorheological fluids. *International Journal of Modern Physics B: Condensed Matter Physics, Statistical Physics, Applied Physics* 19: 1374–1380.
- Chin BD, Park JH, Kwon MH, et al. (2001) Rheological properties and dispersion stability of magnetorheological (MR) suspensions. *Rheologica Acta* 40: 211–219.
- De Vicente J, Klingenberg DJ and Hidalgo-Alvarez R (2011) Magnetorheological fluids: a review. *Soft Matter* 7: 3701–3710.
- Dodbiba G, Park HS, Okaya K, et al. (2008) Investigating magnetorheological properties of mixture of two types of carbonyl iron powders suspended in an ionic liquid. *Journal of Magnetism and Magnetic Materials* 320: 1322–1327.
- Gómez-Ramírez A, López-López MT, González-Caballero F, et al. (2011) Stability of magnetorheological fluids in ionic liquids. *Smart Materials and Structures* 20: 045001
- Gómez-Ramírez A, López-López MT, González-Caballero F, et al. (2012) Wall slip phenomena in concentrated ionic liquid-based magnetorheological fluids. *Rheologica Acta* 51: 793–803.
- Goncalves FD, Koo J-H and Ahmadian M (2006) A review of the state of the art in magnetorheological fluid technologies – part I: MR fluid and MR fluid models. *Shock and Vibration Digest* 38: 203–219.
- Guerrero-Sanchez C, Lara-Ceniceros T, Jimenez-Regalado E, et al. (2007) Magnetorheological fluids based on ionic liquids. *Advanced Materials* 19: 1740–1747.
- Guerrero-Sanchez C, Ortiz-Alvarado A and Schubert US (2009) Temperature effect on the magneto-rheological behavior of magnetite particles dispersed in an ionic liquid. *Journal of Physics: Conference Series* 149: 012052
- Huang W and Wang X (2012) Study on the properties and stability of ionic liquid-based ferrofluid. *Colloid and Polymer Science* 290: 1695–1702.
- Jönkkäri I, Kostamo E, Kostamo J, et al. (2012) Effect of the plate surface characteristics and gap height on yield stress of a magnetorheological fluid. *Smart Materials and Structures* 21: 075030
- Laun HM, Schmidt G, Gabriel C, et al. (2008) Reliable plate–plate MRF magnetorheometry based on validated radial magnetic flux density profile simulations. *Rheologica Acta* 47: 1049–1059.
- López-López MT, Kuzhir P, Bossis G, et al. (2008) Preparation of well dispersed magnetorheological fluids and effect of dispersion on their magnetorheological properties. *Rheologica Acta* 47: 787–796.
- Mendoza CI and Santamaria-Holek I (2009) The rheology of hard sphere suspensions at arbitrary volume fractions: an improved differential viscosity model. *Journal of Chemical Physics* 130: 044904.
- Ngatu GT and Wereley NM (2007) Viscometric and sedimentation characterization of bidisperse magnetorheological fluids. *IEEE Transactions on Magnetics* 43: 2474–2476.
- Oliveira FCC, Rossi LM, Jardim F, et al. (2009) Magnetic fluid based on γ -Fe₂O₃ and CoFe₂O₄ nanoparticles dispersed in ionic liquids. *Journal of Physical Chemistry C* 113: 8566–8572.
- Qi F and Tanner RI (2011) Relative viscosity of bimodal suspensions. *Korea-Australia Rheology Journal* 23: 105–111.
- Rodríguez-Arco L, López-López MT, González-Caballero F, et al. (2011) Steric repulsion as a way to achieve the required stability for the preparation of ionic liquid-based ferrofluids. *Journal of Colloid and Interface Science* 357: 252–254.
- Rosenfeld N, Wereley NM, Radhakrishnan R, et al. (2002) Behavior of magnetorheological fluids utilizing nanopowder iron. *International Journal of Modern Physics B: Condensed Matter Physics, Statistical Physics, Applied Physics* 16: 2392–2398.
- Tadmor R, Rosenweig RE, Frey J, et al. (2000) Resolving the puzzle of ferrofluid dispersants. *Langmuir* 16: 9117–9120.
- Wang X and Gordaninejad F (2008) Magnetorheological materials and their applications. In: Shahinpoor M and Schneider H-J (eds) *Intelligent Materials*. Cambridge: RSC Publishing, pp. 339–385.
- Ward SG and Whitmore RL (1950) Studies of the viscosity and sedimentation of suspensions Part I – the viscosity of suspension of spherical particles. *British Journal of Applied Physics* 1: 286
- Wereley NM, Chaudhuri A, Yoo JH, et al. (2006) Bidisperse magnetorheological fluids using Fe particles at nanometer and micron scale. *Journal of Intelligent Materials Systems and Structures* 17: 393–401.
- Yoshimura A and Prud'homme RK (1988) Wall slip corrections for Couette and parallel disk viscometers. *Journal of Rheology* 32: 53–67.

Publication IV

Ilari Jönkkäri, Miika Sorvali, Hannu Huhtinen, Essi Sarlin, Turkka Salminen, Janne Haapanen, Jyrki Mäkelä and Jyrki Vuorinen

Characterization of Bidisperse Magnetorheological Fluids Utilizing Maghemite ($\gamma - \text{Fe}_2\text{O}_3$) Nanoparticles Synthesized by Flame Spray Pyrolysis

Journal of Smart Materials and Structures 26(9) (2017) 095004

© 2017 IOP Publishing
Reprinted with permission

Characterization of bidisperse magnetorheological fluids utilizing maghemite ($\gamma\text{-Fe}_2\text{O}_3$) nanoparticles synthesized by flame spray pyrolysis

I Jönkkäri¹, M Sorvali², H Huhtinen³, E Sarlin¹, T Salminen⁴, J Haapanen², J M Mäkelä² and J Vuorinen¹

¹Laboratory of Materials Science, Tampere University of Technology, PO Box 589, FI-33101 Tampere, Finland

²Aerosol Physics Laboratory, Laboratory of Physics, Tampere University of Technology, PO Box 692, FI-33101 Tampere, Finland

³Wihuri Physical Laboratory, Department of Physics and Astronomy, University of Turku, FI-20014 Turku, Finland

⁴Optoelectronics Research Centre, Tampere University of Technology, FI-33720 Tampere, Finland

E-mail: ilari.jonkkari@tut.fi

Received 21 April 2017, revised 19 June 2017

Accepted for publication 13 July 2017

Published 9 August 2017



CrossMark

Abstract

In this study we have used liquid flame spray (LFS) process to synthesize $\gamma\text{-Fe}_2\text{O}_3$ nanoparticles of two different average sizes. Different sized nanoparticles were generated with two different liquid precursor feed rates in the spray process, higher feed rate resulting in larger nanoparticles with higher saturation magnetization. The nanoparticles were used in bidisperse magnetorheological fluids to substitute 5% of the micron sized carbonyl iron particles. To our knowledge this is the first time particles synthesized by the LFS method have been used in magnetorheological fluids. The bidisperse fluids showed significantly improved sedimentation stability compared to a monodisperse suspension with the same solid concentration. The tradeoff was an increased viscosity without magnetic field. The effect of the nanoparticles on the rheological properties under external magnetic field was modest. Finally, the dynamic oscillatory testing was used to evaluate the structural changes in the fluids under magnetic field. The addition of nanoparticles decreased the elastic portion of the deformation and increased the viscous portion.

Keywords: magnetorheology, maghemite, bidisperse, flame spray pyrolysis, nanoparticle, sedimentation

(Some figures may appear in colour only in the online journal)

1. Introduction

Magnetorheological (MR) fluids are so-called smart materials that change their properties by external stimuli. With MR fluids the stimulus is an external magnetic field that induces a reversible transition from liquid- to solid-like behavior. The MR fluids are generally composed of spherical magnetic particles that are suspended in non-magnetic carrier fluid.

When the MR fluid is exposed to an external magnetic field, the particles form columnar structures in the direction of the field lines that resist the flow [1–3]. Since the carrier fluid and the particles have a large density mismatch, the particles tend to descend in the fluid over time. This sedimentation is problematic, since it can reduce the MR response, that is the change in rheological properties by magnetic field, or even prevent it completely. The redispersion of the particles may

also be difficult after sedimentation if they form a hard cake at the bottom. There are several ways how the sedimentation may be hindered. A conventional way is the usage of surfactants and thixotropic agents. Thixotropic agents function by forming structures in the carrier fluid at small shear rates that increase fluids viscosity and slow down the sedimentation. The structures break down when the shear rate increases. The surfactants function by steric repulsion. They are typically short molecule chains that can adhere on the particle surface from one end while the other is stretching out and preventing a direct contact with neighboring particles [4]. A more recent approach to reduce sedimentation is the usage of nanoparticles.

Suspensions that contain only well dispersed nanoparticles do not settle at all; thermal convection in the fluid creates thermodynamic forces that counteract gravitational forces causing the sedimentation. Ferrofluids that contain magnetic nanoparticles, surfactant and carrier fluid are stable against agglomeration and sedimentation, but have significantly lower MR response than conventional MR fluids with micron-sized particles [2, 5]. It has been shown in number of studies that addition of a low amount of nanoparticles with larger particles may reduce the sedimentation rate of the whole suspension without sacrificing the MR response [5–13]. When the nanoparticle concentration is kept small, the MR response remains at a satisfactory level or may even improve [6–9]. The nanoparticles in these so-called bidisperse fluids have most often been magnetite (Fe_3O_4) due to its availability, well known synthesis and magnetic properties [5, 10–13]. Another magnetic iron oxide is the maghemite ($\gamma\text{-Fe}_2\text{O}_3$) which has quite similar magnetic properties to Fe_3O_4 . Both have an inverse spinel structure, but $\gamma\text{-Fe}_2\text{O}_3$ has only Fe^{3+} iron cations whereas Fe_3O_4 has both Fe^{3+} and Fe^{2+} . Also, $\gamma\text{-Fe}_2\text{O}_3$ has a better chemical stability than Fe_3O_4 and is more versatile as the particle morphologies may vary from spheres to ellipsoids over a wide size range from 2 to 1000 nm depending on how the particle is synthesized [14].

In the literature several synthesis routes both in liquid and gas phase have been presented. Thermal aerosol techniques offer a potential to generate spherical nanoparticles via a dry industrial process [15] and especially flame methods are considered optional for up-scaling [16]. The particles synthesized with these techniques tend to form aggregates, which are primary particles fused together with strong chemical or sintering forces [17]. In flame spray pyrolysis (FSP) liquid precursors are sprayed into the flame. In a specific FSP-method, liquid flame spray (LFS), hydrogen and oxygen act as atomizing and combustion gases [18]. Major advantage of the LFS process is the broad spectrum of metal or metal oxide nanoparticles, which can be created using different liquid precursors. The method is suitable for one- or multi-component nanoparticle synthesis [19]. Injected metal salt or organometallic precursor evaporates in the flame: the evaporated precursor molecules can react chemically or decompose thermally, then nucleate and re-condense into nanoparticle form of the final material [20].

In the present study we use $\gamma\text{-Fe}_2\text{O}_3$ nanoparticles, synthesized by LFS process, together with micron-sized carbonyl iron (CI) particles to prepare bidisperse MR fluids with improved sedimentation stability. The nanoparticles were characterized by transmission electron microscopy (TEM), x-ray diffraction (XRD), Raman spectroscopy and SQUID magnetometry. The sedimentation stability of the MR fluids was studied by optical tracking of the interface between the clear carrier fluid and the particle suspension that formed in the fluids over time. The rheological characteristics of the fluids were examined with (on-state) and without magnetic field (off-state) via rotational rheometer.

2. Experimental

2.1. Materials

Three MR fluids were prepared with a total particle volume concentration ϕ of 0.15. One MR fluid was monodisperse containing only micron-sized CI particles (BASF, HQ) while in the others 5% of the total particle concentration was substituted with $\gamma\text{-Fe}_2\text{O}_3$ particles. The fraction of the nanoparticles was kept low since the fluids became too thick with higher concentrations. The substitution was done based on the volume fractions since the magnitude of the magnetorheological effect depends on the volume concentration of the magnetic particles [21]. Rhodorsil 47 v 50 silicone oil was used in all MR fluids as the carrier fluid. It has a viscosity of 48 ± 2.4 mPa s and a density of 0.96 g cm^{-3} . Two weight percent of lecithin was added to all MR fluids, since the magnetic nanoparticles need stabilization against agglomeration, as they possess a permanent magnetic moment. The lecithin has been used as a surfactant to improve dispersion stability of similar type of magnetic nanoparticles in silicone oil before [7]. The lecithin was added also into the MR fluid without nanoparticles to make sure that it is not causing the differences in sedimentation behavior and rheological properties between mono- and bidisperse fluids.

2.2. Synthesis of $\gamma\text{-Fe}_2\text{O}_3$ nanoparticles

The $\gamma\text{-Fe}_2\text{O}_3$ nanoparticles were synthesized by LFS-method where hydrogen and oxygen act as atomizing and combustion gases. Gas flow rates in the flame for hydrogen and oxygen were 40 l min^{-1} and 20 l min^{-1} , respectively. The precursor for the Fe_2O_3 was ferrocene ($\text{Fe}(\text{C}_5\text{H}_5)_2$, Alfa Aesar 99%) dissolved in xylene (VWR, technical grade), with metallic concentration of 29 mg(Fe)/ml. Ferrocene was chosen as the precursor compound since it has relatively high volatility and therefore it is not expected to produce undesired hematite residual particles, which would decrease the magnetic properties of the iron oxide nanopowder. Precursor feed rates were 3.0 and 8.3 ml min^{-1} for samples Nano1 and Nano2 respectively. The aerosol nanoparticles were collected from the gas flow by a simple planar electrostatic precipitator (ESP) placed downstream of the flame. In the ESP, there are two steel plates with a distance of approximately 60 mm and the

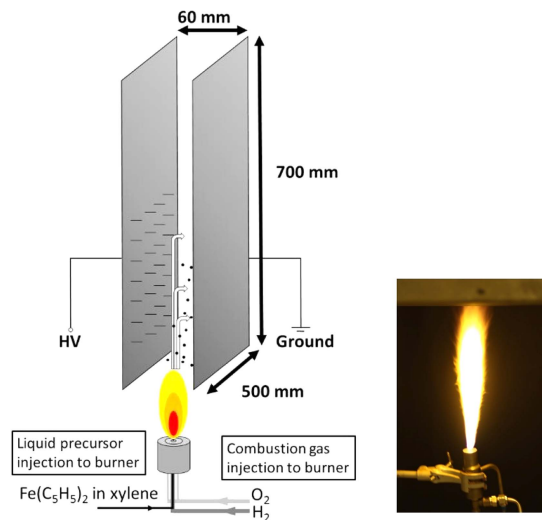


Figure 1. The LFS-process with ESP aerosol nanoparticle collector.

voltage between the plates is 20–30 kV. Distance between the burner and the plates was 380 mm. On the negative plate, there are corona needles to charge the particles. The collection plate is grounded. The LFS-process with ESP aerosol nanoparticle collector is illustrated in figure 1. The powder was finally gathered from the ESP collection plate using a special peeling tool, suitable for the nanoparticle collection. LFS-synthesized iron oxide nanoparticles are mainly in γ -Fe₂O₃ form [22].

2.3. Characterization of nanoparticles

TEM images of the nanoparticle were obtained to study the size, shape and agglomeration of the particles. The samples were prepared by mixing small fractions of nanoparticles with ethyl alcohol, pouring mixture on the TEM grid and letting the alcohol evaporate. The images were acquired using a JEOL JEM 2010 operating at accelerating voltage of 200 kV. The x-ray powder diffraction and Raman spectroscopy were used to study the composition of the iron oxides. The XRD measurements were done with Panalytical Empyrean Multipurpose Diffractometer using Cu K α radiation ($\lambda = 1.5405 \text{ \AA}$) and 45 kV and 40 mA cathode voltage and current, respectively. Raman spectra were measured with a Andor Shamrock 303 spectrometer and Andor Newton 940P cooled CCD detector. The wavelength of the excitation laser was 532 nm. Low laser power level was used to study iron oxides to avoid the heating of the sample that may cause structural phase conversions [23]. The magnetic measurements were made with a Quantum Design MPMS XL SQUID magnetometer. The virgin magnetizations as functions of the external magnetic field B and magnetic hysteresis curves at $-2.5 \text{ T} \leq B \leq 2.5 \text{ T}$ were recorded at temperatures of 10 and 300 K.

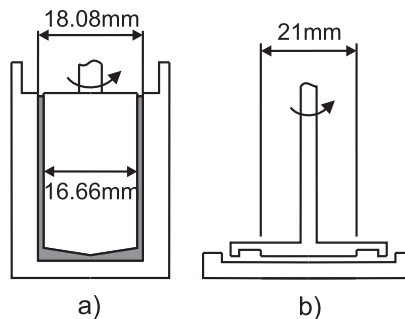


Figure 2. The concentric cylinder (a) and the plate–plate geometry (b) used to measure the off- and on-state properties, respectively.

2.4. Preparation of MR fluids

The MR fluids were prepared with a combination of sonication and mechanical mixing. Sonication was used since it has been proven to be an effective way to break down nanoparticle agglomerates, which are formed from the primary particles and aggregates by weak physical forces [24]. The aggregates generally have such strong bonds that they are not fragmented during sonication. Nanoparticles were first mixed with silicone oil and lecithin by the sonicator (Qsonica, Q700). The sonication was done in cycles where the suspension was sonicated for 10 s at 75% amplitude and then let rest for 30 s to avoid overheating. The total sonication time was 30 min. The mixing pot was cooled from outside with 3 °C liquid circulation. After sonication, the CI particles were added to the suspension and mechanical mixing was maintained at 2000 rpm for 30 min.

2.5. Characterization of MR fluids

The rheological properties of the MR fluids were studied with Anton Paar MCR301 rotational rheometer. MR fluids are desired to have a low viscosity without magnetic field (off-state) and strong increase in rheological properties with the magnetic field (on-state) causing high relative change in the properties or high MR response. Therefore, the measurements were done in both the on- and the off-state.

The CC17 concentric cylinder geometry illustrated in figure 2(a) was used for the off-state measurements since it offers a good sensitivity when measuring low-viscosity fluids. The geometry consists of a rotating inner cylinder and a stationary outer cylinder leaving 0.71 mm wide annular gap between them where the sample is confined. The viscosity curves were measured with constant shear rate tests that had two phases: the shear rate was first increased logarithmically from 0.01 to 1000 s^{-1} (up curve) and then decreased back to 0.01 s^{-1} (down curve).

The on-state rheological properties were measured with MRD180/1T magneto-cell illustrated in figure 2(b). It applies 21 mm plate–plate geometry with a stationary bottom plate and a rotating top plate. Both plates were custom made from aluminum and had roughened surfaces to avoid wall slip which can cause error to the measured values [25]. The

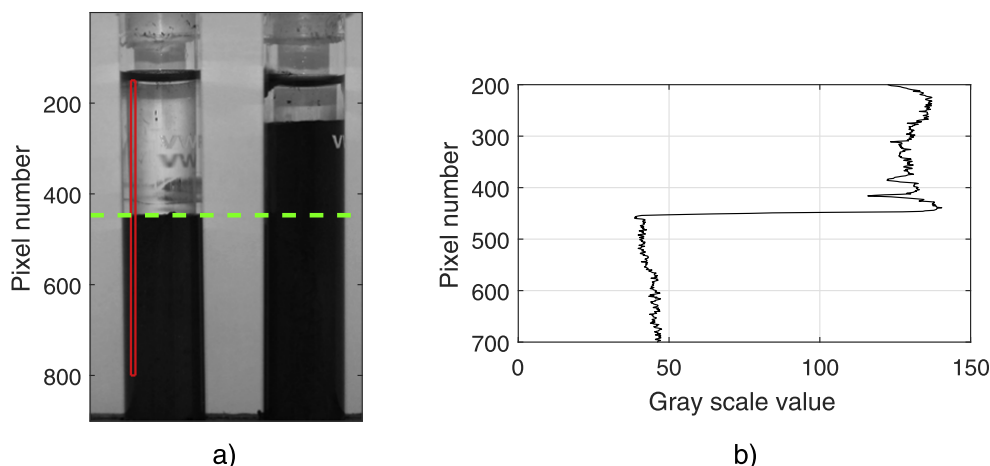


Figure 3. (a) A digital image of the test tubes where the scanned area is marked by a red box and the detected interface by a green dashed line. (b) The gradient in the grayscale values at the interface.

sample was confined in a 0.5 mm wide gap between the plates. The magneto-cell generates vertical and fairly uniform magnetic field that passes through the gap [25, 26]. The magnetic field strength was estimated by measuring the magnetic flux density from the channel underneath the bottom plate with a Hall probe. The temperature of the cell was held at 30 °C during the measurements with a circulating water bath. Two classes of on-state tests were done for the fluids: constant shear rate tests to determine the flow curves and oscillatory tests to study the viscoelastic characteristics and to evaluate the microstructure of the fluids. The flow curves were measured by increasing the shear rate logarithmically from 0.01 to 1000 1 s^{-1} . The dynamic yield stress was then evaluated from the flow curve by the Bingham model that was fitted to the data. The Bingham model is written as follows:

$$\tau_R = \tau_y + \eta_p \dot{\gamma}_R. \quad (1)$$

Here, τ_y is the yield stress and η_p the plastic viscosity.

In the oscillatory tests the samples were subjected to sinusoidal oscillatory shear strain with a strain amplitude γ_0 increasing from 0.01% to 100% at an angular frequency ω of 1 rad s^{-1} . In the linear viscoelastic regime, the resulting stress is also sinusoidal with amplitude τ_0 and phase shift δ . The in-phase and out-of-phase components of the response are the storage modulus G' and the loss modulus G'' :

$$G' = \frac{\tau_0}{\gamma_0} \cos \delta, \quad G'' = \frac{\tau_0}{\gamma_0} \sin \delta. \quad (2)$$

The moduli can be used to evaluate the microstructure of the MR fluid.

The sedimentation rate of the fluids was studied by optical tracking of the interface between the clear carrier fluid and the concentrated particle suspension that formed in the fluids over time after the mixing. The interface was tracked by using a house-built MATLAB® script to analyze digital images that were taken from the test tubes containing 5 ml of MR fluids every 60 min. The digital images were first converted to grayscale where each pixel gets a value from 0 to

255 depending on its intensity. The interface is seen numerically as a steep gradient in the grayscale values when the tube is scanned in vertical direction. The red box in the figure 3(a) shows the preselected area that was scanned by the Matlab script and the green dashed line the interface that was detected based on the gradient in the grayscale values shown in the figure 3(b). The interface position, which means the distance the interface has traveled from the top in millimeters, was then calculated based on the pixel numbers and known dimensions of the test tube.

3. Results and discussion

3.1. Properties of the nanoparticles

The characterization was done for the nanoparticles after the synthesization without sonication or surface treatment. The size distribution and shape of the nanoparticles were studied from TEM images. The TEM images are shown in figure 4. The particle geometries were mostly spherical. The arithmetic average diameters for the Nano1 and Nano2 particles were 7.9 and 16.6 nm, respectively. The averages were determined by randomly measuring 200 particles from the images. The distribution of the particle diameters is shown in figure 5. The particle size distribution is located systematically at smaller diameters for Nano1. The images show that in both cases there are also particle aggregates, which is typical for nanoparticles produced by FSP methods [15].

The composition of the particles was studied with XRD and Raman spectroscopy. The XRD patterns of the particles are shown in figure 6. The diffraction peaks are wide as expected for nanoscale particles. The peak positions can be indexed with (111), (220), (311), (400), (422), (511) and (440) planes of the inverse spinel structure of $\gamma\text{-Fe}_2\text{O}_3$. The peak positions do not fit with crystallographic structure of the hematite ($\alpha\text{-Fe}_2\text{O}_3$). The structures of the $\gamma\text{-Fe}_2\text{O}_3$ and Fe_3O_4

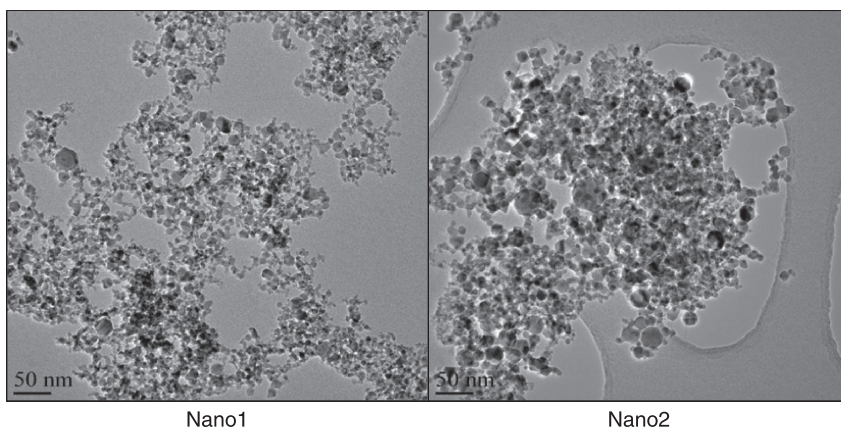


Figure 4. TEM images of Nano1 and 2 particles.

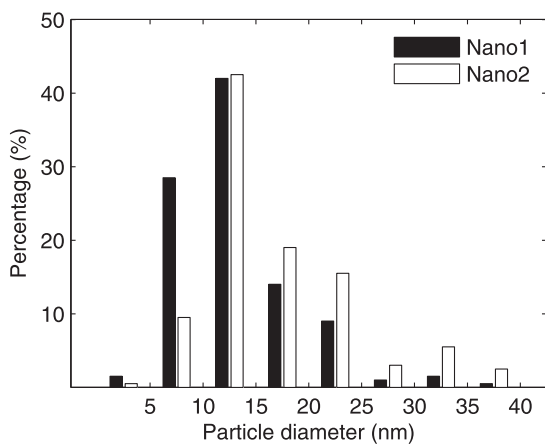


Figure 5. Distribution of the particle diameters of Nano1 and 2 particles.

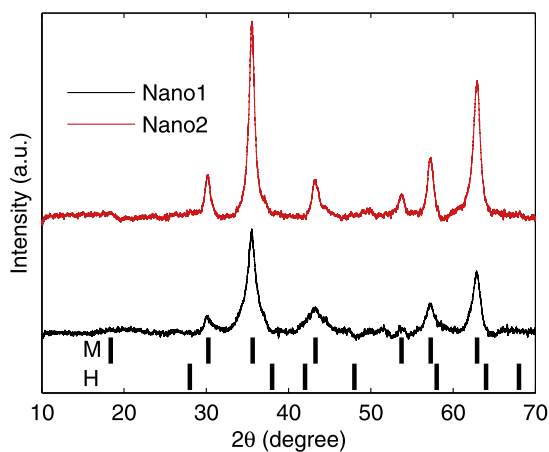


Figure 6. XRD patterns for the Nano1 and Nano2 particles. The peak positions for γ -Fe₂O₃ (M) and α -Fe₂O₃ (H) are shown below the spectrum.

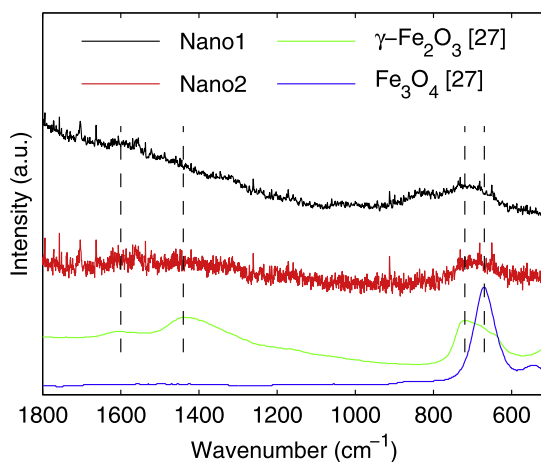


Figure 7. Raman spectrum for the Nano1 and Nano2 particles and the reference spectra for γ -Fe₂O₃ and Fe₃O₄ obtained from the research by Molchan *et al* [27].

are so similar to that they cannot be reliably distinguished based on the XRD data. Therefore, the composition of the particles was studied further by Raman spectroscopy. The Raman spectra of the Nano1 and Nano2 particles together with reference spectrum of the Fe₃O₄ and γ -Fe₂O₃ obtained from the research by Molchan *et al* [27] (reproduced by permission of The Royal Society of Chemistry) are shown in figure 7. Both samples gave low level of signal, meaning that the materials were poor Raman scatterers, and the signal-to-noise ratio was therefore low. The measured spectra have a slightly better fit on the spectrum of the γ -Fe₂O₃, especially around 700 cm⁻¹ where the strongest peaks exist. Based on the XRD patterns and Raman spectrum both nanoparticles samples are considered to be composed mainly of the γ -Fe₂O₃.

The magnetic hysteresis curves and virgin magnetizations at 10 and 300 K are shown in figures 8 and 9, respectively. At 10 K, the both Nano1 and Nano2 samples show a

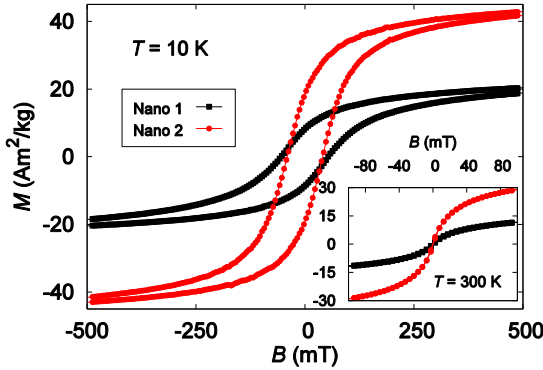


Figure 8. The magnetic hysteresis loops of Nano1 and Nano2 samples measured at 10 K (main panel) and at 300 K (inset).

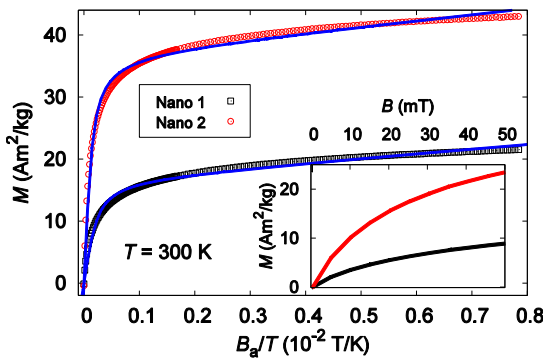


Figure 9. The magnetic virgin curves of Nano1 and Nano2 samples measured at 300 K. The blue solid curves in the main panel correspond to a fit to the Langevin function. The inset shows a closer look to the small magnetic field range up to 50 mT.

hysteretic behavior with relatively symmetric coercivity of 54 mT and 41 mT, respectively. At room temperature, the coercivity is zero, the remanent magnetization is lacking and the fit to the data of both samples is in good agreement with the Langevin function (main panel of figure 9), indicating a superparamagnetic behavior. The saturation magnetizations, M_S , at 300 K for the Nano1 and Nano2 are 22 and 43 $\text{Am}^2 \text{kg}^{-1}$, respectively, being clearly lower than for bulk $\gamma\text{-Fe}_2\text{O}_3$ of 74 $\text{Am}^2 \text{kg}^{-1}$ [14]. Similar results have been reported for iron nanoparticles earlier, e.g. Nurdin *et al* synthesized $\gamma\text{-Fe}_2\text{O}_3$ nanoparticles by chemical co-precipitation method with saturation magnetization of 32 $\text{Am}^2 \text{kg}^{-1}$ at room temperature [28].

The size and the shape of a single particle should mainly effect the coercivity and remanent magnetization which are extrinsic magnetic properties [14]. M_S is an intrinsic magnetic property, which depends mainly on the particles' composition and crystalline structure, but with nanoparticles it is also sensitive to the size. The surfaces of the nanoparticles have a thin layer where the electron spins and hence the magnetic moments are disordered, reducing the total M_S . The effect becomes stronger as the particle size decreases and the

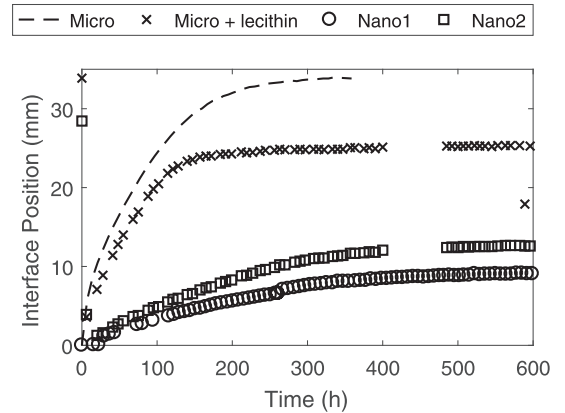


Figure 10. The sedimentation curves for the MR fluids. The curve for micro particles without lecithin is from our previous research [30].

portion of the disorder surface layer increases [29]. Since impurities was not detected in the compositional analysis of the particles it seems more plausible that the differences in magnetic properties of the Nano1 and Nano2 samples are mainly caused by the size related issues.

If the particle size distribution is assumed to be very narrow, the $M(B_a/T)$ curves of superparamagnetic particles can be well fitted using a Langevin function:

$$M(B_a/T) = M_S * [\coth(uB_a/kT) - kT/uB_a], \quad (3)$$

where M_S is the saturation magnetization at 300 K, k is Boltzmann constant, u is the average magnetic moment of the particle, T is the temperature and B_a is applied magnetic field. From the magnetization data and the fit to the Langevin function, we can now calculate an average value for particle size and compare it with the TEM results. When using the M_S values given above, the mass of the samples and the fitting parameters u/k as 102 and 159 K T^{-1} for Nano1 and Nano2, respectively, we can get the number of particles $N = M_S/u$ as 4.45×10^{16} and 5.68×10^{16} , respectively. When using the density of pure $\gamma\text{-Fe}_2\text{O}_3$ as $\rho = 4900 \text{ kg m}^{-3}$ and assuming that the samples are impurity free, we can write the volume of the single particles as 1.30×10^{-26} and $1.04 \times 10^{-26} \text{ m}^3$ for Nano1 and Nano2, respectively. These values give the estimation for the radii (in spherical particle case) as $r_{\text{Nano1}} = 1.5 \text{ nm}$ and $r_{\text{Nano2}} = 1.4 \text{ nm}$, respectively. These values are clearly smaller than the ones determined from the TEM images.

3.2. Properties of the MR fluids

The sedimentation stability of the MR fluids was studied by tracking the interface between the clear carrier fluid and suspension that formed in all fluids over time. The interface level as a function of time is shown in figure 10. The average sedimentation rate during first 100 h of the measurement for the fluid containing micron sized CI particles and lecithin was $0.042 \mu\text{m s}^{-1}$, which is slightly less than in our previous

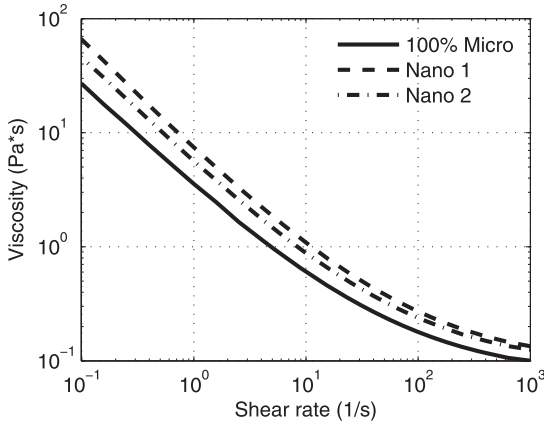


Figure 11. The off-state viscosity curves for the MR fluids.

research ($0.055 \mu\text{m s}^{-1}$) for the similar type of fluid [30]. The likely explanation for the difference is the lecithin that was here added also in the monodisperse MR fluid, but was not used in the previous research. The lecithin generates steric repulsion between the particles by molecular chains crafted on the surfaces, which increases the distance between the adjacent particles and reduce their velocity during sedimentation. López-López *et al* reported improved sedimentation stability of mineral oil based MR fluids when oleic acid was used as a surfactant for CI particles at concentrations above 1 vol% [31]. The addition of the nanoparticles reduces the sedimentation rate significantly. The sedimentation rates for MR fluids with Nano1 and Nano2 particles were 0.009 and $0.012 \mu\text{m s}^{-1}$, respectively. Results are quite well in line with previous researches. For example, Ngatu and Wereley (2007) reported a sedimentation rate of 0.0058 mm s^{-1} for their MR fluid, having total iron particle loading of 70 wt% from which 10% were magnetite nanoparticles [7]. In our previous research we reported only modest improvements in sedimentation stability when the nanoparticle concentration was 5% [30]. The reason might be that the average particle diameters in here were 7.9 and 16.6 nm, which are about three to six times smaller than in our previous research (50 nm). The decrease in particle diameter increases the total surface area which increases the overall friction between the particles and the carrier fluid. What is also evident from the figure 10, is that the interface travel at the end of the measurement is smaller for the MR fluids with nanoparticles compared to the fluid with only larger CI particles. This means that also the packing density is smaller which is in contradiction to the theory, since the nanoparticles should be able to occupy the empty spaces between larger particles, thus increasing the packing density. It is known that the nanoparticles produced by FSP methods tend to form aggregates. The existence of aggregates is the likely explanation for the reduced packing density, since the arbitrary aggregates are not able to pack as tightly as individual particles. The low packing density may make the re-dispersing of the particles easier after long storage.

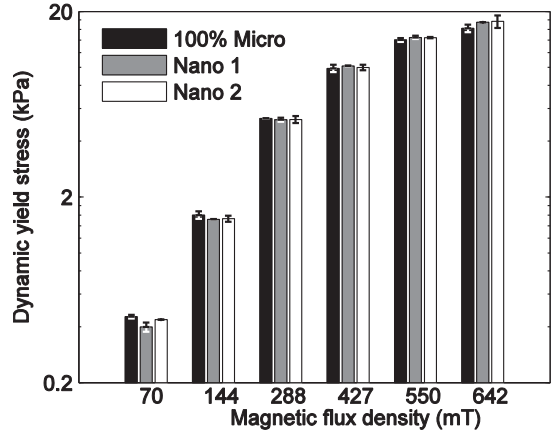


Figure 12. The averages and standard deviations of the dynamic yield stresses of MR fluids as function of magnetic flux density.

The off state viscosity curves for the MR fluids are shown in figure 11. The curves are from down phase of the measurement; the shear rate decreases from 1000 to 0.01 s^{-1} in logarithmical increments. It is obvious from the curves that all MR fluids show non-Newtonian behavior as the fluids are strongly shear thinning. This is likely due to hydrodynamic interactions between particles at moderate shear rates. It seems that the viscosities are about to reach a Newtonian plateau at 1000 s^{-1} , where the preferred flow structures of the suspensions are reached. Here the viscosities for the MR fluids containing nanoparticles are always higher than for the monodisperse MR fluid. The viscosity of the MR fluid with Nano1 particles is about 84% higher at small shear rates and the difference decreases to about 29% as the shear rate increases to 1000 s^{-1} . The corresponding values were 52% and 23% for the Nano2. Theoretically the viscosity of the bidisperse system should be smaller than that of the monodisperse system with the same particle concentration as there is a relationship between viscosity of the suspension and maximum packing density of the particles ϕ_m as described in a model by Krieger and Dougherty [32]:

$$\frac{\eta_s}{\eta_f} = \left(1 - \frac{\phi}{\phi_m}\right)^{-[\eta]\phi_m}, \quad (4)$$

where η_f is the viscosity of the carrier fluid and $[\eta]$ is the intrinsic viscosity which is equal to 2.5 for spheres. The particles in bidisperse system should reach higher maximum packing density than in the monodisperse system which would lead to smaller viscosity of the suspension. However, the sedimentation measurements revealed that the packing density in our bidisperse MR fluids were in fact smaller than in the monodisperse MR fluid at least in free settling. It can explain the unexpected viscosities as well.

The on-state dynamic yield stresses obtained from steady state measurements by a Bingham model fit are shown in figure 12. The figure shows the averages of two measurements and the standard error of the results. The measurements were done with 0.5, 1, 2, 3, 4 and 5 A coil currents that

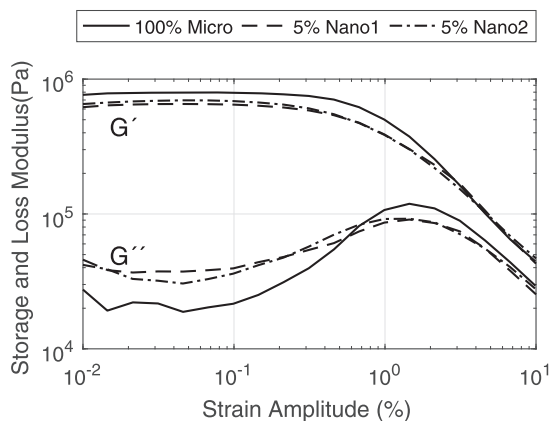


Figure 13. Amplitude sweeps for MR fluids at 427 mT flux density containing only micron sized particles and 5% and 15% of magnetite nanoparticles.

resulted to 70, 144, 288, 427, 550 and 642 mT flux densities, respectively. The dynamic yield stress represents the stress needed to continuously break the particle structures in presence of the magnetic field. The yield stresses have a strong dependence on the magnetic flux density as expected for MR fluids. The relationship follows the power-law. At moderately small flux densities ($B < 300$ mT) the relationship is about $\tau \sim B^{2.2}$ and at intermediate field strengths ($400 \text{ mT} < B < 600$ mT) the power index decreases to about 1.75 because of partial magnetic saturation of the particles. These are quite well in line with the values 2 and 1.5 given by the literature for monodisperse MR fluids [33]. The dynamic yield stresses of the bidisperse fluids are slightly lower at low flux densities and slightly higher at intermediate flux densities compared to the monodisperse fluid. The yield stress is $-12\% \dots +7\%$ with Nano1 particles and $-4\% \dots +9\%$ with Nano2. The Nano2 particles have higher saturation magnetization which can explain the slightly better values. The difference, however, is generally within the standard error of the results. The increase of the yield stress is believed to be caused by the smaller particles filling the voids between microparticles locally enhancing the magnetic field [7, 8]. Leong *et al* [34] used $\gamma\text{-Fe}_2\text{O}_3$ nanoparticles to prepare bidisperse MR fluids. They used higher total solid concentration than in our research (80.89 wt%) and the saturation magnetization of their nanoparticles was also higher ($73.8 \text{ Am}^2 \text{ kg}^{-1}$). In their research, the dynamic yield stress was higher for a bidisperse MR fluid with 5% nanoparticle concentration compared to a completely monodisperse fluid over the whole flux density range. The increase was about 8% with the highest flux density of 710 mT, which is well in line with our result of 7%–9% increase in dynamic yield stress at 642 mT.

The amplitude sweeps for the MR fluids at 427 mT flux density are shown in figure 13. The nanoparticles have similar effect at all flux densities and therefore we have chosen only the 427 mT flux density to discuss the results. The storage G' and loss moduli G'' have a linear region at low amplitudes. Here the G' is considerably higher than the G'' meaning that the deformation is mainly elastic and the

MR fluid behaves in a solid like manner. The deformation happens by stretching and tilting of the particle chain structures. Beyond the linear region the G' shows a steady decrease while the G'' first passes through a distinct maximum and then a decrease. The change in loss modulus begins at lower strain amplitudes than the storage modulus. This means that the loss modulus is more sensitive to the deformation or the structural changes of the fluid. The end of the linear region is related to the yield stress; as the stress amplitude rises above the yield stress of the MR fluid, the chain structures begin to break and the deformation changes from mainly solid to more viscous. The peaking of the G'' is called strain overshooting and it has been observed with electrorheological (ER) and MR fluids before [35, 36]. Sim *et al* explained that the overshooting is caused by the reformation process of the particle structures. Reformation comprises both destruction of the old structures and formation of new ones that dissipates energy and is seen as increase of G'' . At higher shear rates (amplitudes) the formation of the new structures is reduced and the structures break into smaller clusters or individual particles [36].

The elastic portion of the deformation decreases and viscous portion increases as part of the micron-sized particles is replaced with nanoparticles. This shows as a decrease in the storage modulus G' and an increase in the loss modulus G'' . The observations are surprising, since the dynamic yield stresses were higher for the bidisperse MR fluids at high flux densities. Wereley *et al* [8] observed similar effects as the elastic limit yield stress, determined from the storage modulus, decreased with increasing iron nanoparticle concentration even though the dynamic yield stress increased.

4. Conclusions

In this paper we have experimentally studied the properties of two $\gamma\text{-Fe}_2\text{O}_3$ nanoparticles, synthesized by LFS-method, and the properties of bidisperse MR fluids utilizing these nanoparticles. To our knowledge this is the first research where the nanoparticles in the MR fluid have been synthesized by the LFS-method. The synthesis of the nanoparticles was done with precursor feed rates of 3.0 and 8.3 ml min^{-1} , which led to average particles sizes of 7.9 and 16.6 nm, respectively. The compositions of both samples were verified to be $\gamma\text{-Fe}_2\text{O}_3$ by XRD and Raman spectroscopy. The saturation magnetization of the smaller particles was $22 \text{ Am}^2 \text{ kg}^{-1}$, which was lower than $43 \text{ Am}^2 \text{ kg}^{-1}$ measured for the larger particles and considerably lower than that of the pure $\gamma\text{-Fe}_2\text{O}_3$ ($74 \text{ Am}^2 \text{ kg}^{-1}$). The difference is likely caused by the particle sizes as no substantial amount of impurities was detected.

The substitution of 5% of micronized particles with nanoparticles in MR fluids offered significant reduction in sedimentation rate; the sedimentation rates of bidisperse fluids with 7.9 nm and 16.6 nm nanoparticles were 0.009 and $0.012 \mu\text{m s}^{-1}$ respectively which is a significant improvement to the $0.042 \mu\text{m s}^{-1}$ of monodisperse fluid. However, the off-state viscosity of these bidisperse fluids increased 52%–84% at low shear rates and 23%–29% at high shear rates compared to

the monodisperse fluid. The higher viscosity at low shear rates is probably contributing to the improved sedimentation rate. The dynamic yield stress of the bidisperse MR fluids decreased at the lowest flux densities and increased at the highest flux densities compared to the monodisperse MR fluid. The MR fluid with larger nanoparticles had slightly higher yield stresses, which can be explained by the higher saturation magnetization of particles. The oscillatory testing revealed that the nanoparticles made the response of the MR fluid more viscous.

It was shown, that γ -Fe₂O₃ nanoparticles synthesized by LFS-method can be used to prepare a bidisperse MR fluids with improved sedimentation stability while still maintaining good MR properties. The drawback was increased off-field viscosity which was likely caused by nanoparticle aggregates characteristic for the particles synthesized with flame spray processes.

Acknowledgments

The Jenny and Antti Wihuri Foundation is acknowledged for the financial support.

References

- [1] Bossis G, Volkova O, Lacis S and Meunier A 2002 Magnetorheology: fluids, structures and rheology *Ferrofluids: Magnetically Controllable Fluids and Their Applications* ed S Odenbach (Berlin, Heidelberg: Springer Berlin Heidelberg) pp 202–30
- [2] Carlson J D and Jolly M R 2000 MR fluid, foam and elastomer devices *Mechatronics* **10** 555–69
- [3] de Vicente J, Klingenberg D J and Hidalgo-Alvarez R 2011 Magnetorheological fluids: a review *Soft Matter*. **7** 3701–10
- [4] Ashtiani M, Hashemabadi S H and Ghaffari A 2015 A review on the magnetorheological fluid preparation and stabilization *J. Magn. Magn. Mater.* **374** 716–30
- [5] Chaudhuri A, Wang G and Wereley N M 2005 Substitution of micron by nanometer scale powders in magnetorheological fluids *Int. J. Mod. Phys. B* **19** 1474–80
- [6] Chin B D, Park J H, Kwon M H and Park O O 2001 Rheological properties and dispersion stability of magnetorheological (MR) suspensions *Rheol. Acta* **40** 211–9
- [7] Ngatu G T and Wereley N M 2007 Viscometric and sedimentation characterization of bidisperse magnetorheological fluids *Trans. Magn.* **43** 2474–6
- [8] Wereley N M, Chaudhuri A, Yoo J H, John S, Kotha S, Suggs A, Radhakrishnan R, Love B J and Sudarshan T S 2006 Bidisperse magnetorheological fluids using Fe particles at nanometer and micron scale *J. Intell. Mater. Syst. Struct.* **17** 393–401
- [9] Rosenfeld N, Wereley N M, Radhakrishnan R and Sudarshan T S 2002 Behavior of magnetorheological fluids utilizing nanopowder iron *Int. J. Mod. Phys. B* **16** 2392–8
- [10] Lopez-Lopez M T, Kuzhir P, Lacis S, Bossis G, Gonzalez-Caballero F and Duran J D G 2006 Magnetorheology for suspensions of solid particles dispersed in ferrofluids *J. Phys.: Condens. Matter* **18** 2803–13
- [11] Shimada K, Akagami Y, Fujita T, Miyazaki T, Kamiyama S and Shibayama A 2002 Characteristics of magnetic compound fluid (MCF) in a rotating rheometer *J. Magn. Magn. Mater.* **252** 235–7
- [12] Patel R 2011 Mechanism of chain formation in nanofluid based MR fluids *J. Magn. Magn. Mater.* **323** 1360–3
- [13] Viota J L, Duran J D G, Gonzalez-Caballero F and Delgado A V 2007 Magnetic properties of extremely bimodal magnetite suspensions *J. Magn. Magn. Mater.* **314** 80–6
- [14] Serna C J and Morales M P 2004 Maghemite (γ -Fe₂O₃): a versatile magnetic colloidal material *Surface and Colloid Science* ed E Matijevic and M Borkovec (Boston, MA: Springer US) pp 27–81
- [15] Ulrich D G 1971 Theory of particle formation and growth in oxide synthesis flames *Combust. Sci. Technol.* **4** 47–57
- [16] Kammiller H K, Mädler L and Pratsinis S E 2001 Flame synthesis of nanoparticles *Chem. Eng. Tech.* **24** 583–96
- [17] Teleki A, Wengeler R, Wengeler L, Nirschl C H and Pratsinis S E 2008 Distinguishing between aggregates and agglomerates of flame-made TiO₂ by high-pressure dispersion *Powder Technol.* **181** 292–300
- [18] Mäkelä J M, Keskinen H, Forsblom T and Keskinen J 2004 Generation of metal and metal oxide nanoparticles by liquid flame spray process *J. Mater. Sci.* **39** 2783–8
- [19] Haapanen J, Aromaa M, Teisala H, Tuominen M, Stepien M, Saarinen J J, Heikkilä M, Toivakka M, Kuusipalo J and Mäkelä J M 2015 Binary TiO₂/SiO₂ nanoparticle coating for controlling the wetting properties of paperboard *Mater. Chem. Phys.* **149–150** 230–7
- [20] Mäkelä J M, Hellsten S, Silvonen J, Vippola M, Levänen E and Mäntylä T 2006 Collection of liquid flame spray generated TiO₂ nanoparticles on stainless steel surface *Mater. Lett.* **60** 530–4
- [21] Carlson D J 2008 Magnetorheological fluids *Smart Materials* ed M Schwartz (Boca Raton, FL: CRC Press) ch 17
- [22] Harra J, Nikkanen J-P, Aromaa M, Suhonen H, Honkanen M, Salminen T, Heinonen S, Levänen E and Mäkelä J M 2013 Gas phase synthesis of encapsulated iron oxide–titanium dioxide composite nanoparticles by spray pyrolysis *Powder Technol.* **243** 46–52
- [23] Li Y-S, Church J S and Woodhead A L 2012 Infrared and Raman spectroscopic studies on iron oxide magnetic nanoparticles and their surface modifications *J. Magn. Magn. Mater.* **324** 1543–50
- [24] Mandzy N, Grulke E and Druffel T 2005 Breakage of TiO₂ agglomerates in electrostatically stabilized aqueous dispersions *Powder Technol.* **160** 121–6
- [25] Jönkkäri I, Kostamo E, Kostamo J, Syrjälä S and Pietola M 2012 Effect of the plate surface characteristics and gap height on yield stress of a magnetorheological fluid *Smart Mater. Struct.* **21** 75030–40
- [26] Laun H M, Schmidt G, Gabriel C and Kielburg C 2008 Reliable plate–plate MRF magnetorheometry based on validated radial magnetic flux density profile simulations *Rheol. Acta* **47** 1049–59
- [27] Molchan I S, Thompson G E, Lindsay R, Skeldon P, Likodimos V, Romanos G E, Falaras P, Adamova G, Iliev B and Schubert T J S 2014 Corrosion behaviour of mild steel in 1-alkyl-3-methylimidazolium tricyanomethanide ionic liquids for CO₂ capture application *RSC Adv.* **4** 5300–11
- [28] Nurdin I, Johan M R, Yaacob I I, Ang B C and Andriyana A 2014 Synthesis, characterization and stability of superparamagnetic maghemite nanoparticle suspension *Mater. Res. Innov.* **18** 200–3
- [29] Jun Y W, Seo J W and Cheon J 2008 Nanoscaling laws of magnetic nanoparticles and their applicabilities in biomedical sciences *Acc. Chem. Res.* **41** 179–89
- [30] Jönkkäri I, Matti I and Syrjälä S 2015 Sedimentation stability and rheological properties of ionic liquid-based bidisperse magnetorheological fluids *J. Intell. Mater. Syst. Struct.* **26** 2256–65

- [31] López-López M T, De Vicente J, González-Caballero F and Durán J D G 2005 Stability of magnetizable colloidal suspensions by addition of oleic acid and silica nanoparticles *Colloids Surf. A* **264** 75–81
- [32] Krieger I M and Dougherty T J 1959 A mechanism for non-Newtonian flow in suspensions of rigid spheres *Trans. Soc. Rheol.* **3** 137–52
- [33] Bossis G, Laci S, Meunier A and Volova O 2002 Magnetorheological fluids *J. Magn. Magn. Mater.* **252** 224–8
- [34] Leong S A N, Mazlan S A, Samin P M and Idris A 2016 Ubaidillah, performance of bidisperse magnetorheological fluids utilizing superparamagnetic maghemite nanoparticles *AIP Conf. Proc.* **1710** 030050
- [35] Li W H, Du, H and Guo N Q 2004 Dynamic behavior of MR suspensions at moderate flux densities *Mater. Sci. Eng. A* **371** 9–15
- [36] Sim H G, Ahn K H and Lee S J 2003 Three dimensional dynamics simulation of electrorheological fluids under large amplitude oscillatory shear flow *J. Rheol.* **47** 879–95

Tampereen teknillinen yliopisto
PL 527
33101 Tampere

Tampere University of Technology
P.O.B. 527
FI-33101 Tampere, Finland

ISBN 978-952-15-4184-1

ISSN 1459-2045